A Converter-Enhanced Synchronous Compensator for LCC-HVDC Links Feeding Weak AC Systems

by

Narges Zarean Shahraki

A thesis submitted to the Faculty of Graduate and Postdoctoral Studies of
The University of Manitoba
in partial fulfilment of the requirements of the degree of

Doctor of Philosophy

Department of Electrical and Computer Engineering
University of Manitoba
Winnipeg, Canada

Copyright © 2̃025 Narges Zarean Shahraki

Abstract

High Voltage Direct Current (HVDC) technology is increasingly being utilized for long-distance power transmission and the integration of large-scale renewable energy sources. While Voltage Sourced Converters (VSC-HVDC) are gaining prominence for their compatibility with weak ac systems, Line-Commutated Converters (LCC-HVDC) remain the standard for bulk, high-power applications due to their robustness and superior dc fault control. However, LCC technology requires a strong synchronous voltage source for commutation, typically demanding a short-circuit ratio (SCR) greater than 2.0. Furthermore, LCC-HVDC consumes significant reactive power, up to 50–60% of its real power rating at full load, which must be supplied by ac filters, shunt capacitors, or a high-capacity ac network.

Traditional synchronous condensers (SCs) provide both reactive power and inherent inertia. However, they are characterized by high maintenance requirements and relatively sluggish response time. Conversely, power electronic-based STATCOMs offer rapid, flexible reactive compensation and superior voltage support during disturbances. However, a standard STATCOM lacks the ability to provide an inertial response unless integrated with a battery energy storage system (BESS).

This thesis proposes a novel topology integrating a synchronous condenser (SC) into the ac bus of a weak LCC-HVDC system via a back-to-back (BtB) voltage source converter

link. This configuration provides significantly enhanced steady-state reactive power support and superior short-circuit current contribution during voltage disturbances compared to standalone units. Furthermore, during frequency events, the BtB-SC interface enables active power exchange proportional to the system's inertia, delivering support that far exceeds the physical limits of a traditional SC with equivalent MVA and H ratings.

By implementing an advanced control system for the BtB-SC, this configuration significantly improves transient rotor angle stability margins during severe events, such as sustained three-phase faults. Upon disturbance detection, the synchronous link between the SC and the grid is decoupled, enabling asynchronous operation. This intentional decoupling facilitates larger SC speed deviations, allowing for more kinetic energy exchange between the SC rotor and the ac network. Consequently, the system enhances resilience against rotor angle instability.

Using electromagnetic transient (EMT) simulations, this research demonstrates that the proposed BtB-SC topology significantly outperforms standalone synchronous condensers. Under voltage disturbances, the BtB-SC provides superior reactive power support compared to a standalone SC, accelerating voltage recovery. During frequency transients, its asynchronous configuration results in enhanced apparent inertia, attenuated frequency deviations, and a reduced $RoCoF$. Scaling the back-to-back VSC rating further enhances these benefits by expanding the power exchange capacity within IGBT thermal limits. Finally, a Genetic Algorithm was employed to optimize active power control parameters, achieving the highest frequency nadir and minimum $RoCoF$ during loss of the system's largest generator.

The thesis also introduces a novel online inertia measurement method is introduced for Inverter-Based Resources utilizing the bus frequency signal. It is applied to both Grid-Forming and Grid-Following systems. With this tool the actual inertia contribution offered

by the proposed BtB-SC scheme can be measured. A primary advantage of the proposed approach is its efficacy in black-box modeling scenarios; it requires no knowledge of internal controller parameters, making it ideal for industry applications where proprietary data is restricted. Its performance is validated through EMT-based numerical case studies, which demonstrate the robustness and precision of the proposed measurement technique.

Copyright Forms

I would like to acknowledge the use of the following papers in the preparation of this thesis in compliance with the appropriate publisher's copyright statements.

1. "Enhancing inertia and voltage regulation using converter-interfaced synchronous condensers at LCC-HVDC terminals," *in IET Conference Proceedings CP918*, IET, 2025, pp. 357–362.

   https://ieeexplore.ieee.org/abstract/document/11004532

2. "Transient stability enhancement using converter-interfaced synchronous condenser at LCC-HVDC terminals," *CIGRE 2025 International Symposium Palais des Congrès de Montréal, Québec*, Canada, 2025.

   https://www.e-cigre.org/publications/detail/symp-mon-2025-symposium-montreal.html

3. "Online inertia estimation of inverter-based resources using bus frequency measurement," Electric Power Systems Research 252, 112306, 2026.

   https://www.sciencedirect.com/science/article/abs/pii/S0378779625008934

4. "Optimized virtual inertia control for frequency regulation at LCC-HVDC terminals using converter-interfaced synchronous condenser," Electric Power Systems Research 262, 113616, 2027.

https://www.sciencedirect.com/science/article/pii/S0378779626009090

Acknowledgements

I wish to express my deepest gratitude to all the individuals whose contributions, guidance, and encouragement made the completion of this doctoral thesis possible. Their mentorship and support have been indispensable at every stage of this research. First and foremost,

I extend my deepest gratitude to my supervisor, Dr. Aniruddha Gole. Your unwavering commitment to excellence, inspiring mentorship, and remarkable patience have been instrumental in shaping my development as a researcher. Our insightful discussions(and the memorable coffee breaks) continually encouraged me to strive for the highest standards and were invaluable in refining this thesis.

I would like to extend my sincere gratitude to my Mitacs industry advisor, Dr. Mojtaba Mohaddes at TransGrid Solutions Corporation, who has been a constant source of inspiration, support, and camaraderie. His exceptional technical expertise, generous mentorship, and collaborative spirit, alongside many stimulating discussions, have greatly enriched my research experience. Furthermore, the collaborative environment at TransGrid Solutions has been instrumental in shaping my ideas and broadening my professional perspective.

I also express my sincere gratitude to my advisory and examining committee members, Dr. Shaahin Filizadeh, Dr. Jenny Zhou, and the external examiner Dr. Ramakrishna Gokaraju,

for their time, critical insights, and generous guidance. Their perceptive suggestions significantly elevated the quality and rigor of this dissertation.

I am deeply grateful to my colleagues in the power systems simulation lab, especially Dr. Kaustav Dey and Dr. Ajinkya Sinkar, whose research excellence, dedication, and encouragement have continually inspired me throughout this work.

Finally, my deepest appreciation belongs to my family. To my loving and supportive husband, my parents, and my sisters—thank you for your unconditional love, patience, and guidance, which inspire and anchor me in everything I pursue.

Table of Contents

Abstract ii

Copyright Forms v

Acknowledgements vii

List of Figures xiii

List of Tables xviii

1 Introduction **1**

1.1 Background 1

1.2 New proposed Reactive Power Compensator 10

1.3 Research Objectives and Contributions 10

1.3.1 Research Objectives 10

1.3.2 Summary of Contributions 11

1.4 List of Publications 12

1.5 Thesis Organization 13

2 High Voltage Direct Current Transmission Schemes **15**

2.1 AC Systems 15

2.2 LCC-HVDC Transmission Schemes 17

2.2.1 Operation Principles of Line Commutated Converter 19
2.2.2 AC Filters 21
2.2.3 LCC Control Systems 23
2.2.4 Phase Locked Loop (PLL) 24
2.3 VSC-HVDC Transmission Schemes 25
2.3.1 Two-level Voltage Source Converter (VSC) 25
2.3.2 Modular Multilevel Converter (MMC) 27
2.3.3 VSC Converter-level Control 29
2.4 Summary 35

3 Enhancing Transient Stability in Weak LCC-HVDC Systems Using the Converter-interfaced Synchronous Condenser 36

3.1 Synchronous Condenser 39
3.1.1 short-circuit Strength Contribution 40
3.1.2 Inertia Contribution 41
3.2 STATCOM 43
3.3 Back-to-back Converter-Interfaced Synchronous Condenser 46
3.3.1 Operating Principle of the Back-to-Back Synchronous Condenser (BtB-SC) 46
3.4 BtB-SC Configuration for Improving Transient Stability 48
3.5 Impact of BtB-SC on Frequency Stability of LCC-HVDC 52
3.6 A Comment on Economic Considerations of the Proposed Scheme 68
3.7 Summary 68

4 Enhancing Inertia and Voltage Regulation Using the BtB-SC at LCC-HVDC Terminals 70

4.1 Performance Comparison of BtB-SC and Standalone SC 71

4.1.1 Voltage Regulation Due to an ac Fault 71

4.1.2 Comparison of a Stand-alone SC and BtB-SC due to a Frequency Event 73

4.2 Optimizing BtB-SC Virtual Inertia for Frequency Regulation 85

4.2.1 Background of Genetic Algorithm 86

4.3 Summary 92

5 Online Inertia Estimation of Inverter-Based Resources 93

5.1 Probing Signal Based Inertia Measurement [29] 95

5.2 Inertia Estimation directly from Bus Frequency Measurements 100

5.2.1 Bus Frequency-based Inertia Measurement of Classical Generator Model105

5.3 Inertia Measurement of Grid-Forming Inverters with VSG Control 112

5.3.1 Inertia measurement using ω_{vsg} signal 114

5.3.2 Bus Frequency-based Inertia Measurement 116

5.3.3 Effect of Variation in Operating Conditions on Inertia Measurement . 118

5.4 Inertia Measurement of a Grid-Following BtB-SC 119

5.4.1 Measurement of BtB-SC Apparent Inertia Using Internal Speed Signal 119

5.4.2 Measurement of BtB-SC Apparent Inertia Using Bus Frequency Signal 121

5.5 Summary 123

6 Contributions, Conclusion, and Recommendations for Future Work 124

6.1 Contributions and Conclusions 124

6.2 Future Work 126

References 128

Appendix A PLL small signal modeling 136

List of Figures

2.1 Rectifier-side ac system 16
2.2 A 12-pulse LCC-HVDC transmission system 18
2.3 Graetz bridge: a three-phase 6-pulse full-wave bridge converter 19
2.4 Line commutated converter waveforms. (a) three-phase line voltages and the dc voltage; (b) phase-a line current 21
2.5 Two Graetz bridges connected in series on the dc side and parallel on the ac side. There is one tap-changing transformer with a $Y - Y$ configuration and one with a $\Delta - Y$ configuration 22
2.6 Control system of LCC-HVDC system 23
2.7 Block diagram of PLL 25
2.8 A three-phase, 2-level, 6-pulse bridge configuration of a VSC with IGBTs coupled with anti-parallel diodes 26
2.9 Two-level VSC output voltage 27
2.10 (a) Half-bridge or Full-bridge Schematic Diagram of a One-phase MMC. (b) Schematic Diagram of MMC Output Voltage Waveforms. 28
2.11 Grid-following control diagram of VSC-HVDC including inner and outer controllers 30

2.12 Droop Control Structure 32
2.13 VSG control structure 34

3.1 Typical Synchronous Condenser Configuration 40
3.2 Simplified Synchronous Condenser short-circuit Diagram 41
3.3 Typical STATCOM Configuration 44
3.4 BtB-SC Schematic 47
3.5 Steady-state equivalent circuit 48
3.6 BtB-SC active power control block diagram 50
3.7 Selection of K_2: (a) ac frequency, (b) P_i: constant K_2 mode and (c) P_i: dynamic K_2 mode 51
3.8 LCC-HVDC System configuration 53
3.9 Voltage recovery for circuit breaker opening times of 100, 150, 200 and 250 ms 57
3.10 Frequency recovery for circuit breaker opening times of 100, 150, 200, and 250 ms 58
3.11 Impact of BtB-SC with $K_2 = 70$, constant control mode, fault duration of 100 ms and 200 ms 60
3.12 Direct-axis current (a) synchronous condenser active power (b) and speed (c) in constant control with $K_2 = 70$, during 100 ms & 200 ms faults 61
3.13 Post-fault voltage recovery with and without BtB-SC: (a) voltage restoration (b) reactive power, and (c) q-axis current with $K_2 = 70$, during 100 ms faults 62
3.14 Post-fault voltage regulation with and without BtB-SC: (a) voltage restoration and (b) Grid-side converter q-axis current with $K_2 = 70$, during 100 ms, and 200 ms faults 63

3.15 VSC's ac and dc voltages during BtB-SC operation, with (a) ac voltages and (b) dc voltages 64
3.16 System Frequency (a) Direct-axis current of Machine-side (MS) converter (b) SC active power (c) and SC speed (d) under dynamic selection mode with $K_2 = 70$, during 100 ms & 200 ms faults 65
3.17 Comparison of BtB-SC with dynamic and constant K_2 control for fault duration of 200 ms 66
3.18 Comparison of BtB-SC with $K_1 = 0$ & $K_1 = 20$ in dynamic control mode for fault duration of 200 ms 67

4.1 Comparison of voltage dynamic response between the standalone SC and the BtB-SC 72
4.2 Comparison of reactive power contribution between the standalone SC and the BtB-SC 73
4.3 Frequency regulation for LCC-HVDC system using stand-alone SC and BtB-SC with $K_1 = 0$ during a frequency event 77
4.4 Synchronous Condenser speed recovery 78
4.5 Frequency regulation comparison for LCC-HVDC system using high-rating and high-inertia stand-alone SC and BtB-SC 80
4.6 Voltage regulation comparison for LCC-HVDC system using high-rating and high-inertia stand-alone SC and BtB-SC 80
4.7 Direct-axis current profile for 70 MVA (a) and 85 MVA (b) converter ratings, active power (c) 82
4.8 Post-contingency frequency recovery profiles for 70 MVA and 85 MVA converter ratings 82

4.9 System performance comparison: standalone SC vs. BtB-SC with $K_2 = 0$ during a frequency event 83
4.10 Frequency regulation for LCC-HVDC system using BtB-SC with $K_1 = 4$ and $K_2 = 60$ during a frequency event 85
4.11 Post-contingency crossrecovery profiles for different K_1 and K_2 settings; area A denotes recovery speed 87
4.12 Flowchart of the Genetic Algorithm 88
4.13 Comparison of post-contingency frequency recovery for K_1=4, K_2=60, and the optimal results achieved by the genetic algorithm at K_1=10.6008, K_2=102.062 91
4.14 Post-contingency frequency recovery performance, achieved using the control parameters optimized via a Genetic Algorithm ($K_1 = 10.6008$, $K_2 = 102.062$) 91

5.1 Probing frequency injection (a) Voltage injection (b) Current injection 97
5.2 Schematic for inertia measurement of synchronous generator 98
5.3 Schematic diagram of three-phase PLL 101
5.4 Frequency response of three-phase PLL parameters 103
5.5 Steady-state behaviour of PLL frequency measurement 104
5.6 Schematic of classical generator connected to infinite bus 106
5.7 Frequency response of $A(s)$ for different values of x'_d 108
5.8 Comparison of terminal voltage frequency and rotor speed waveforms for classical synchronous machine model with injected probing frequency $\Delta f = 0.3$ Hz for $x'_d = 0.1$ pu, $x'_d = 0.8$ pu 109
5.9 Schematic of internal voltage measurement approach 110

5.10 Comparison of terminal voltage frequency and rotor speed waveforms for classical synchronous machine model with injected probing frequency $\Delta f = 0.3$ Hz for $x'_d = 0.8$ pu without and with the compensation 111

5.11 Power circuit schematic of VSC-based inverter 113

5.12 Observation that inertia estimation is not affected by active power change . . 118

5.13 Schematic for apparent inertia measurement of BtB-SC using internal speed signal 120

5.14 Power circuit schematic of BtB-SC for apparent inertia measurement of BtB-SC using bus frequency signal 122

A.1 PLL block diagram 136

List of Tables

3.1 SC and STATCOM Comparison [71] 45
3.2 Selection criteria of K_2 value 52
3.3 LCC-HVDC System Parameters 54
3.4 Synchronous machines and SC parameters 55

4.1 Genetic Algorithm Configuration Parameters 90

5.1 Inertia measurement for classical generator model 99
5.2 Measured Inertia values for classical generator model for different power loadings (P_o) and injected probing signal frequencies 112
5.3 VSG converter system parameters 115
5.4 Inertia measurement of VSG converter with ω_{vsg} signal 115
5.5 Inertia measurement of VSG converter with bus frequency (without internal impedance compensation) 116
5.6 Inertia measurement of VSG converter with bus frequency (with internal impedance compensation) 117
5.7 Inertia measurement of BtB-SC compensator using synchronous generator speed 121
5.8 Inertia measurement of BtB-SC compensator using bus frequency 122

Chapter 1

Introduction

This chapter introduces the research background of the thesis. It outlines the details of High Voltage Direct Current (HVDC) converter equipment, such as Line-Commutated Converter (LCC) and Voltage-Sourced Converter (VSC). LCCs are commonly used in HVDC Transmission for bulk transmission of large units of power. Although competing technologies such as VSCs are being introduced, they still lack the high ratings available through LCCs. One of the challenges with LCCs is that they require an ac source at the converter busbar to provide reactive power and voltage support. This thesis investigates a novel approach to address this limitation that not only provides reactive power support but also provides synthetic inertia to enhance the performance of LCC-HVDC systems. This chapter outlines the objectives and structure of the thesis.

1.1 Background

HVDC is a popular technology used for bulk power transmission. Its reduced power losses, reduced transmission line costs, increased system stability, better power flow control, and fast

semiconductor technology development make it more competitive with ac transmission [1]. HVDC transmission can work not only with overhead transmission lines, but also with underwater or underground cables, while large capacitance makes ac transmission challenging. It is also used to interconnect asynchronous power systems where conventional alternating current (ac) connections cannot be used. These systems are widely used today.

HVDC technology is categorized by the power electronic switching devices used in the ac to dc converter. Line-commutated, current source converter (LCC-CSC) technology has been commercially available since the mid-1950s. Today, voltage-sourced converter-based HVDC (VSC-HVDC) is also seeing increased use as it can operate in very weak ac systems and is very suitable for use in HVDC networks. Nevertheless, LCC-HVDC converters continue to be widely used, particularly for being relatively less expensive and commercially available with significantly higher ratings. These converters have the advantage of being robust and can rapidly control the direct current, e.g., at faults on the dc side. However, thyristor-based converters require a synchronous voltage source to commutate due to the limited flexibility within the thyristor valve [2], with which the converter stations must consume a large amount of reactive power. Under full load conditions, the reactive power consumption can be as high as 50–60% of the active power [3]. This demand is supplied by the ac filters, shunt capacitor banks, or the ac network, provided it has sufficient short-circuit capacity. The network short-circuit level at the converter bus should typically be more than double the converter's MVA rating to operate.

In modern power systems, new challenges arise as the penetration of renewable energy sources (RES) increases. Unlike traditional synchronous-generator-based power systems that provide short-circuit capacity, inertia, and self-synchronization, power-electronics converter-based renewable energy sources do not do so, and make the systems appear weaker. The

arising potential network operation problems are as follows:

- Voltage Stability

  Synchronous generators are fitted with automatic voltage regulators (AVRs) and excitation systems that help maintain the reactive power balance across the power system and regulate network voltages. As power Inverter-Based Resource (IBR) levels increase, the reactive power balance will likely be affected. It is necessary to provide sufficient reactive power for rapid voltage recovery when large disturbances occur. Conventional synchronous generators can supply 5-7 times the rated current during network fault events, but IBRs have very limited overload capability. The geographical area affected by low voltages is therefore increased due to the decrease in conventional synchronous generators.

- Decreased System Strength

  Power system strength is an inherent characteristic of any power system, which is usually measured in terms of fault current (or fault level in MVA). It describes the network's ability to withstand variations in active and reactive power flows and its resilience to network disturbances. Using this measure can help quantify the robustness of a system following a disturbance. HVDC systems typically use the short-circuit ratio as a measure of system strength, which is the ratio of the MVA fault level to the rated HVDC power transmitted.

  As a rule, higher relative fault levels are associated with stronger power systems, which are typically meshed networks with multiple transmission lines and generation sources contributing to fault currents. In such networks, voltages generally are more stable following disturbances (small or large). During disturbances, conventional synchronous

generation can provide much higher fault currents (reactive power injections), which contribute significantly to the strength of the system [4].

For LCC-HVDC systems, the risk of commutation failure increases significantly if voltage depressions in any phase are greater than 20% at the connection point [5]. On the other hand, if the voltage depressions within any phase are less than 10%, there is a very low probability of commutation failure. Due to voltage depressions caused by weak systems, LCCs are more susceptible to commutation failures when connected to weak IBR systems. In the event of commutation failures, there can be large oscillations in the active power in the remaining portion of the network. The so-called 'commutation failure zones of vulnerability' have been defined in Canada [6]. Substations in these zones can suffer at least 10% sudden voltage drops. Any inverter-based developments in these zones are assessed thoroughly to confirm there are no risks to the power system.

- Frequency Stability

  RES are generally coupled to the grid through power electronics, so the 'natural' inertial response is not inherently present. The replacement of conventional synchronous generation with RES has led to a faster frequency dynamic with a larger Rate of Change of Frequency (RoCoF) and frequency deviation following a contingency due to the deterioration of the system's inertial response [4].

  Long-term and short-term frequency stability issues [7] caused by converter-based systems. Low-inertia systems with a limit of short-circuit power from converter-interfaced generation may cause poor dynamic performance compared to conventional grids. Power oscillations resulting from low inertia operating conditions and weak intercon-

nections among power systems are more significant. The oscillatory characteristic in low-inertia systems is completely different from that of conventional systems due to the different physical characteristics and interaction with the grid of converter-based components. This causes power oscillations in a low-inertia system during a slight load increase when the system is operating based on converter-based generation [8, 9].

Some of these weak ac grid operation challenges can be alleviated using dynamic reactive power supply apparatuses that adapt their capacity to network conditions to keep the ac voltage within the desired tolerance. Reactive power regulation can be achieved by controlling the reactive power consumption of HVDC converters, which usually increases the converter rating. It can also be performed by switching reactive shunt elements, i.e., ac filters, shunt capacitors, and shunt reactors, while maintaining filtering requirements. Shunt capacitors are generally divided into several banks that can be switched on and off according to the demand for reactive power. As the number of banks in operation changes, the ac busbar voltage of the converter station varies in a stepwise manner. The MVAr size of capacitor banks to be switched must be limited to keep variation within the maximum acceptable limits. Other dynamic reactive power compensation systems, which utilized globally, specifically for LCC-HVDC systems, are synchronous condensers or static synchronous compensators (STATCOM) [10–16].

A Synchronous Condenser (SC) is an actual synchronous machine operating without a prime mover, hence supplying only reactive power in the steady-state. It has been playing a crucial role in reactive power compensation and maintaining voltage stability in power systems for decades [17]. By varying the field excitation current, SC can operate in over-excited or under-excited modes to supply/absorb reactive power to/from the networ, which can smoothly control the voltage or keep the system power factor at a specified level. Ad-

ditionally, SC can support short-circuit current into the network, which makes the network appear to be stronger [18]. However, synchronous condensers require high maintenance and can have a slow response due to the rotor inertia. Hence, many LCC-HVDC-based utilities are contemplating replacing them with other power electronic reactive power compensators, such as a static compensator (STATCOM).

FACTS devices such as static compensators (STATCOM), and static Var compensators (SVC) have played an increasingly important role in addressing the changing needs of the power system. STATCOM has become the most popular FACTS device in recent years. It is often preferred over thyristor-based SVCs due to minimal no-load losses, a smaller footprint, and better under-voltage performance [19, 20]. The state-of-the-art multilevel configuration STATCOM produces much fewer harmonics; as a result, they no longer need a harmonic filter to achieve the required harmonic grid code requirements [21,22]. The static compensator acts as a fast adjustable current source that provides flexible reactive compensation. Its response is fast both for set-point changes and dynamic voltage support in case of a power network disturbance. STATCOMs can also offer very fast absorption/injection of reactive power during (fault period) and after the disturbance (fault recovery period), and high absorption of reactive power in case of over-voltage scenarios. These devices may also feature active filtering, flicker compensation, and power oscillation damping (POD) [23].

The adoption rate of STATCOM has been increasing globally, while SCs have experienced a revival. One of the main reasons behind the recent growth in interest in synchronous condenser applications is the inertia of the synchronous machine rotor. Due to the transition from traditional synchronous machine-based power generation to renewable-based systems, such needs arise. In renewable-based systems, many wind and PV generation units are interfaced to the grid using power electronics that typically have no rotational inertia [24].

Only synchronous condensers provide an inertia contribution among all power stabilization products or systems (e.g., SVC, STATCOM, capacitor banks, etc). Other new technologies based on virtual inertia ideas focus on solving the same problem, e.g., using wind turbine speed reduction. Inertia contributions from this type of technical solution are still limited today [25].

The SC has a typical inertia constant H between 1.3 to 2 s. H can be increased by utilizing a higher machine rating that has a negative impact on losses and cost/MVAr. If the primary purpose of adding an SC is to enhance inertia, a more cost-effective approach would be to incorporate a small SC with a flywheel. This combination can effectively boost inertia while keeping losses to a minimum instead of employing a considerably larger SC that would result in higher losses. Considering that the time constant (H) can extend to 5 to 6 seconds, a 75 MVAr SC will store more energy than a 260 MVAr SC with an H value of 1.7 seconds [25]. However, STATCOM technologies cannot offer inertia support unless they are equipped with energy storage systems, such as batteries or super-capacitors.

The conversion of synchronous generators to SCs is being investigated in various countries. It occurs when synchronous generators cannot economically participate in the energy market and are otherwise decommissioned. For decades, synchronous generating units have been used as SCs in southern Brazil and Tasmania (Australia) hydropower plants. SC mode can be used when MW generation is not required or not possible due to water storage levels [4].

LCC-HVDC connections necessitate a minimum level of short-circuit power and inertia in the connected ac system [26]. Even in a strong system, a fault occurrence can lead to system division or even the formation of islands with an inadequate number of synchronous machines remaining operational. To mitigate these issues, Manitoba Hydro, Canada's large HVDC

transmission user, now has thirteen SCs in place to ensure minimum short-circuit levels, sufficient reactive power, and inertia for the proper operation of LCC-HVDC equipment. Specifically, in the Winnipeg area, the development of remote hydro with HVDC technology termination is carefully regulated due to concerns about frequency stability and excessive fault currents [4].

Sometimes it is considered beneficial to combine several reactive power sources. Each compensator has its advantages and limitations. For example, SC is slow, but curtails first-cycle over-voltage and provides inertia support. A STATCOM is reactive and only operates once over-voltage is detected, and may have limited capability to control the immediate over-voltage. Combining them could exploit the benefits of both. In this regard, the Phoenix project [23] is an innovative project that combines both SC and STATCOM technologies to form the world's first Hybrid Synchronous Condenser (H-SC) system.

Compared to synchronous condenser systems, STATCOMs provide better dynamic voltage support, over-voltage mitigation, power oscillation damping, and power quality enhancement. Studies [25] demonstrate that combining these complementary technologies can exploit their strengths and compensate for their weaknesses. This combination is being developed and shown in the Phoenix project as a viable and beneficial solution for modern power systems. In this system, through a three-winding power transformer, a STATCOM runs in parallel with an SC. In addition to STATCOM and SC operating independently, a coordinated control strategy has been developed between the two components to improve performance and efficiency. The project focuses on coordinating and optimizing the role of the master control system. Various operating modes are available, including MVAr control, voltage control, and a combination of both [27].

A key new development, which will be explored further in this thesis, is a hybrid sys-

tem consisting of a back-to-back medium voltage dc system (MVdc) and a synchronous condenser [28]. The hybrid system exhibits exceptional performance, excelling in handling both voltage and frequency disturbances. This novel configuration significantly enhances the performance of the synchronous condenser across all aspects of frequency support. Simultaneously, it retains the capability to deliver substantial short-circuit current during a "voltage event"—defined as an occurrence, such as a remote or bolted ac fault, that induces a significant deviation in system voltage.

The inherent frequency support of a synchronous condenser has several limitations. A "frequency event" is defined as an occurrence, such as a load rejection or generator trip, that causes the system frequency to deviate. During such events, the frequency variation and Rate of Change of Frequency ($RoCoF$) are typically small, resulting in only a limited exchange of stored energy with the power system. Moreover, the machine's stored kinetic energy cannot be effectively utilized to restore system frequency during deviations from the nominal level, as its inertia opposes frequency variations. Additionally, after under-frequency or over-frequency events, the machine's inertia hinders the swift restoration of frequency to its normal level. The synchronous condenser often experiences electromechanical oscillations or swings following frequency or voltage events, leading to undesirable impacts on system voltage and frequency. Furthermore, as a source of reactive power, the synchronous condenser responds more slowly than power electronic devices, causing potential over-voltage during fault recovery [28].

1.2 New proposed Reactive Power Compensator

The proposed system shown in Fig. 3.4 of Section 3.3.1, combines a synchronous condenser with a pair of Back-to-Back (BtB) converters to offer several advantages. It can potentially provide significantly higher reactive power support than a standalone synchronous condenser in steady-state conditions. It supplies substantial short-circuit current during voltage events, surpassing a standalone SC. Additionally, during frequency events, it can supply or absorb active power proportionally to the inertia, with active power capabilities much higher than a regular synchronous condenser of the same MVA rating and H constant. It can also adjust power output based on the power system's requirements during under- or over-frequency situations. Moreover, it supports frequency restoration without opposing the frequency change and can provide active power support if needed. Fast voltage recovery after a fault is achieved through the converter's voltage/reactive power controller, which optimizes support using the converter and SC capabilities [28].

Due to these valuable features, utilizing this novel SC in the LCC-HVDC system could potentially alleviate the operating challenges arising when HVDC terminals are connected to weak ac systems, which are so common these days.

1.3 Research Objectives and Contributions

1.3.1 Research Objectives

- To investigate voltage and frequency support afforded by various reactive power apparatuses, such as synchronous condensers as well as BtB-SC in weak ac systems connected to an LCC-HVDC transmission system.

- To develop an optimal controller strategy by investigating the impact of various BtB-SC control modes. The proposed strategy is dynamically selected during a disturbance to enhance the transient rotor angle stability of ac grid generators during solid three-phase faults of varying durations.

- To optimize the controller parameters of BtB-SC to achieve the fastest possible frequency recovery while ensuring that the frequency nadir does not fall below the minimum threshold defined by the grid code, the RoCoF remains within acceptable limits, and the converters do not hit their operational limits.

- To enhance an inertia measurement method originally proposed in [29] to estimate the inertia of BtB-SC and investigate its frequency support performance.

1.3.2 Summary of Contributions

- This work develops and evaluates a novel topology that integrates a rotating synchronous condenser (SC) into an ac bus through a back-to-back (BtB) voltage-source converter (VSC) link (BtB-SC). During normal operation, the SC is synchronously connected to the grid while the VSCs operate as two STATCOMs. Compared with standard standalone synchronous condensers, this configuration provides enhanced reactive power support, superior voltage regulation, faster voltage recovery, and a greater contribution to short-circuit current during voltage disturbances.

- This thesis investigates the performance of the BtB-SC topology under frequency transients. Upon detecting a frequency disturbance, the synchronizing link between the synchronous condenser and the grid is decoupled. This allows the machine to operate asynchronously, thereby enabling greater kinetic energy exchange with the power

system. The results demonstrate that this configuration significantly enhances the system's transient and rotor angle stability margins during severe disturbances. Furthermore, dynamically adjusting the virtual inertia during the recovery phase further improves frequency regulation.

- The proposed topology demonstrates significant advantages over a standalone synchronous condenser for frequency regulation. By decoupling the synchronous condenser from the grid, the asynchronous connection effectively increases virtual inertia and substantially reduces the Rate of Change of Frequency. In addition to inertia support, the developed controller enables the BtB-SC to enhance the damping of electromechanical modes, thereby minimizing frequency deviations and increasing the frequency nadir. To maximize these benefits, the controller parameters are optimized using a genetic algorithm, resulting in a substantial improvement in overall dynamic performance.

- This work presents an online inertia estimation technique for inverter-based resources based solely on local bus frequency measurements. Validated for both Grid-Forming (GFM) and Grid-Following (GFL) topologies, the method delivers precise inertia estimates at the converter terminal. A key advantage of this approach is its applicability to black-boxed IBR systems, enabling accurate estimation without requiring access to internal controller parameters or proprietary vendor models.

1.4 List of Publications

[1] **NZ Shahraki**, M Mohaddes, K Dey, A. M Gole, "Enhancing inertia and voltage regulation using converter-interfaced synchronous condensers at LCC-HVDC terminals," *in IET Conference Proceedings CP918*, IET, 2025, pp. 357–362.

[2] **NZ Shahraki**, A. M Gole, M Mohaddes, C Karawita, "Transient stability enhancement using converter-interfaced synchronous condenser at LCC-HVDC terminals," *CIGRE 2025 International Symposium Palais des Congrès de Montréal, Québec*, Canada, 2025.

[3] **NZ Shahraki**, K Dey, T Lin, A. M Gole, "Online inertia estimation of inverter-based resources using bus frequency measurement," Electric Power Systems Research 252, 112306, 2026.

[4] **NZ Shahraki**, JS Acosta, A. M Gole, M Mohaddes, "Optimized virtual inertia control for frequency regulation at LCC-HVDC terminals using converter-interfaced synchronous condenser," Electric Power Systems Research 262, 113616, 2027.

1.5 Thesis Organization

The thesis is organized into six chapters.

Chapter 1 presents an introduction and outline of the thesis. The research motivation and the objectives were elaborated. A literature review on the LCC-HVDC system, its challenges when connected to a weak ac grid, and the existing mitigation solutions were also presented in this chapter. The organization of the rest of the thesis is presented below.

Chapter 2 introduces LCC-HVDC and VSC-HVDC transmission schemes, providing a comprehensive exploration of their equipment, operation principles, and control systems. A symmetrical monopole LCC-HVDC transmission system with practical specifications is developed in the electromagnetic transients (EMT) simulation program PSCAD/EMTDC.

Chapter 3 addresses the stability challenges of LCC-HVDC systems connected to weak ac grids and the role of compensators like synchronous condensers and STATCOMs in miti-

gating these issues. It specifically evaluates a novel topology where a synchronous condenser is interfaced via a back-to-back VSC link. By decoupling the condenser's mechanical inertia from the grid, this configuration significantly enhances transient and rotor angle stability during severe disturbances.

Chapter 4 uses PSCAD/EMTDC simulations to demonstrate that the proposed BtB-SC topology offers substantial advantages over a standalone synchronous condenser during voltage and frequency disturbances. The BtB-SC facilitates faster recovery by delivering significantly higher reactive power. Furthermore, the asynchronous grid connection enables larger energy exchanges, resulting in higher apparent inertia, reduced frequency deviations, and a lower $RoCoF$. Ultimately, genetic algorithm optimization of the active power controller parameters ensures superior dynamic performance by synergistically maximizing both inertia and damping.

Chapter 5 enhances an inertia measurement method originally proposed in [29] based on bus voltage frequency signal as a suitable replacement of the virtual speed signal. Using an EMT simulation, the performance of the proposed inertia measurement method is first validated with the example of a synchronous machine with known inertia. It is then extended to analyze the inertia response of BtB-SC and Grid-forming IBR systems.

Chapter 6 summarizes the contributions and conclusions of this thesis and outlines recommendations for future work.

Chapter 2

High Voltage Direct Current Transmission Schemes

This chapter introduces various types of converters used in HVDC power transmission, i.e., Line-Commutated Converters (LCC) and Voltage Source Converters (VSC). The LCC-HVDC and VSC-HVDC transmission systems are briefly described in terms of their components, converter structures, control strategies, and operational principles.

2.1 AC Systems

HVDC transmission systems either take power from (rectifier operation) or feed power into (inverter operation) an ac network. As mentioned in the previous section, the ability of an LCC to operate properly [30] depends on the "strength" of the ac system. A "strong" system is one where the ac voltage magnitude is not significantly affected by the power being exchanged.

Short-circuit ratio (SCR) and effective short-circuit ratio (ESCR) indices are widely used

as indicators of the strength of an ac system. The SCR is defined as the short-circuit capacity of the ac converter bus divided by the active power of the converter, as given in (2.1) & (2.2). With the presence of ac filters, the system behaves as though it is weaker, so an ESCR is defined, whose value is lower than the SCR and considers the MVAr rating of the ac filters, as shown in (2.3). Typically, an ac system with an ESCR of 2.5 or more is considered a strong system, and one with a smaller SCR is referred to as a weak system and is expected to have more trouble with over-voltage on load rejection, successful commutations, and so on.

As shown in Fig. 2.1, the ac system is located at the rectifying end of a single-infeed HVDC system, and the terms SCR and ESCR can be defined as follows [31].

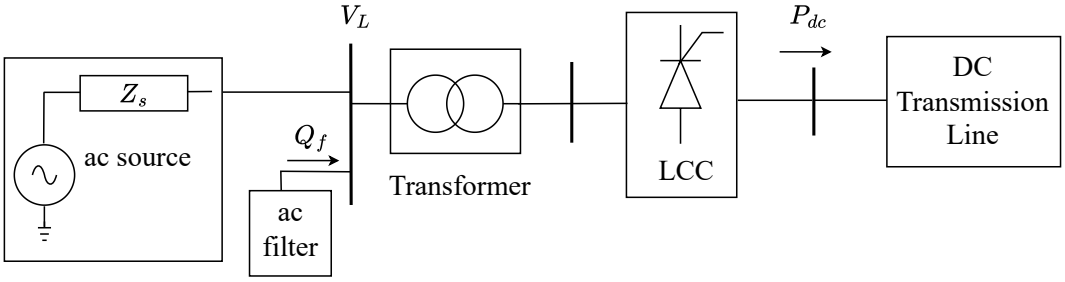

Figure 2.1: Rectifier-side ac system

$$SCMVA = \frac{{V_L}^2}{Z_S} \tag{2.1}$$

$$SCR = \frac{SCMVA}{P_{dc}} \tag{2.2}$$

$$ESCR = SCR - \frac{Q_f}{P_{dc}} \tag{2.3}$$

where $SCMVA$ (MVA) is the short-circuit power of the ac system at the ac busbar of the converter, V_L (kV) is the line voltage, P_{dc} (MW) is the rated dc power, and Q_f (MVAr) is the reactive power of the ac filter at rated voltage. Based on its $ESCR$ value, an ac system can be categorized from very weak to very strong. An ac system with a higher $ESCR$ is typically more robust, making it easier to control. According to the $ESCR$, the following are approximate ranges for weak and strong system designations [32].

- $ESCR < 1.5$ pu : Very weak system
- 1.5 pu $\leq ESCR < 2.5$ pu : Weak system
- 2.5 pu $\leq ESCR < 5$ pu : Strong system

2.2 LCC-HVDC Transmission Schemes

Line-commutated converter-based high-voltage direct current (LCC-HVDC) transmission systems, also known as conventional HVDC, are currently the most widely-used dc transmission systems [33, 34]. In LCC-HVDC systems, the semiconductor device used in the converter blocks is a thyristor, a naturally commutated device capable of blocking high voltages (up to 10 kV) and carrying high currents (6 kA) [35,36]. Note that due to the isolation provided by the dc connection, the rectifier- and inverter-side ac networks do not need to be synchronized with each other and can even have different frequencies of operation (for example, 50 Hz to 60 Hz) [30, 33, 37]. HVDC systems are available in various configurations, including monopolar, bipolar with one 12-pulse valve group per pole, bipolar with

two 12-pulse valve groups per pole, back-to-back bipolar, multiple-terminal, etc., depending on the application [38]. Fig. 2.2 shows a schematic diagram of a 12-pulse monopolar line-commutated converter-based high-voltage direct current (LCC-HVDC) transmission system. The system layout shown in this diagram is used as a case study in this research.

The power is sent from the ac side into the dc side at the rectifier end (sending end) and from the dc side to the ac side at the inverter (receiving) end. The HVDC power converter is designed to operate at high voltages, high currents, and, as a result, high power levels. For this reason, many thyristors are connected in series or parallel to form one "valve" in the power converter and achieve the required currents and voltages [39, 40].

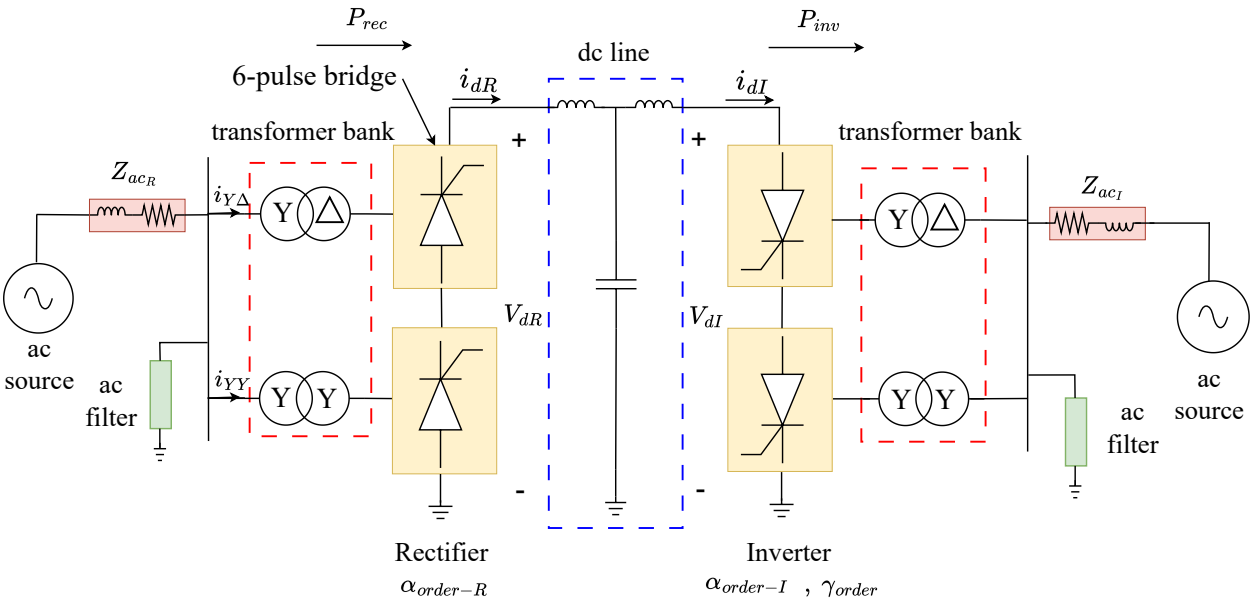

Figure 2.2: A 12-pulse LCC-HVDC transmission system

A strong synchronous voltage source is needed for the LCCs to commutate (i.e., to transfer the current from one phase to another) in a synchronized firing sequence of the thyristor

valves. It can be shown [33] that the LCCs always operate with a lagging power factor and thus demand reactive power at the ac busbar. Under full load, the reactive power consumption is typically 50–60% of the active power consumption. Reactive power consumption varies according to the loading condition. As a result, reactive power compensation is typically provided near the converters, some of it by the ac filters and the remainder by shunt capacitors, synchronous compensators, or other reactive power devices [41].

2.2.1 Operation Principles of Line Commutated Converter

The three-phase, full-wave bridge, called a 6-pulse or Graetz bridge, as shown in Fig. 2.3 is the basic building block of an LCC. The thyristor valves can only conduct in the forward direction, i.e., current flowing from anode "A" to cathode "K."

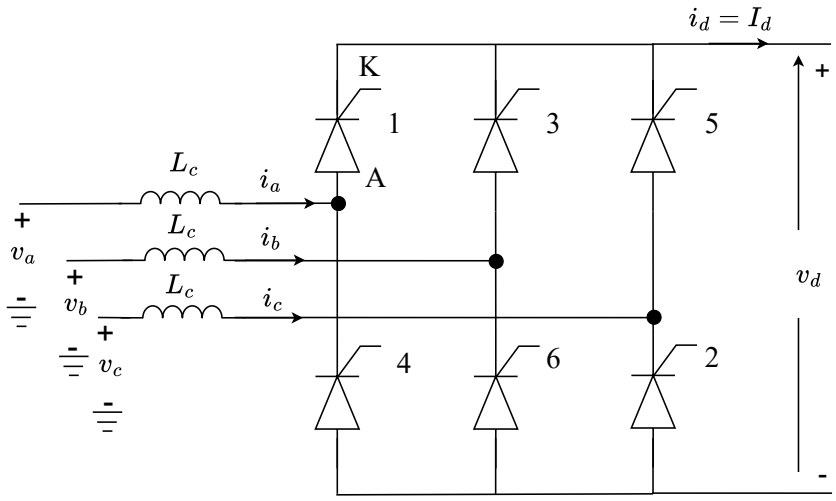

Figure 2.3: Graetz bridge: a three-phase 6-pulse full-wave bridge converter

The LCC achieves control by regulating the firing angle on both the rectifier and inverter sides. Turning on a thyristor is achieved by providing a firing pulse at its gate when its anode

to cathode voltage is positive, i.e., the valve is forward biased. The angular delay from the point of forward bias to the point of firing pulse issue is termed the "delay" or "firing" angle α. Typically, the valves are fired in a symmetrical sequence, i.e., T_1, $T_2 \ldots$ T_6, T_1, and so on. However, it only turns off when the commutating ac voltage becomes negative. No turn-off order is given to the valve turning off. Instead, the turnoff is initiated by providing a firing pulse to the next valve in the firing sequence. The turn-off is not instantaneous, as it takes a finite interval for the current to reduce from its conducting value of I_d to zero. During this time, the offgoing valve gradually transfers its current to the ongoing valve. The angular measure of this interval is the "overlap" angle μ. Also, after the current in the valve extinguishes, this negative voltage (i.e., reverse bias) must be maintained for a specific minimum period. The angular span of this negative voltage is referred to as the extinction angle γ. Having too short an extinction angle can cause the valve to re-ignite spontaneously, even without a firing pulse. This misoperation is called a "commutation failure" and must be avoided as much as possible.

The dc side of LCC-HVDC systems has large smoothing reactors to ensure that the steady-state dc line current is essentially constant ($i_d \approx I_d$) with the minimum ripple. Control operation maintains the dc current at its desired value. The smoothing reactor also prevents lightning surges on the transmission line from entering the converter station and causing damage to the thyristor valves. DC voltage and ac current waveforms of LCC are shown in Fig. 2.4. The commutation period μ shown in Fig. 2.4 (a) exists due to the ac side inductance L_c, which prevents instantaneous changes between current levels. During this period, a nonlinear transition occurs between the two constant boundary values of the ac line current, as illustrated in the same figure.

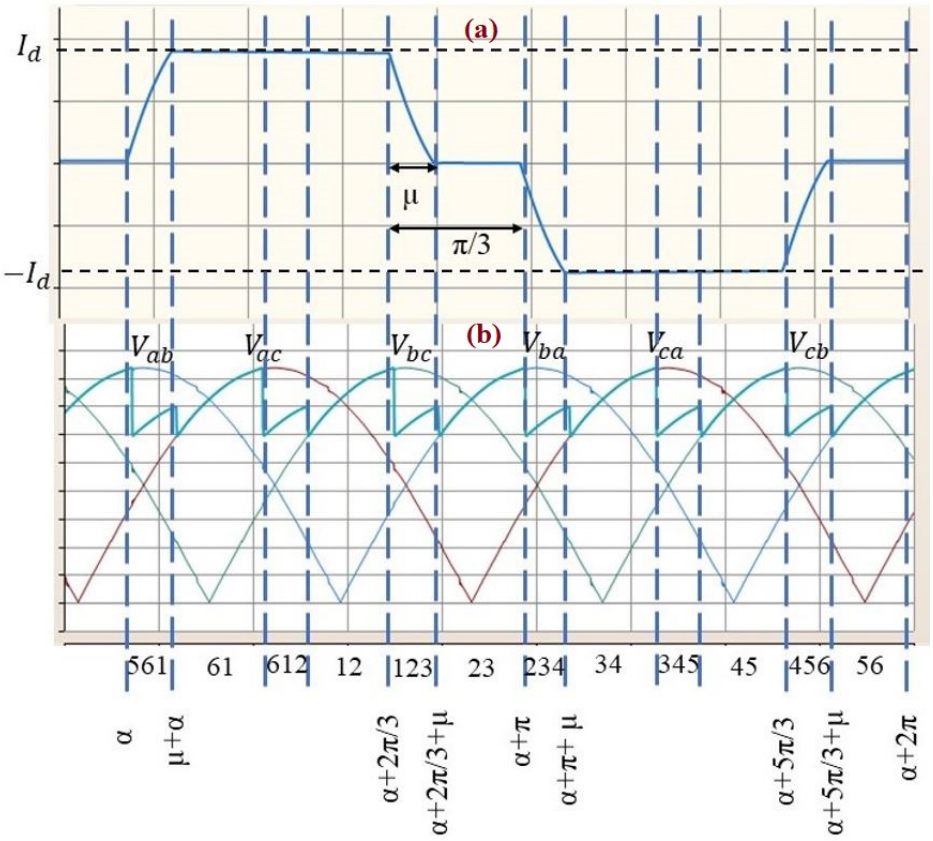

Figure 2.4: Line commutated converter waveforms. (a) three-phase line voltages and the dc voltage; (b) phase-a line current

2.2.2 AC Filters

Harmonics in dc current and voltage can cause additional heating in components such as converter transformers, and also create interference with nearby communication circuits. AC and dc side filters are normally provided to mitigate the harmonics. For a p-pulse bridge, the harmonics of the ac-side current are of the order (np ± 1), and the dc-side voltage harmonics are of the order np, where n = 1, 2,... K^{th}-order harmonics have a magnitude of 1/k of the fundamental component. Graetz bridges are typically connected in series on the dc side and parallel on the ac side to eliminate lower-order harmonics, as illustrated in Fig. 2.5. A

$Y-Delta$ transformer is used to interface the ac side of one bridge, and a $Y-Y$ transformer is used for the ac side of the other bridge. As a result, the 5th and 7th harmonic currents are canceled, and the configuration is known as a 12-pulse bridge [41].

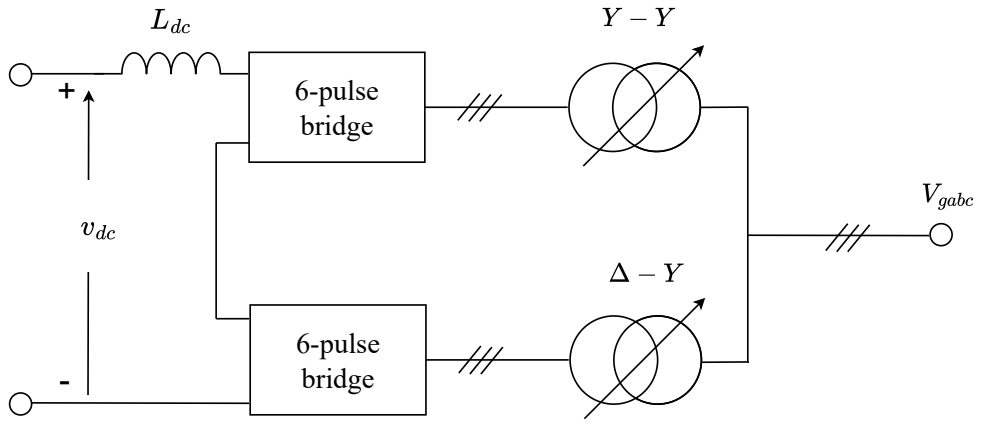

Figure 2.5: Two Graetz bridges connected in series on the dc side and parallel on the ac side. There is one tap-changing transformer with a $Y-Y$ configuration and one with a $\Delta-Y$ configuration

The design of filters is one of the most challenging aspects of an HVDC project. AC filters are typically tuned for a 12-pulse bridge to provide low-impedance paths for the 11th and 13th harmonic currents. Another high-pass filter can eliminate the remainder of the higher-order harmonics. Filters must be designed to ensure an acceptable total harmonic distortion (THD), as well as to meet the standards for telephonic interference, which are usually determined by the telephone influence factor (TIF) [42] under all operating conditions.

2.2.3 LCC Control Systems

Fig. 2.6 illustrates a basic control diagram for an LCC-HVDC system. There are several levels in an LCC-HVDC system.

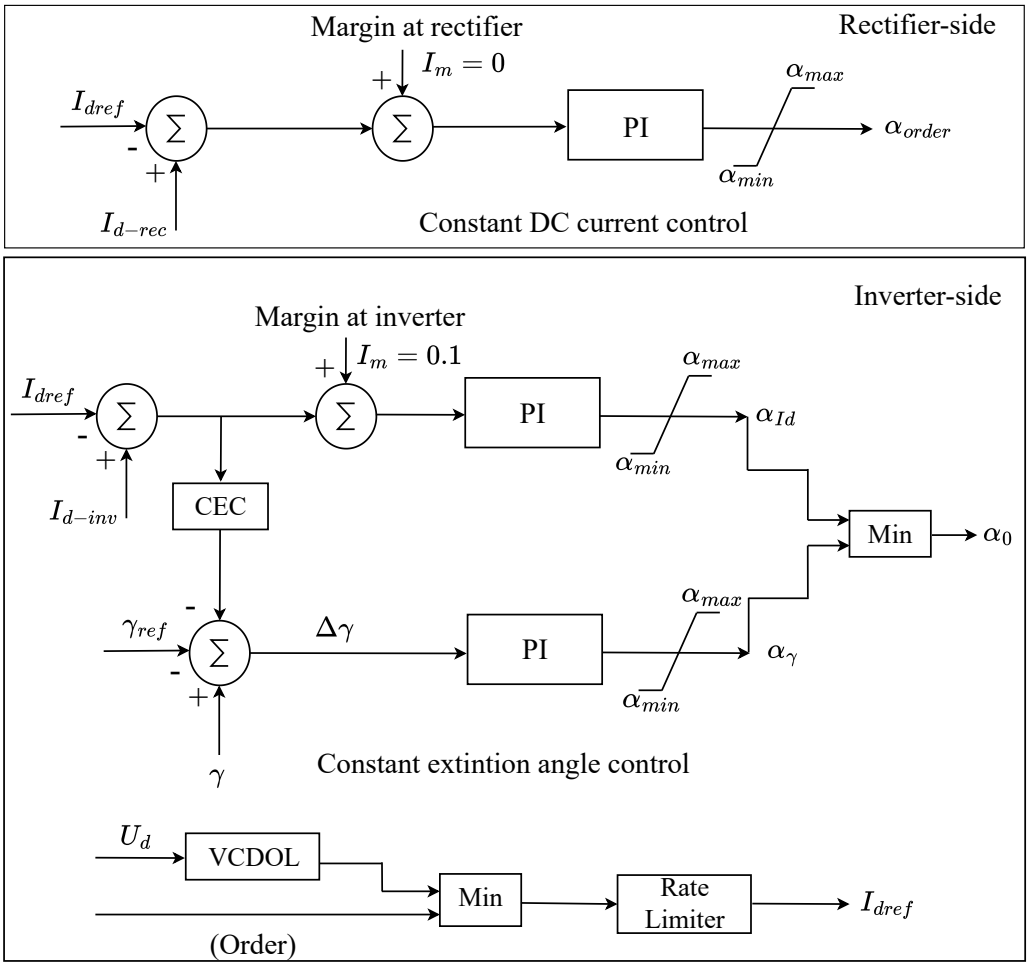

Figure 2.6: Control system of LCC-HVDC system

Typically, the rectifier regulates the dc line current, while the inverter operates in a constant extinction angle control mode. Although additional control functions may be employed for specific modes of operation, under normal conditions, the control of both the rectifier

and inverter can be effectively described using proportional-integral (PI) controllers that act on the dc current and the inverter's extinction angle, respectively. I_{dref} is the reference of dc; I_{d-rec} is the measurement value of the dc, and I_m is the margin current, which is zero on the rectifier side; and α_{max}, α_{min} are the maximum and minimum limited value of the firing angle; I_{d-inv} is the measurement value of dc on the inverter side; γ_{ref} is the reference of the extinction angle on the inverter side; and γ is the measurement value of the extinction angle on the inverter side. The voltage-dependent current order limit (VDCOL) controller is employed to limit the dc current order during ac under-voltage conditions to protect the valves [1, 6]. To ensure the correct timing of firing pulses to the converters, phase-locked loops (PLLs) are used at both ends. The modeling of the PLL is detailed in the following section.

2.2.4 Phase Locked Loop (PLL)

A phase-locked loop (PLL) is a control system for tracking the phase angle of the fundamental positive-sequence component of an ac waveform. It can synchronize an output signal with a distorted input signal that may vary (within certain limits) in amplitude, frequency, and phase.

Various types of PLLs are currently used in HVDC schemes worldwide [43]. They follow the same operating principle, but their main difference is in phase angle measurement. This research utilizes the widely used D-Q-Z type PLL [44], shown in Fig. 2.7. A voltage-controlled oscillator (VCO) within the PLL generates a reference angle θ of 0° to 360°, which is used to fire the converter valves. A PI controller utilizes the phase angle error between the ac system voltage (positive sequence, phase A) and the reference ramp θ is used to determine the frequency of the voltage control oscillator. A properly designed system quickly achieves an

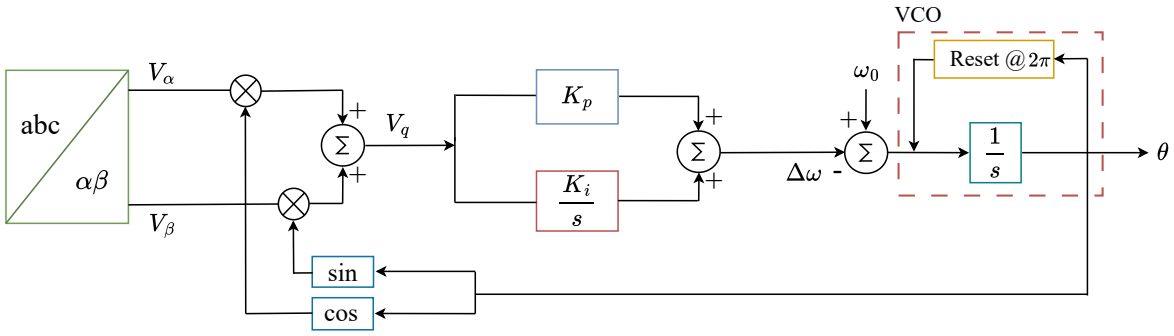

Figure 2.7: Block diagram of PLL

equilibrium where there is no phase angle error, ensuring that the phase-A positive sequence voltage of the input voltage is in perfect synchronism with the angle θ [44].

2.3 VSC-HVDC Transmission Schemes

The voltage source converter (VSC) is a modern technology that uses gate turn-off devices such as insulated gate bipolar transistors (IGBTs) as the basic switching element. Unlike the LCC, the VSC valves are more versatile as they can be turned off by external command. This capability allows the VSC to generate its own voltage waveforms independently of the ac system. While offering superior flexibility, the current power ratings of VSC systems are still lower than those attainable with LCCs. Common VSC structures include the two-level VSC, three-level VSC, and modular multilevel converter (MMC) [38, 45].

2.3.1 Two-level Voltage Source Converter (VSC)

A three-phase VSC is constructed using three half-bridge converters (see Fig. 2.8). A bridge consists of six switches, each comprising an IGBT and an antiparallel diode. Although to reach higher voltage ratings necessary for transmission (in the range of hundreds of kilovolts),

several IGBT devices and anti-parallel diodes are typically connected in series to constitute the"valve" [46].

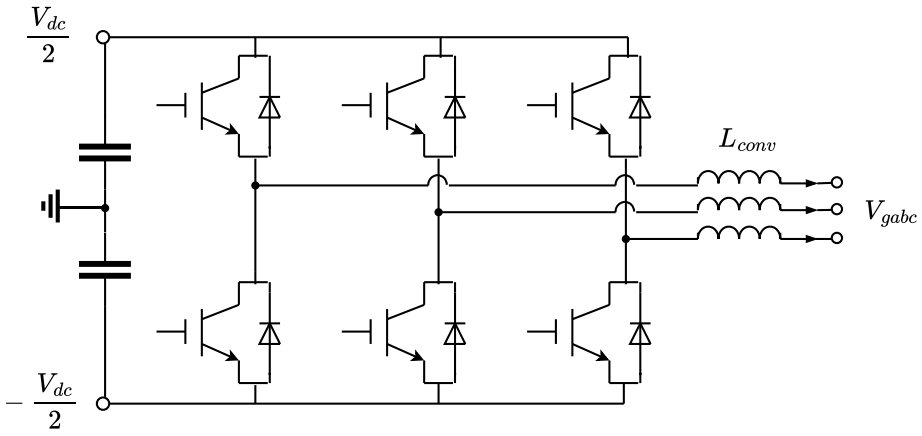

Figure 2.8: A three-phase, 2-level, 6-pulse bridge configuration of a VSC with IGBTs coupled with anti-parallel diodes

Each phase in this converter can generate either a voltage of $+\frac{V_{dc}}{2}$ (when the top switch is on) or $-\frac{V_{dc}}{2}$ (when the bottom switch is on), naming it a two-level converter. Utilizing a PWM technique commonly generates a symmetric sequence of such $\pm\frac{V_{dc}}{2}$ pulses at the converter outputs. The width of the pulses is manipulated to obtain the desired fundamental and harmonic spectrums [38, 47]. Fig. 2.9 shows an example waveform for the output phase-to-neutral voltage. Since self-commutated converters employ IGBT, there is no commutation circuit, and the associated problems are experienced in conventional HVDC converter blocks. Therefore, weight, efficiency, and voltage control range are improved [2,46]. The VSC switches are typically switched at a frequency of 1-2 kHz in power systems applications. Although higher switching rates are available in low-power applications such as motor drives, they are avoided in bulk power converters to minimize switching losses.

No matter what direction the ac current flows, VSCs can control the magnitude and

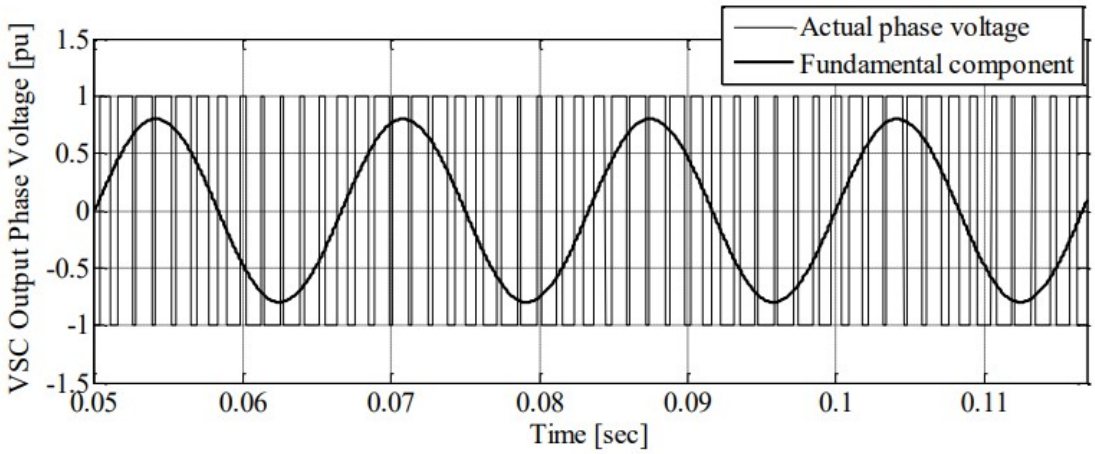

Figure 2.9: Two-level VSC output voltage

phase angle of the ac voltage V_{gabc} (Fig. 2.8). This allows independent control of the ac system's active and reactive power exchange [41].

2.3.2 Modular Multilevel Converter (MMC)

The MMC topology is a VSC topology for high-power and high-voltage applications, which can also be employed for HVDC transmission [48], FACTS [49], and so on.

The schematic diagram of a single-phase MMC is shown in Fig. 2.10 (a). Each arm comprises multiple identical modules, which can either be of the half-bridge or full-bridge type. By applying appropriate switching signals, it is possible to achieve the desired ac terminal voltage. Compared to a two-level VSC, the MMC features lower losses and can produce an almost harmonic-free ac voltage waveform. The dc capacitors are distributed within each module, with the MMC constructed from cascade-connected modules. As a result, the ac terminal voltage can achieve various voltage levels, depending on the number of modules.

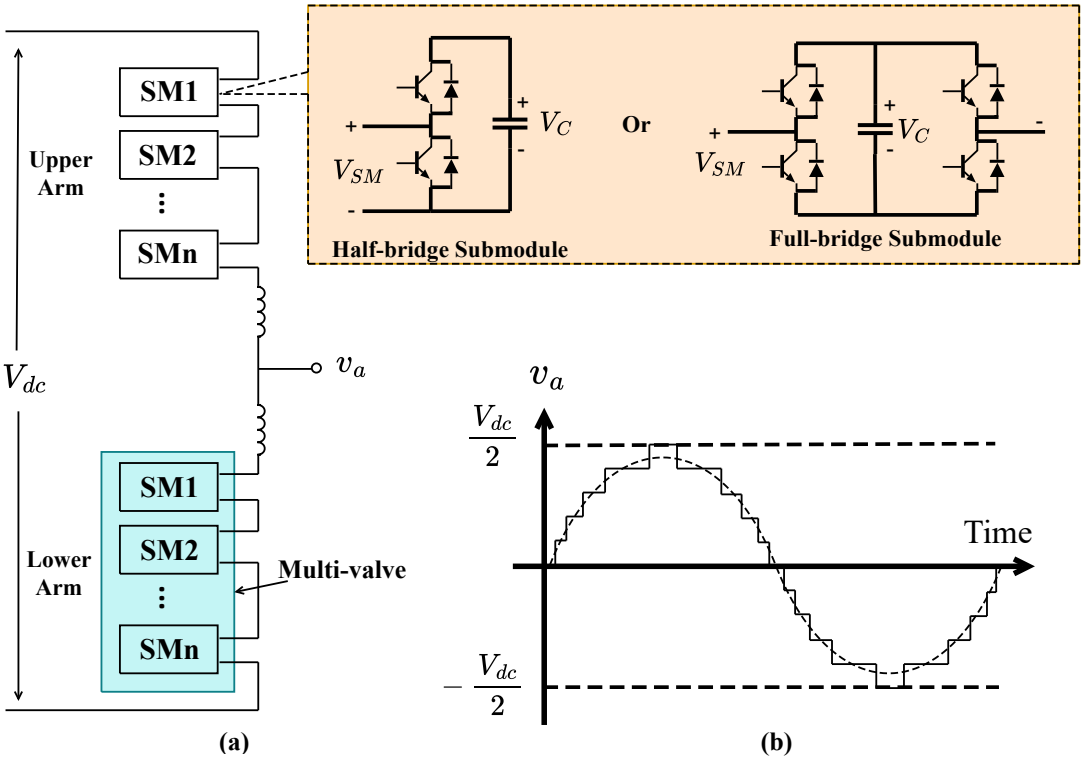

Figure 2.10: (a) Half-bridge or Full-bridge Schematic Diagram of a One-phase MMC. (b) Schematic Diagram of MMC Output Voltage Waveforms.

The modular structure of the MMC is well-suited for practical operation as its design can be adjusted by adding or removing submodules to match the desired rated voltage for a specific scheme. This obviates the requirement for custom design, which are typically required for LCC-based applications. During operation, the ac voltage waveform is produced by either adding or bypassing specific modules in the arm, as illustrated in Fig. 2.10 (b). With numerous levels, the stepped output waveform can closely approximate a sine wave, effectively eliminating the need for filters.

Conversely, compared to the two-level VSC, the MMC features a more complex structure, and its control system design is more complicated. Additional control mechanisms are

required to balance the voltages across each submodule's capacitance(utilizing a capacitance voltage balancing controller), and to suppress circulating current (through a circulating current suppression controller known as CCSC).

2.3.3 VSC Converter-level Control

Here, only the higher-level controllers for any VSC (whether MMC or two-level VSC) are discussed. Typically, VSC control modes can be classified as either grid following (GFL) or grid forming (GFM).

Grid-Following Strategy

The grid-following control method is a widely used technique for converter control, allowing converters to synchronize their generated voltage waveform with the grid voltage waveform using a phase-locked loop. However, in high-impedance ("weak") grid situations, the grid-following method can struggle with sudden phase shifts and poor tracking, leading to operational fluctuations and potential instability.

The VSC grid-following control scheme is illustrated in Fig. 2.11 [45]. The outer loop controller is shown in a configuration for controlling the real power (P) or dc link voltage (V_{dc}) and the ac rms voltage (V_{ac}) or reactive power (Q). These controllers regulate either the active power or dc link voltage (via I_{d1-ref}), ac voltage, or the reactive power (via I_{q1-ref}). The outer loop controllers provide the current references I_{d1-ref} and I_{q1-ref} to the inner loop current controllers. These currents are fed into a current limiter, which imposes maximum constraints on their magnitudes to prevent overcurrent conditions. The limited currents I_{dref} and I_{qref} are passed to a decoupled current controller that generates the voltage orders v_{cd} and v_{cq} for the VSC so that the order currents are achieved. The terms v_{td} and v_{tq} represent

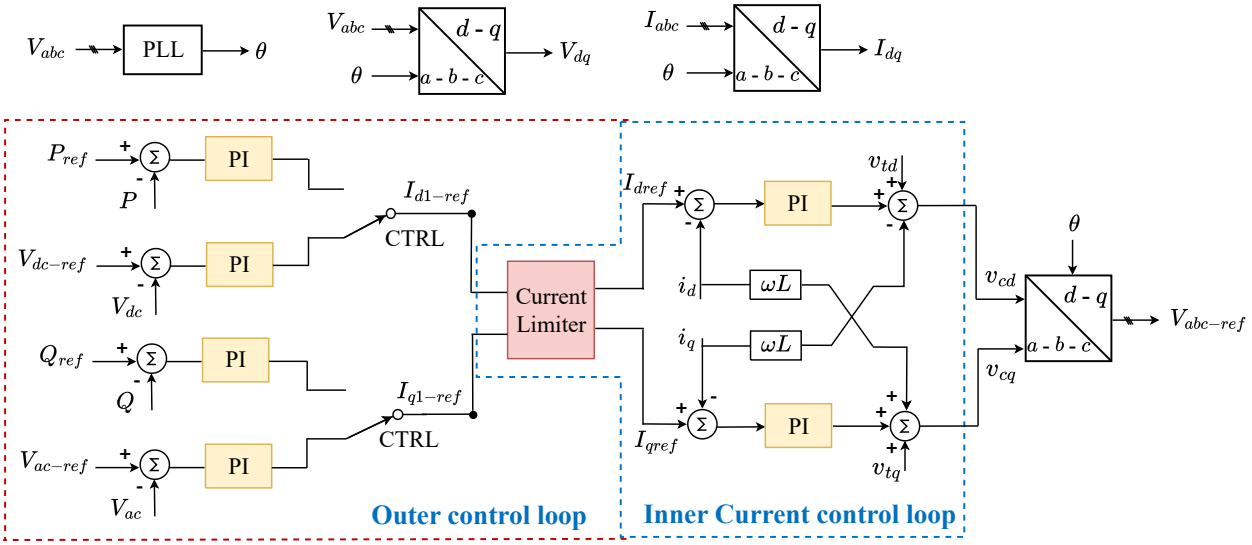

Figure 2.11: Grid-following control diagram of VSC-HVDC including inner and outer controllers

the d- and q-axis voltages of the PCC, and ωL is the reactance between converter valves to the PCC bus.

Grid-Forming Strategy

The grid-forming (GFM) control method is a recent advancement in converter control [50]. Unlike the traditional grid-following (GFL) strategy, where converters synchronize with the grid's voltage and frequency, GFM generates its own output voltage and frequency. This makes it suitable for connecting to purely passive loads or very weak systems. The magnitude and phase of the generated voltage are continuously adjusted to provide the desired real and reactive power. This innovative approach allows converters to establish a new grid reference and actively shape the network's voltage and frequency, enabling them to initiate and sustain a stable grid even when the main grid is unavailable or unstable. GFM offers

potential benefits in enhancing grid resilience, supporting microgrid operations, and ensuring a reliable power supply from renewable sources.

- Droop-based Control Strategy for GFM

  Droop-based control is one of the basic GFM strategies to control the terminal voltage and the frequency of the VSC side (V_{gabc} in Fig. 2.8) [51, 52]. This control strategy needs voltage and current feedback from the ac network.

  The power flow equations are defined as follows. In (2.4) & (2.5), E represents the voltage magnitude at the sending point, and V is the voltage magnitude at the receiving point. The angle difference between these two voltages is denoted by δ, and X is the line reactance between them. P and Q refer to the active power and reactive power flow from the sending point to the receiving point, respectively.

$$P = \frac{VE}{X} \sin \delta \tag{2.4}$$

$$Q = \frac{E^2}{X} - \frac{VE}{X} \cos \delta \tag{2.5}$$

  When the transmission line resistance is ignored, the active power P changes with the power angle $\delta = \int(\omega - \omega_0)\ dt$, where ω_0 is the nominal frequency. On the other hand, reactive power Q is more sensitive to voltage magnitude. Therefore, active power P depends on system frequency (ω), while reactive power Q depends on voltage magnitude. Assuming a linear relationship, the following characteristic equations can be established: Equations (2.6) & (2.7) define the $P - \omega^*$ droop and $Q - E^*$ droop characteristics, respectively. Here, E^* and ω^* are the reference voltage and frequency,

while ω_0, E_0, P_0, and Q_0 are the steady-state values of frequency, terminal voltage, active power, and reactive power. Variables m and n are the droop constants.

$$\omega^* = \omega_0 - m(P_0 - P) = g(P) \tag{2.6}$$

$$E^* = E_0 - n(Q_0 - Q) = f(Q) \tag{2.7}$$

The control block is shown in Fig. 2.12. The V_{ref} is equal to E^*, and δ_{ref} can be calculated by integrating the reference frequency ω^*.

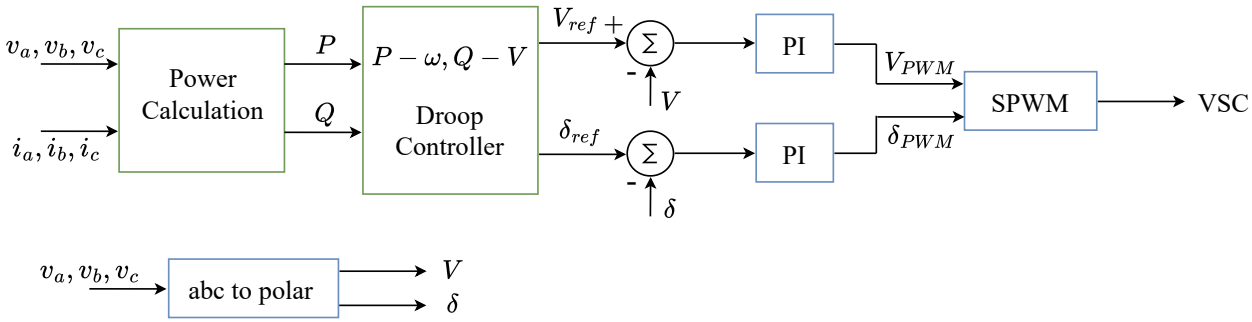

Figure 2.12: Droop Control Structure

Additionally, this control strategy is suitable for both grid-connecting and islanding modes. However, since the controller is in voltage-source control mode, there is no inherent current limiting. Also, there are steady-state errors in frequency and voltage.

- Virtual Synchronous Generator (VSG) Control

  As inverter-based distributed energy sources (DES) replace conventional synchronous

generators, system inertia declines, making the grid more susceptible to rapid frequency changes, oscillations, and instability. The Virtual Synchronous Generator (VSG) is a GFM control strategy that configures power electronic converters to emulate the dynamic behavior of synchronous generators (SGs). Synchronous generators inherently provide high inertia due to their rotor mass, which enhances the damping of frequency oscillations and supports system stability during transient events [53]. By mimicking these characteristics, VSG-controlled converters can contribute synthetic inertia and controlled damping, helping stabilize grid frequency and mitigate oscillatory disturbances when transients occur.

Various Virtual Synchronous Machine (VSM) models [54–57] have been developed with differing accuracy in replicating synchronous machine behavior. This discussion focuses on simplified VSMs that use the swing equation to regulate converter power, as shown in (2.8).

$$J\ddot{\theta} = T_m - T_e - D\Delta\dot{\theta} = \frac{P_m}{\omega} - \frac{P_e}{\omega} - D\Delta\dot{\theta} \tag{2.8}$$

In (2.8), ω denotes the synchronous angular velocity, and θ represents the synchronous phase angle. The mechanical power P_m of the synchronous machine corresponds to the converter's power reference, while the electrical power P_e represents the measured power at the point of common coupling (PCC). The mechanical torque T_m and electrical torque T_e are proportional to their respective powers, such that $T_m = \frac{P_m}{\omega}$, and similarly for T_e. For machines operating near synchronous speed—a typical condition—these relationships simplify to $P_m \approx T_m$ and $P_e \approx T_e$ in per-unit terms. Here, J is the inertia constant and D is the damping coefficient. In a VSM, both inertia and damping are

synthetic parameters that can be tuned or even adapted dynamically. This differs from a real synchronous machine, where inertia and damping are fixed by the rotor's physical mass, damper winding characteristics, mechanical friction, and windage losses, and therefore cannot be arbitrarily adjusted. The VSM provides additional control flexibility, including the possibility of adaptively modifying these constants during operation.

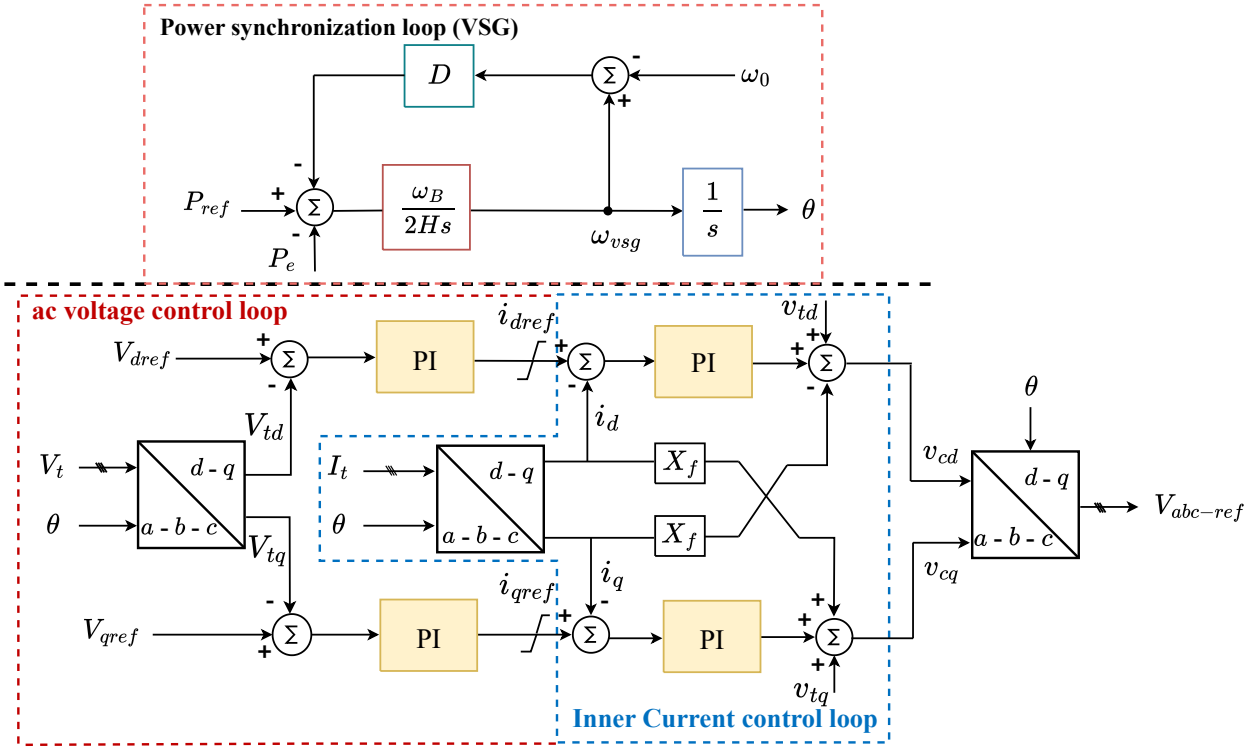

Figure 2.13: VSG control structure

Fig. 2.13 shows the VSM control diagram. The power synchronization loop emulates the swing equation of a synchronous machine and generates the ac voltage synchronization angle θ at the PCC. The ac voltage magnitude at the PCC is generated by the ac voltage control loop through either an ac voltage controller or a reactive power controller. This control

function closely resembles the automatic voltage regulator (AVR) in a synchronous machine, regulating the voltage to maintain stability and proper operation of the power system.

2.4 Summary

This chapter presented the operating principles of HVDC transmission schemes, focusing on line-commutated converter (LCC-HVDC) and voltage source converter (VSC-HVDC) technologies, and provided a comprehensive overview of their key equipment and control systems. It also explains how ac system strength is measured using the SCR and ESCR indices and what impact these indices have on converter operation.

Chapter 3

Enhancing Transient Stability in Weak LCC-HVDC Systems Using the Converter-interfaced Synchronous Condenser

This chapter investigates the capability of the converter-interfaced synchronous condenser arrangement in enhancing transient stability and voltage support when connected at the ac busbar of a Weak LCC-HVDC System. To provide a fair comparison, I first investigate how other options, such as STATCOM, provide these features, and then investigate the proposed Back-to-back Synchronous Condenser (BtB-SC) approach.

Power system stability refers to the system's ability to maintain equilibrium during normal operation and to return to an equilibrium state after a disturbance [53]. Rotor angle stability is associated with the electro-mechanical modes and is a key index used in power

systems analysis [53, 58]. Rotor angle stability can be of two types:

- 1) Transient Stability: Transient stability is associated with the power system's regaining a steady-state following a significant disturbance, such as an ac fault. Instability is indicated by an angular separation between synchronous machines.
- 2) Small Signal Stability: A system that is small-signal stable maintains a stable operating point following small perturbations. It allows the use of linearized system models for analysis [59].

Assuming the network configuration remains unchanged in a stable power system, the system returns to its original operating point following a disturbance. A stronger stability condition is that the system settles into a new stable operating state without loss of synchronism, even if the disturbance results in a change in the network structure [60]. For continuous and stable operation of the power system, it is essential to maintain synchronization among the angles of all synchronous machines. This synchronization is governed by the "swing equation" that relates generator rotor speed and rotor angles to the generator power [59–61].

With the increasing penetration of renewables, HVDC connections now constitute a significant portion of modern power grids. HVDC lines asynchronously interconnect ac networks and enable harnessing renewable generation. The introduction of HVDC converters is resulting in both challenges and opportunities for improving transient stability. Unlike conventional synchronous generators, renewable-based systems have limited inherent inertia, restricting their ability to exchange kinetic energy and provide frequency support [62]. In Canada, many large utilities in Manitoba, Quebec, and Alberta use line-commutated HVDC converters. The active power relationship in a six-pulse converter bridge is approximated as

follows:

$$U_d = \frac{3\sqrt{2}}{\pi} U_{v0} \cos\alpha - \frac{3}{\pi} X_c I_d \tag{3.1}$$

$$P_d = U_d I_d = \frac{3\sqrt{2}}{\pi} U_{v0} I_d \cos\phi \tag{3.2}$$

Line-commutated converters, regardless of their rectifier or inverter operation, consistently consume reactive power, which is expressed as:

$$Q_d = \frac{3\sqrt{2}}{\pi} U_{v0} I_d \sin\phi = \frac{P_d}{\cos\phi}\sqrt{1-\cos^2\phi} = P_d\sqrt{\frac{1}{\cos^2\phi} - 1} = P_d\sqrt{(\frac{3\sqrt{2}}{\pi}.\frac{U_{v0}}{U_d})^2 - 1} \tag{3.3}$$

Here U_d denotes the dc voltage, U_{v0} the transformer valve winding voltage (line to line RMS value), I_d the dc current, α the firing angle, X_c the commutation reactance refers to the valve side of the converter transformer (per phase), P_d the converter dc power, Q_d the reactive power consumed by the converter power factor angle, and ϕ the power factor angle.

Several strategies have been proposed to improve grid transient stability by appropriate control of the HVDC converters. One approach utilizes the fast, flexible control of dc power through techniques such as dc power modulation and rapid power adjustments. Another approach uses margin switching or voltage-dependent current order limits (VDCOL) to maintain dc power close to its scheduled value during ac system disturbances [63]. Other methods include modulating the active dc power via the current reference of the LCC, which can significantly improve oscillation damping [64–66]. However, the impact of any control strategy depends on the disturbance location [67, 68]. It should be realized that incorporating additional control strategies into an existing HVDC system makes the controller more complex and may lead to different control loops working against each other.

Reactive power demand remains a fundamental challenge in LCC-HVDC systems. Compensation is typically achieved using shunt capacitor banks, ac harmonic filters, and, in special cases, compensation devices such as the synchronous condenser (SC) and the Static Synchronous Compensator (STATCOM). The allocation of compensation measures is contingent upon the specific system configuration and prevailing operating conditions [16]. Synchronous condensers provide inertia and frequency stability benefits due to their rotating mass, while STATCOMs offer fast and flexible voltage regulation with continuous reactive power control even under low voltage conditions.

This chapter investigates a promising alternative approach that employs a back-to-back converter interfacing a synchronous condenser (BtB-SC) to the ac bus of an LCC-HVDC system [69, 70]. This hybrid compensator combines the beneficial characteristics of both SCs and STATCOMs to overcome their individual limitations, thereby improving voltage stability, frequency regulation, and overall system robustness in weak ac networks.

3.1 Synchronous Condenser

One of the significant reactive power compensator applications for LCC-HVDC systems has been a synchronous condenser, which is an ac synchronous machine that operates without a prime mover and exchanges zero real power in the steady state with the connected network. Fig. 3.1 shows a simple single-line diagram of a synchronous condenser. SCs can fulfill several needs, including [57]:

- SCs can supply a controllable amount of reactive power needed for the converter.
- This allows the dc converter controller to maintain acceptable ac voltage control where the receiving system's short-circuit capacity is low.

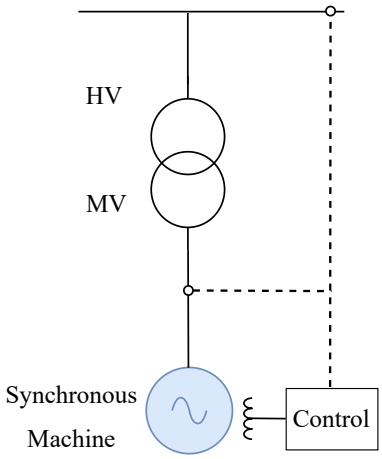

Figure 3.1: Typical Synchronous Condenser Configuration

3.1.1 short-circuit Strength Contribution

The excitation system controls the machine's internal voltage by adjusting the field current, effectively acting as a controllable voltage source behind an inductance. Increasing the field current raises the voltage amplitude and injects reactive power; reducing it lowers the voltage and absorbs reactive power. Typically, these actions are taken in response to alterations in network conditions during severe contingencies, such as faults, to support changing system voltage. Thus, a synchronous condenser can contribute to the short-circuit current in a system [71]. A higher short-circuit capacity is desirable for an LCC converter as it means less variation in ac voltage due to loading changes and also improved immunity against commutation failures [72].

The symmetrical short-circuit current can be approximated by dividing the voltage behind the sub-transient reactance by the sum of the sub-transient reactance, $X_d^{"}$, and the transformer leakage impedance, X_t, while ignoring resistance. The simplified diagram in

Fig. 3.2 corresponds to (3.4).

$$I = \frac{E}{jX_d^{"} + jX_t} \tag{3.4}$$

When the synchronous condenser is floating or has no net VAR output, the terminal voltage V_t and internal voltage E will be the same, usually around 1.0 per unit. When the SC is operating at maximum overexcited condition, the system will receive MVArs, and the voltage of the internal condenser, E, will exceed 1.0 p.u.

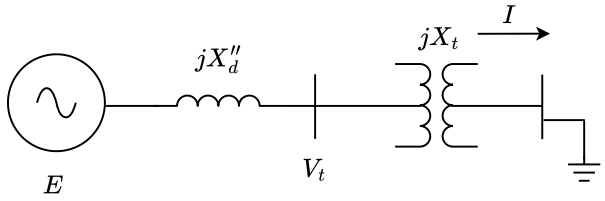

Figure 3.2: Simplified Synchronous Condenser short-circuit Diagram

To enhance the effectiveness of the synchronous condenser in providing increased short-circuit capacity, one way is to minimize the impedance of both the condenser and the transformer. While the sub-transient reactance remains relatively fixed in per unit on the condenser MVA base, the option to further optimize lies in reducing the transformer leakage impedance.

3.1.2 Inertia Contribution

Another favorable characteristic of the synchronous condenser is its rotating inertia. Inertia refers to the quantity of kinetic energy transferred between a synchronous machine and the power system during the acceleration or deceleration of the rotor. This energy exchange

occurs in response to a deviation in the system frequency, effectively counteracting it. Consequently, power systems with higher inertia exhibit a smaller change in rotational kinetic energy when subject to disturbances and consequently less change in the rotor speed, leading to a quantifiably lower rate of change of frequency ($RoCoF$).

An electrical machine's per unit inertia constant H can be defined as the kinetic energy in watt-seconds at rated speed divided by the rated MVA base. The inertia constant H is given by:

$$H = \frac{\text{Stored Energy at Rated Speed in MW} \cdot \text{S}}{\text{MVA Rating}} \tag{3.5}$$

The average inertia constant of a multi-machine power system can be represented as:

$$H = \frac{\sum_{i=1}^{n}(H_i \cdot \text{MVA}_i)}{\sum_{i=1}^{n} \text{MVA}_i} \tag{3.6}$$

Renewable power sources are widely regarded as advantageous for increasing power generation. However, compared to traditional thermal units, they contribute less inertia to the power system. Another noteworthy factor is the rising prevalence of HVDC connections, which necessitate specific minimum short-circuit power and inertia in the connected ac system. To address this concern, synchronous condensers offer approximately 1.5 - 2.5 seconds of conventional inertia levels.

The rate of change of frequency ($RoCoF$) is the time derivative of the power system frequency ($\frac{d\omega}{dt}$) after an imbalance of power in the electrical power system (i.e., disconnection of a generator/load tripping) before the action of any control. It is calculated as follows:

$$\frac{d\omega}{dt} = \frac{(P_m - P_e) \cdot \omega_0}{2 \cdot H} \tag{3.7}$$

Here ω_0 denotes the system nominal frequency in rad/s, H the inertia constant of the machine in MW.S/MVA, P_m the machine's mechanical power in per unit, and P_e the machine's electrical power in per unit.

In system design, ensuring adequate inertia is vital to avoid the frequency surpassing critical thresholds when a major power source in the network, such as HVDC links or heavily loaded generators, experiences a trip. Synchronous condensers emerge as one of the most viable solutions to fulfill this requirement, especially in low-inertia systems.

3.2 STATCOM

With the development of power electronics, the static compensator (STATCOM) has become a popular reactive power source. The STATCOM controls its output reactive power by controlling a voltage behind its reactance, much like a synchronous machine-type static compensator. However, there is no rotating mass, so the maintenance requirements are much reduced, and the upfront capital cost is lower [44]. However, the lack of rotating inertia and its associated kinetic energy storage means that STATCOM cannot provide the same inertia support as an SC unless it is equipped with a battery energy storage system (BESS). Also, it is more prone to damage from overcurrent due to the sensitive nature of the power electronic devices. Choosing between the STATCOM and an SC can be challenging because of these differences. When comparing these devices with similar nameplate ratings, they will show different performances during and after network contingencies [69].

The VSC functions as a controllable voltage source and a series-connected coupling reactor connected to an ac bus. A STATCOM is a special case of the VSC with no power source interfacing with the VSC dc-side terminals, and the dc bus is merely terminated to

the dc-bus capacitor(s), as depicted in Fig. 3.3.

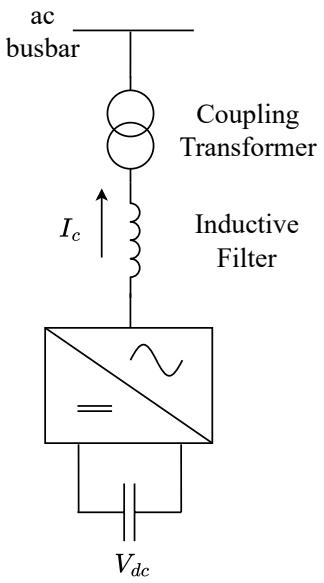

Figure 3.3: Typical STATCOM Configuration

The STATCOM's dc-bus voltage, V_{dc}, is regulated by controlling the real power exchanged with the rest of the system. This active power is very small in the steady state, as it only compensates for the VSC power losses.

The voltage source amplitude is altered to achieve reactive power output similar to a synchronous machine. Each converter consists of multiple dc capacitors linked through power electronics equipped with turn-off capability, such as IGBTs. Due to its switching algorithm, a near-sinusoidal voltage is generated at the converter terminals. This voltage synchronizes with the network voltage sine wave, allowing the STATCOM control system to regulate the current output precisely. From the network perspective, the STATCOM operates as a swift-reacting reactive current source [73].

The STATCOM control block diagram closely resembles that of a grid-following control structure shown in Fig. 2.11. However, since the STATCOM only has a dc-side capacitor,

it cannot provide steady-state real power, although very short-term transient power may be possible depending on its capacitor size. Hence, the power reference order P_{ref} would be nominally zero in the power control application.

Table 3.1: SC and STATCOM Comparison [71]

Features	**STATCOM**	**Synchronous Condenser**
Reactive Power Capability	same inductive and capacitive output	inductive output is ˜60% of capacitive
Overload Capability	125% for 3 seconds	200% for 10 seconds or 150% for 30 seconds
Activation Time to sudden voltage changes	1.5 – 2 cycles	immediately
Contribution to system inertia	No (unless with energy storage)	Yes
Contribution to system short-circuit power.	No	Yes

The inertia of the synchronous machine rotor is a significant factor driving the increased interest in synchronous condenser applications. Implementing a synchronous condenser can contribute to smoother frequency dynamics during frequency events in the system. In contrast to a synchronous condenser, a STATCOM without an additional energy storage system cannot aid in frequency stability. Table 3.1 summarizes the differences between the synchronous condenser and STATCOM technology [74].

3.3 Back-to-back Converter-Interfaced Synchronous Condenser

A promising hybrid solution proposed in [28] combines an SC with a Back-to-Back (BtB) VSC system. This topology offers enhanced performance under significant voltage and frequency disturbances. During voltage events, the SC remains synchronized with the ac grid, and the overall setup delivers/absorbs substantially more reactive power than that of a standalone SC. During frequency disturbances, the SC operates asynchronously with the grid. As synchronism is no longer demanded, the SC provides significantly more frequency support to the ac grid than a synchronously connected SC.

3.3.1 Operating Principle of the Back-to-Back Synchronous Condenser (BtB-SC)

Fig. 3.4 presents the schematic of the BtB-SC system. In this design, an SC is connected to the ac network through two VSCs arranged in a back-to-back configuration. The power rating of the BtB-SC is determined according to the active and reactive power requirements of the ac network during voltage and frequency disturbances. Furthermore, a regular ac circuit breaker, denoted as switch S_1, is incorporated across the BtB converters.

The switch S_1 is opened when a frequency event is detected (e.g., under frequency, over frequency, high $RoCoF$), resulting in the BtB-SC configuration of Fig. 3.4. The grid-side converter remains synchronized with the grid, whereas the SC-side converter is synchronized to the SC frequency, which, due to the asynchronous BtB link, can be different from the ac system frequency. With proper control, a large amount of kinetic energy can be temporarily extracted from or absorbed into the SC in a controlled manner, causing the SC's rotational

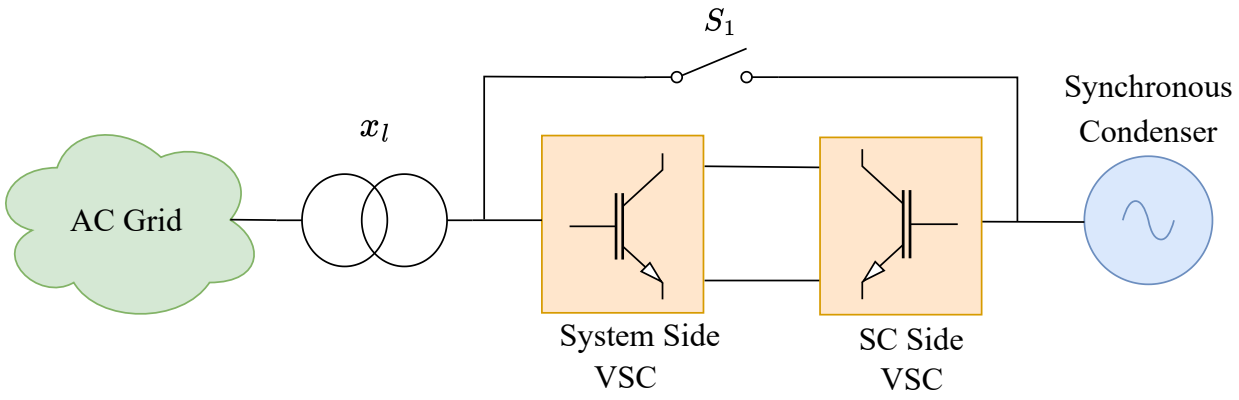

Figure 3.4: BtB-SC Schematic

speed (and terminal voltage frequency) to change. This allows for larger energy amounts to be exchanged with the SC than would be possible with one directly connected and hence synchronous with the ac system. The SC, therefore, appears to have a much larger inertia constant H than a conventional SC, which could be a key factor in supporting ac-side frequency.

During steady state, S_1 is closed, and the SC operates as a normal SC with the rotor rotating at synchronous speed, and the BtB is reconfigured as two parallel STATCOMs, as illustrated in Fig. 3.5. This is called the STATCOM/SC operating configuration. Both VSC converters and the SC can operate in reactive power control mode (Q mode) or voltage control mode (V mode) with properly assigned droops. The system operator determines the voltage and reactive power set points in each mode based on ac system requirements. The system's total steady-state reactive power capacity is equal to the sum of the ratings of the SC plus the two VSCs. This configuration employs the benefits of a hybrid STATCOM-SC system, as proposed in [25], by offering a rapid dynamic response along with short-circuit current.

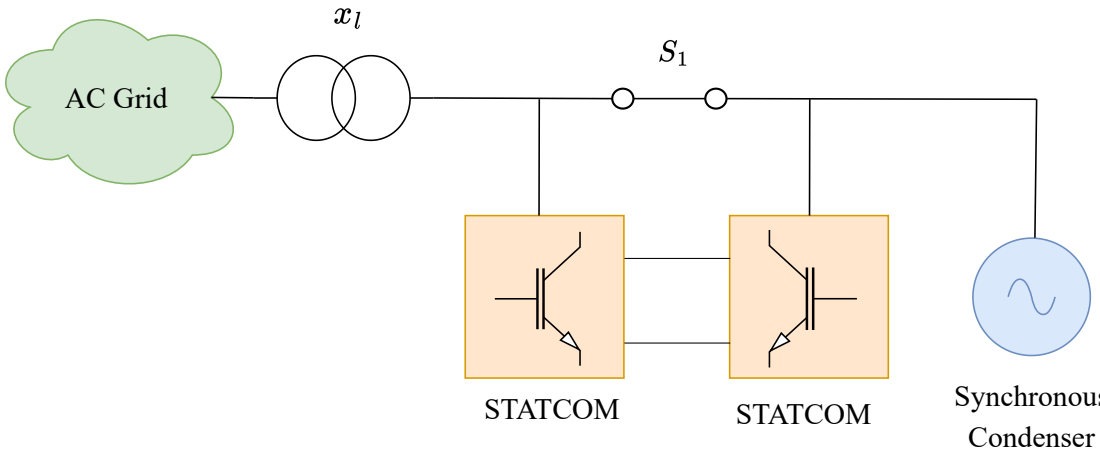

Figure 3.5: Steady-state equivalent circuit

Given these valuable features, incorporating the BtB-SC device into the LCC-HVDC system could effectively mitigate the operational challenges associated with connecting HVDC terminals to weak ac systems. This is because an SC of a much smaller rating and inertia can be used for this purpose to help mitigate voltage disturbances as well as frequency disturbances. This chapter extends the BtB-SC frequency topology application to enhance inverter-side ac voltage angle stability in LCC-HVDC systems connected to weak ac networks.

3.4 BtB-SC Configuration for Improving Transient Stability

To support system frequency and enhance ac voltage angle stability, the BtB-SC operates in the specific configuration depicted in Fig. 3.4. The reactive power setpoint for the SC-side converter is set to zero, and the active power reference is determined by a controller based

on the following equation:

$$P_{\text{ref}} = \underbrace{K_1 \cdot \Delta\omega}_{P_d} + \underbrace{K_2 \cdot \frac{d\Delta\omega}{dt}}_{P_i} \tag{3.8}$$

The parameter K_1 defines the frequency droop determining the active power component (P_d) injected into (or absorbed from) the ac system in response to the frequency variation ($\Delta\omega$). This valuable ancillary service is called Fast Frequency Support (FFS) [75]. The parameter K_2 determines the apparent inertia, as it controls the active power (P_i) supplied or absorbed by the SC in reaction to the rate of change of frequency ($\frac{d\Delta\omega}{dt}$) in the network. Using the controller depicted in Fig. 3.6, the BtB configuration enables substantial amounts of kinetic energy to be exchanged with the SC under precise control, without fear of losing synchronism.

When the system frequency deviates beyond ±0.5 Hz or the $RoCoF$ exceeds ±1 Hz/s during a disturbance (as determined by the first diamond block in Fig. 3.6 (a)), switch S_1 in Fig. 3.4 is opened and the selector switch labeled CTRL in Fig. 3.6 (b) is set to position 2. In this case, the SC delivers (or absorbs) active power to (or from) the ac grid based on the active power reference (P_{ref}) determined in block II of Fig. 3.6 (b). Additional control loops shown in block III of Fig. 3.6 (b) attempt to limit the synchronous machine speed (ω_{SC}) to within the predefined speed band ((ω_{SC-min}), (ω_{SC-max})). The performance of this configuration of BtB-SC for two different methods for selecting K_2, i.e., constant K_2 and dynamic K_2, as shown in Fig. 3.7, is now investigated.

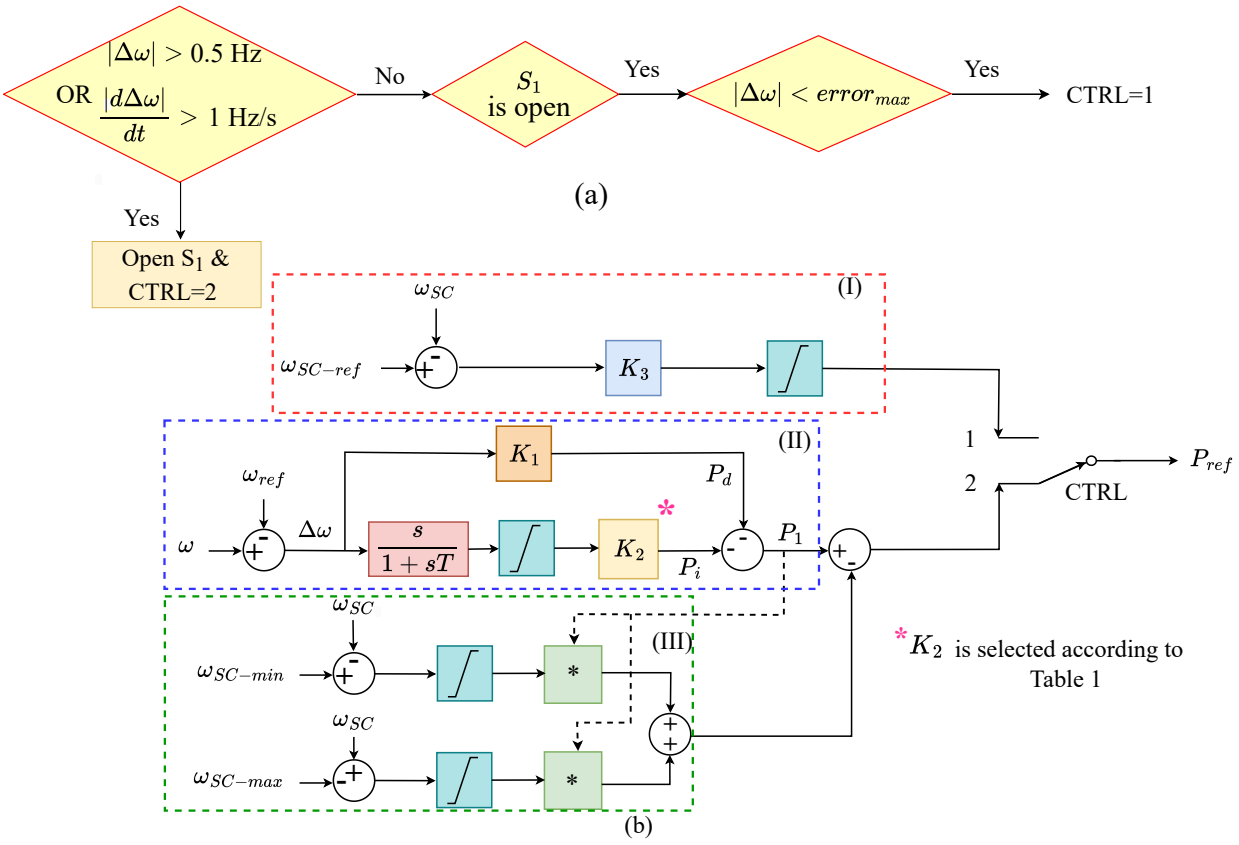

Figure 3.6: BtB-SC active power control block diagram

Constant K_2 selection mode

In this mode, K_2 remains constant. The BtB-SC behaves similarly to a stand-alone SC by absorbing or injecting active power proportional to the rate of change of frequency, as shown in Fig. 3.7 (b). Note that with a constant K_2, it can be seen from Fig. 3.7 (b) that P_i is negative when the ac frequency is rising towards 1.0 pu, i.e., active power is being taken away from the ac network and used to speed up the SC (hatched portion in Fig. 3.7 (b)). This has a negative impact on frequency restoration in the ac network. A solution to this, which can speed up the ac system frequency recovery, is to use a dynamic K_2.

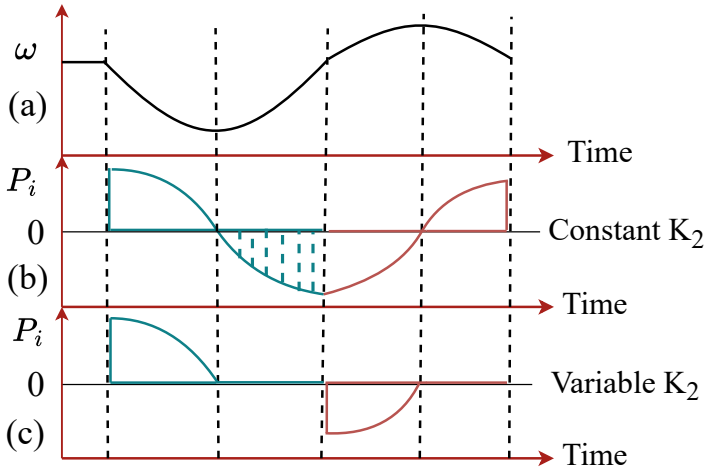

Figure 3.7: Selection of K_2: (a) ac frequency, (b) P_i: constant K_2 mode and (c) P_i: dynamic K_2 mode

Dynamic K_2 selection mode

Variable K_2 is determined based on the signs of the frequency deviation ($\Delta\omega = \omega\text{-}\omega_{ref}$) and the rate of change of frequency ($\frac{d\Delta\omega}{dt}$) following the logic presented in Table 3.2. The idea is to only exchange active power when the frequency is moving away from 1.0 pu and to have zero exchange when it is naturally moving towards 1.0 pu. This approach prevents the BtB-SC from impeding frequency restoration, unlike a standalone synchronous condenser, by setting the BtB active power order to zero during recovery intervals. Once the ac system frequency has recovered, the BtB-SC continues to exchange power with the ac system to restore the SC's rotational speed to its rated value. The rightmost control block in Fig. 3.6 (a) ensures that the power exchange with SC is only carried out when the ac frequency deviation $\Delta\omega$ is within a preset band ($error_{max}$) around the nominal frequency. Unlike a traditional SC, which would lose synchronism if its angle deviated too much, the proposed BtB-SC does not have this issue due to its asynchronous connection. As a result, the BtB-SC

Table 3.2: Selection criteria of K_2 value

$\Delta\omega = (\omega - \omega_{ref})$	$\frac{d\Delta\omega}{dt}$	Constant K_2	Variable K_2
> 0	> 0	design value	design value
≥ 0	≤ 0	design value	zero
< 0	< 0	design value	design value
≤ 0	≥ 0	design value	zero

exhibits a significantly higher apparent inertia constant H and damping D, positioning it as a key component in enhancing the frequency and, as a result, rotor angle stability of the ac system's generators.

3.5 Impact of BtB-SC on Frequency Stability of LCC-HVDC

This section investigates the performance of the BtB-SC under solid three-phase faults of varying durations applied to the inverter-side ac bus. Fig. 3.8 shows a weak LCC-HVDC transmission system developed on an EMT simulation program.

The base LCC system is the CIGRÉ Benchmark model [75], operating at half of its rated capacity with an active power of 500 MW. Consequently, the ac filter banks operated at half capacity, supplying 312 MVAr of reactive power. The ac-side Thevenin equivalent in the published benchmark has been replaced with the host ac system consisting of two ac hydro generators (to incite inter-machine mechanical oscillation modes), local loads, and the proposed BtB-SC apparatus. The effective short-circuit ratio (ESCR) in the base system is 1.5 at the inverter and 4.0 at the rectifier end. In parametric studies, the base case ESCR can be changeable. The inverter-side ac system includes the ac filters, the proposed BtB-SC

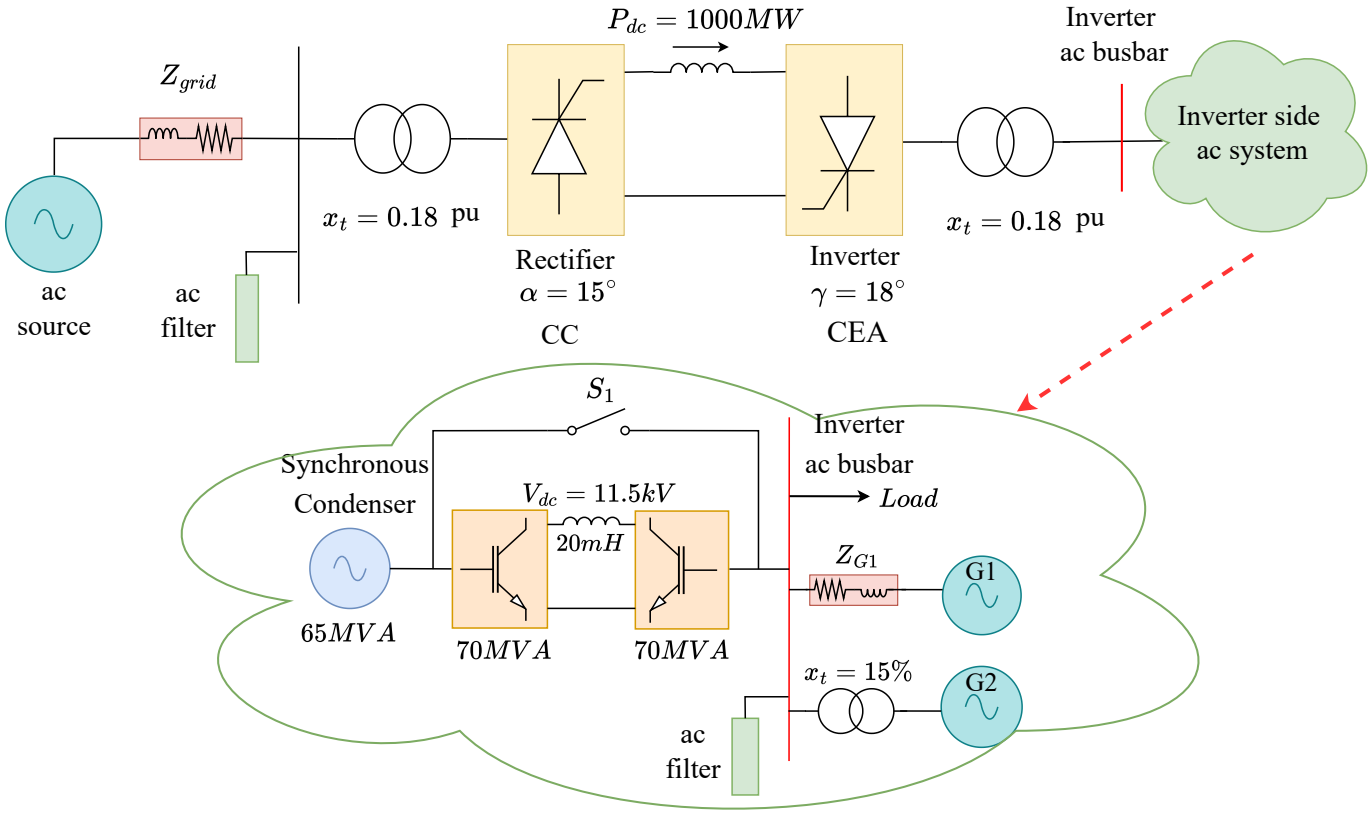

Figure 3.8: LCC-HVDC System configuration

device, and two synchronous generators with unequal inertia constants and power ratings as shown in Fig. 3.8. G_1 is a 500 MVA remote generator connected by a 100 km long 230 kV line represnted by Z_{G_1}. G_2 is a 500 MVA generator located at the HVDC inverter. The local load at the inverter ac busbar is $(1200 + j360)$ MVA, consisting of 50% constant power and 50% constant impedance loads. The system parameters are given in Table 3.3. According to the sub-transient reactance for generators given in Table 3.4, the short-circuit level for the

Table 3.3: LCC-HVDC System Parameters

Parameters	**Rectifier**	**Inverter**
ac side base voltage	345 kV	230 kV
Base MVA	1000 MVA	1000 MVA
Rated dc voltage	500 kV	500 kV
Rated dc current	2 kA	2 kA
Transformer voltages (kV)	345:211.42	211.42:230
Controller gains (K_p, K_i)	$(1.10, 0.01)$	$(0.5, 0.5)$
shunt filter rating (MVAr)	625	625

ac system is calculated as follows:

$$SCL_{G_1} = \frac{1}{jx"_d * \frac{MVA_{base}}{MVA1_{rated}} + Z_{G_1} * \frac{MVA_{base}}{MVA1_{rated}}} = \frac{1}{j0.25 * \frac{1000}{500} + (0.1 + j0.5) * \frac{1000}{500}} = 0.67 \text{ pu} \tag{3.9}$$

$$SCL_{G_2} = \frac{1}{jx"_d * \frac{MVA_{base}}{MVA2_{rated}} + x_t * \frac{MVA_{base}}{MVA2_{rated}}} = \frac{1}{j0.25 * \frac{1000}{500} + j0.15 * \frac{1000}{500}} = 1.25 \text{ pu} \tag{3.10}$$

Therefore, the total short-circuit level of the ac system is:

$$SCL_{total} = SCL_{G_1} + SCL_{G_2} = 1.92 \text{ pu} \tag{3.11}$$

The ESCR of our ac system can be calculated as follows:

$$ESCR = SCL_{total} - \frac{Q_{filter}}{P_{dc}} = 1.92 - \frac{312}{500} = 1.3 \text{ pu} \tag{3.12}$$

There is a quantitative relationship between the power stability of the HVDC system and the ESCR. Generally, a critical effective short-circuit ratio (CESCR) of around 1.5 is

recommended [11,53] when operating under typical converter station equipment parameters. If the ESCR falls below 1.5, the LCC-HVDC system will have difficulty in maintaining stable operation. Since the ESCR of the base system (1.3) is below the critical ESCR threshold of 1.5, a synchronous condenser is deployed to elevate the ESCR to 1.5. The SC should increase the ESCR by 0.2 (i.e., 1.5-1.3). The required rating of SC is calculated as follows:

$$SCL_{SC} = \frac{1}{jx"_d * \frac{MVA_{base}}{MVA_{SC}} + x_t * \frac{MVA_{base}}{MVA_{SC}}} = \frac{1}{j0.22 * \frac{1000}{MVA_{SC}} + j0.1 * \frac{1000}{MVA_{SC}}} \rightarrow MVA_{SC} = 64 \text{ MVA} \tag{3.13}$$

According to 3.13, the SC incorporated into the BtB-SC device is sized at 65 MVA and equipped with a static exciter since it has the potential to offer a faster response, which is essential in a very weak LCC-HVDC system. The time constants with brushless or other types of exciters are much slower and typically less suitable for applications demanding fast voltage support. The VSCs are half-bridge modular multilevel converters (MMC), with 11 submodules per arm and a 1 mH reactor connected in series with each arm. The machine parameters are listed in Table 3.4.

Table 3.4: Synchronous machines and SC parameters

	x''_d (pu)	x_d (pu)	H (s)	Exciter gains (K_p, K_i)
G_1	0.25	1	2	(20,0.05)
G_2	0.25	1.5	2.5	(25,0.01)
SC	0.22	0.92	5	(200,0.02)

As discussed earlier, during a frequency event in the electrical grid, switch S_1 is opened to allow the BtB-SC to deliver substantially more active power to the system. The timing of this topology transition is critical. While S_1 remains closed, the two STATCOM units together with the synchronous condenser are collectively providing substantial reactive power support

to the system. However, once S_1 is opened, only the grid-side VSC continues operating in voltage control mode, reducing reactive power support to approximately one-third of the original level.

During ac faults, rapid reactive power injection is essential to restore system voltage promptly to prevent grid voltage collapse or commutation failure in the LCC inverter systems. However, during the subsequent recovery phase, the system typically experiences transient overvoltage before settling at the rated value. To ensure system stability and equipment protection, this overvoltage must be limited to a maximum threshold of 1.05 pu. Simultaneously, such faults induce a generation-load imbalance, causing frequency deviations. Therefore, the BtB-SC must deliver active power swiftly enough to prevent the system frequency nadir from dropping below the minimum permissible level. Consequently, S_1 should remain closed just long enough to provide sufficient reactive power for voltage recovery after fault clearance, and yet not be too long to precipitate a large $RoCoF$. The timing can be adjusted by conducting simulation studies. To demonstrate this, a remote ac fault causing the voltage at the inverter ac bus to drop to 0.4 pu is applied for 100 ms, and the voltage recovery is examined for varying durations of the topology transition. Fig. 3.9 illustrates voltage regulation for topology transitions occurring 100, 150, 200, and 250 ms after fault clearance.

The curves in Fig 3.9 illustrate that while a 100 ms delay provides sufficient initial voltage support, allowing the voltage to recover from 0.4 pu to 1.0 pu, it results in a transient overshoot exceeding the 1.05 pu threshold (blue curve). Since this violation is impermissible, the duration for which the bypass switch S_1 remains closed was extended to 150 ms. As indicated by the orange curve, while the peak overvoltage is reduced, it remains above the allowable limit. A further increase in the closing time to 200 ms (green curve) brings the

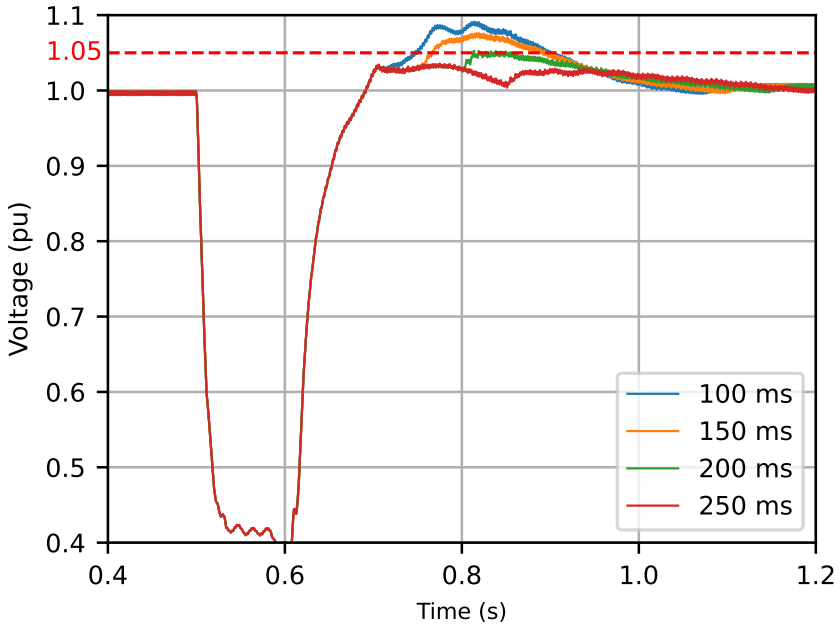

Figure 3.9: Voltage recovery for circuit breaker opening times of 100, 150, 200 and 250 ms

peak voltage exactly to the 1.05 pu boundary without violating it. Finally, extending the delay to 250 ms (red curve) maintains the maximum voltage at 1.03 pu, ensuring the entire recovery profile remains within the acceptable range. These results demonstrate that the delay to open the circuit breaker is maintained in the range 200-250 ms, resulting in a well-damped and maintained voltage within acceptable limits. Further increasing the closure time yields no additional benefit in our case, as the voltage had already substantially recovered by 250 ms post-fault.

On the other hand, longer closure durations of S_1 delays the activation of inertia support from the BtB-SC to the system resulting in greater initial frequency deviation, a lower frequency nadir, and extended time to reach steady state, as illustrated in Fig. 3.10.

The timing of this topology transition can be adapted based on specific system prior-

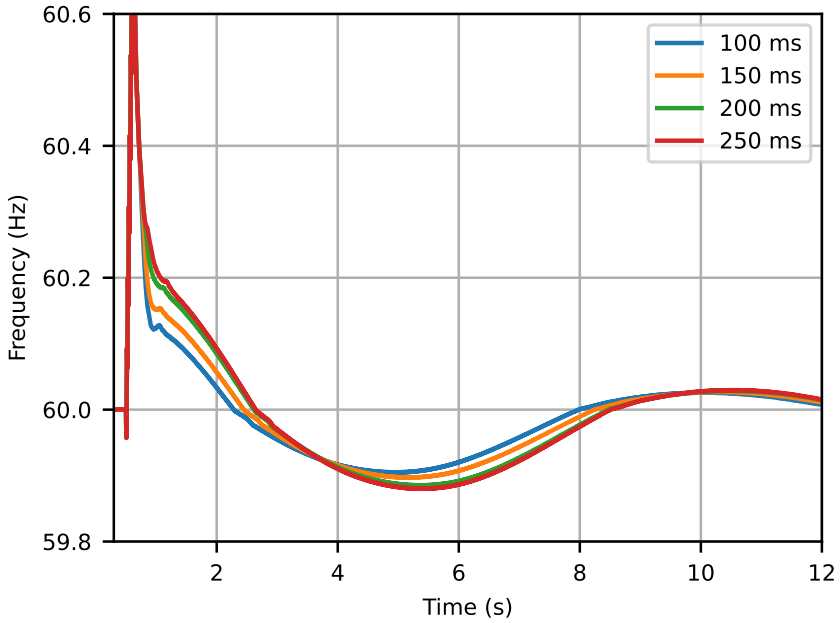

Figure 3.10: Frequency recovery for circuit breaker opening times of 100, 150, 200, and 250 ms

ities and the nature of the contingency specifically whether the voltage excursion or the frequency deviation exhibits greater transient severity. By adjusting the switching interval, the control scheme can be tailored to prioritize the most critical stability requirement for a given disturbance. If the grid requirements prioritize active power (frequency regulation), an earlier transition is more effective for mitigating frequency excursions. Conversely, for systems where reactive power (voltage regulation) is the priority, maintaining S_1 in the closed position for an extended duration is more appropriate to enhance the voltage recovery.

To evaluate the impact of the back-to-back synchronous condenser (BtB-SC) on the angle stability of the inverter-side ac voltage in a weak LCC-HVDC system during a frequency event, a solid three-phase ac fault is applied at t=0.5 s with varying fault durations.

Constant K_2 selection mode

This section investigates the performance of BtB-SC with K_2 as a constant. Here, the power order of the BtB-SC is calculated based on (3.8) with K_1 set to zero and K_2 calibrated to 70 pu/pu. Therefore, the hybrid system operates solely as a pure inertia source, supplying power only during frequency transients. Therefore, the apparent inertia of the BtB-SC in this case study can be calculated using the swing equation, assuming the damping coefficient of the SC is negligible, as follows:

$$\left.\begin{aligned} 2H\tfrac{d\Delta\omega}{dt} &= -\Delta P \\ K_2\tfrac{d\Delta\omega}{dt} &= -P_{\text{ref}} \end{aligned}\right\} \implies H_{BtB} = \frac{K_2}{2} \tag{3.14}$$

According to (3.14), the BtB-SC provides an apparent inertia of 35 s which is seven times larger than that of the standalone SC. The equivalent inertia of the ac system, considering the contribution of two generators G_1, and G_2 can be expressed as:

$$H = \frac{H_1\text{MVA}_1 + H_2\text{MVA}_2}{\text{MVA}_1 + \text{MVA}_2} = 2.25 \text{ s} \tag{3.15}$$

If an SC with the same rating as that used in the BtB-SC is connected directly to the system, the apparent inertia increases to 2.72 s as per (3.15). However, if the SC is interfaced with the BtB converters, the apparent inertia increases significantly by almost 90% to 4.25 s.

Fig. 3.11 shows the response of frequency and ac voltage angles following faults of various durations. In the absence of the BtB-SC, the LCC-HVDC system experiences escalating oscillations in the inverter ac voltage angle and frequency, failing to recover in case of fault durations of 100 ms. However, with the BtB-SC, the system can successfully recover and maintain synchronism for much larger fault durations, e.g., 200 ms.

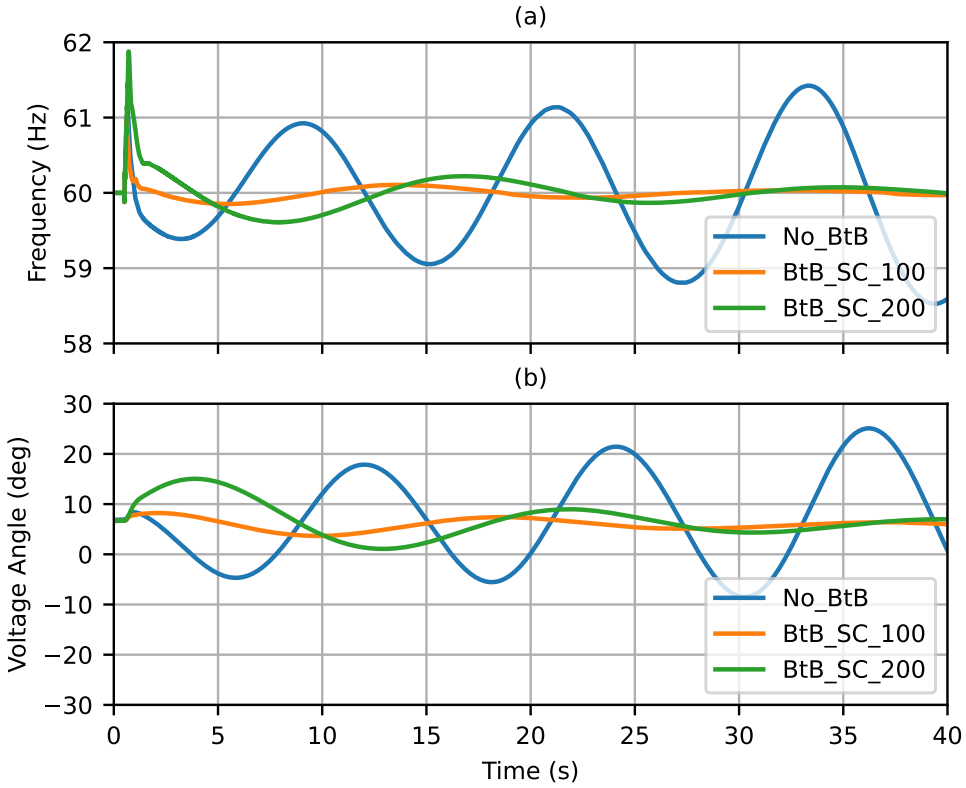

Figure 3.11: Impact of BtB-SC with $K_2 = 70$, constant control mode, fault duration of 100 ms and 200 ms

Fig. 3.12 (a) illustrates the reference value for the direct-axis (d-axis) current of the machine-side converter. This current is derived from the active power reference generated by the BtB-SC control scheme shown in Fig. 3.6. Consequently, as shown in Fig. 3.12(b), the BtB-SC exchanges a significant amount of active power with the grid to facilitate frequency regulation. Furthermore, Fig. 3.12 (c) illustrates that the speed of the synchronous condenser in the BtB-SC configuration exhibits significant deviation without being constrained by the requirement to maintain synchronism with the grid.

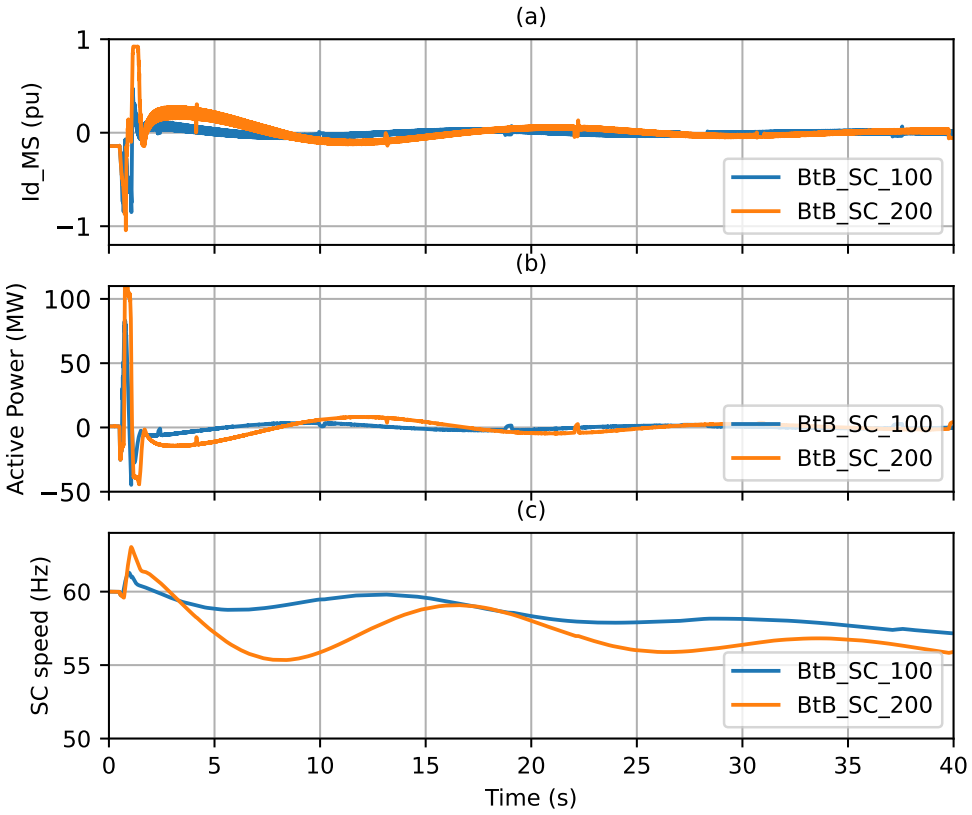

Figure 3.12: Direct-axis current (a) synchronous condenser active power (b) and speed (c) in constant control with $K_2 = 70$, during 100 ms & 200 ms faults

As discussed earlier, breaker S_1 is kept closed for a few cycles following fault clearance to accelerate voltage recovery and mitigate post-fault over-voltage. Fig. 3.13 (a) shows that the system with the BtB-SC exhibits satisfactory recovery of voltage, with recovery from 0 to 1 pu in 90 ms as opposed to 140 ms without the BtB-SC with a significantly reduced over-voltage profile (peak of 1.05 pu instead of 1.19 pu), enabled by substantial reactive power exchange with the network, as illustrated in Fig. 3.13 (b). Immediately following fault clearance, Fig. 3.13 (c) demonstrates that the reactive current (I_q) injected by the BtB-SC reaches its upper limit. This provides the system with maximum reactive power to

restore the ac voltage to its rated value as rapidly as possible. Once the voltage reaches 1.0 pu, the BtB-SC transitions to reactive power absorption to suppress the transient overvoltage and maintain it below the 1.05 pu threshold. At point A on the graph, the bypass switch S_1 opens to initiate frequency recovery; consequently, the reactive power absorbed by the BtB-SC decreases, resulting in a slight increase in the bus voltage.

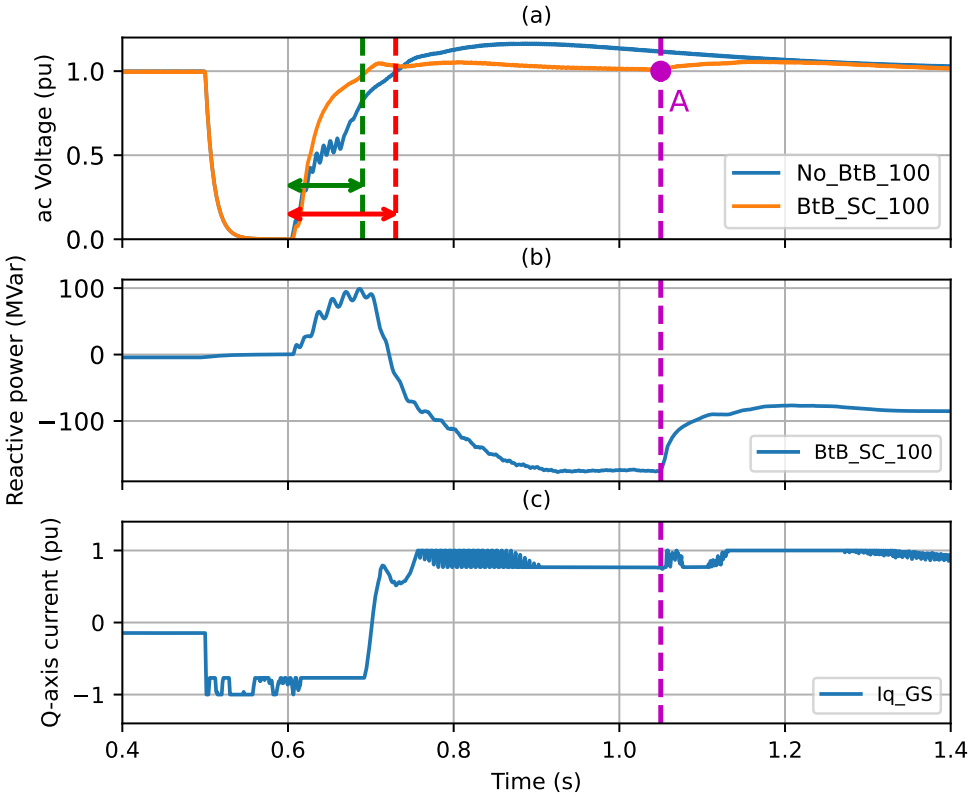

Figure 3.13: Post-fault voltage recovery with and without BtB-SC: (a) voltage restoration (b) reactive power, and (c) q-axis current with $K_2 = 70$, during 100 ms faults

Fig. 3.14 (a) shows that without the BtB-SC, the voltage exhibits growing oscillations following a 100 ms fault. In contrast, with the BtB-SC integrated, the voltage returns rapidly to steady state for a 100 ms fault and is also able to suppress such oscillations even for a

larger duration of faults, such as 200 ms. Fig. 3.14 (b) shows the quadrature-axis current of the grid-side converter operating in voltage control mode throughout the study to regulate the grid ac voltage.

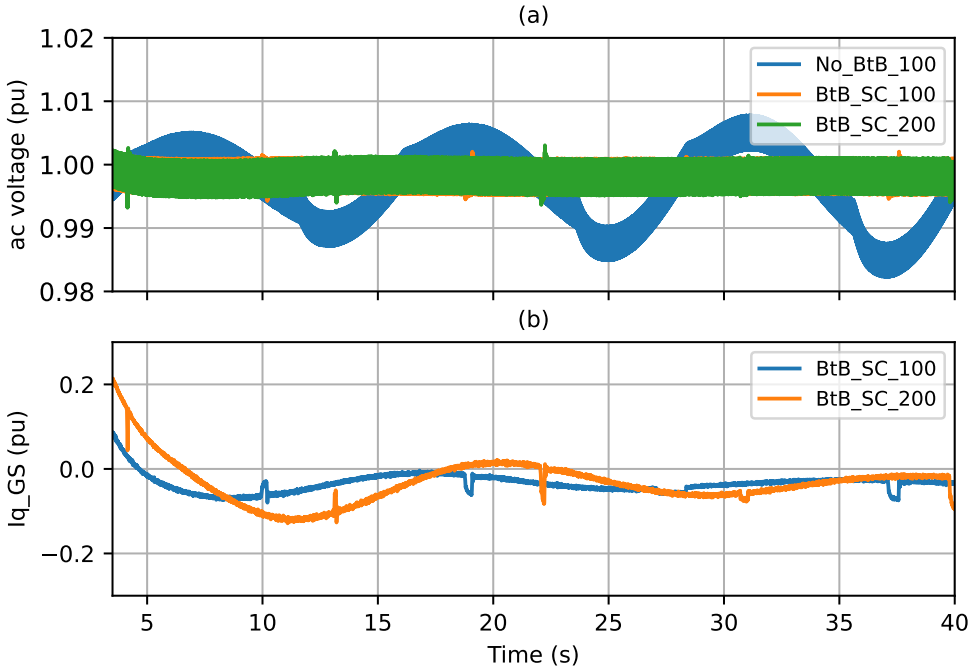

Figure 3.14: Post-fault voltage regulation with and without BtB-SC: (a) voltage restoration and (b) Grid-side converter q-axis current with $K_2 = 70$, during 100 ms, and 200 ms faults

Fig. 3.15 (a) and (b) show the ac and dc voltages of the VSCs, respectively, during BtB-SC operation.

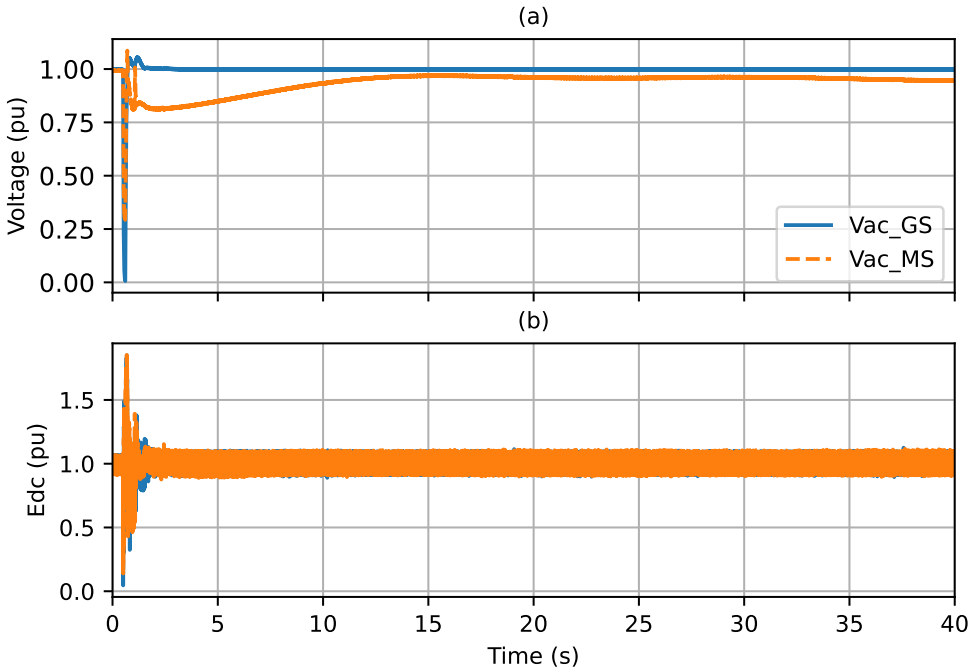

Figure 3.15: VSC's ac and dc voltages during BtB-SC operation, with (a) ac voltages and (b) dc voltages

Dynamic Selection of K_2

This section evaluates the performance of the BtB-SC if K_2 is allowed to change dynamically during a transient. Specifically, solid three-phase ac faults with durations ranging from 100 ms to 200 ms are investigated. As mentioned in section 3.4, the recovery can be enhanced if the BtB-SC injects power only when the system is straying in frequency from 1.0 pu, and injects zero power in periods where the frequency is naturally moving towards 1.0 on its own, according to Fig. 3.16. For instance, during the interval from 6 s to 8.7 s for a 200 ms fault duration, the I_d of the machine-side (MS) converter and, as a result, the active power injection is reduced to zero and the SC speed remains constant. Fig. 3.16(a) shows that, with the BtB-SC under dynamic K_2 selection, the system frequency recovers

satisfactorily following fault durations of 100 ms and 200 ms. Fig. 3.16(b) presents the direct-axis current of the machine-side converter operating in active power control mode to regulate the grid frequency. Fig. 3.16(c) illustrates the active power delivered by the BtB-SC, while Fig. 3.16(d) shows the post-fault speed response of the synchronous condenser for different fault durations.

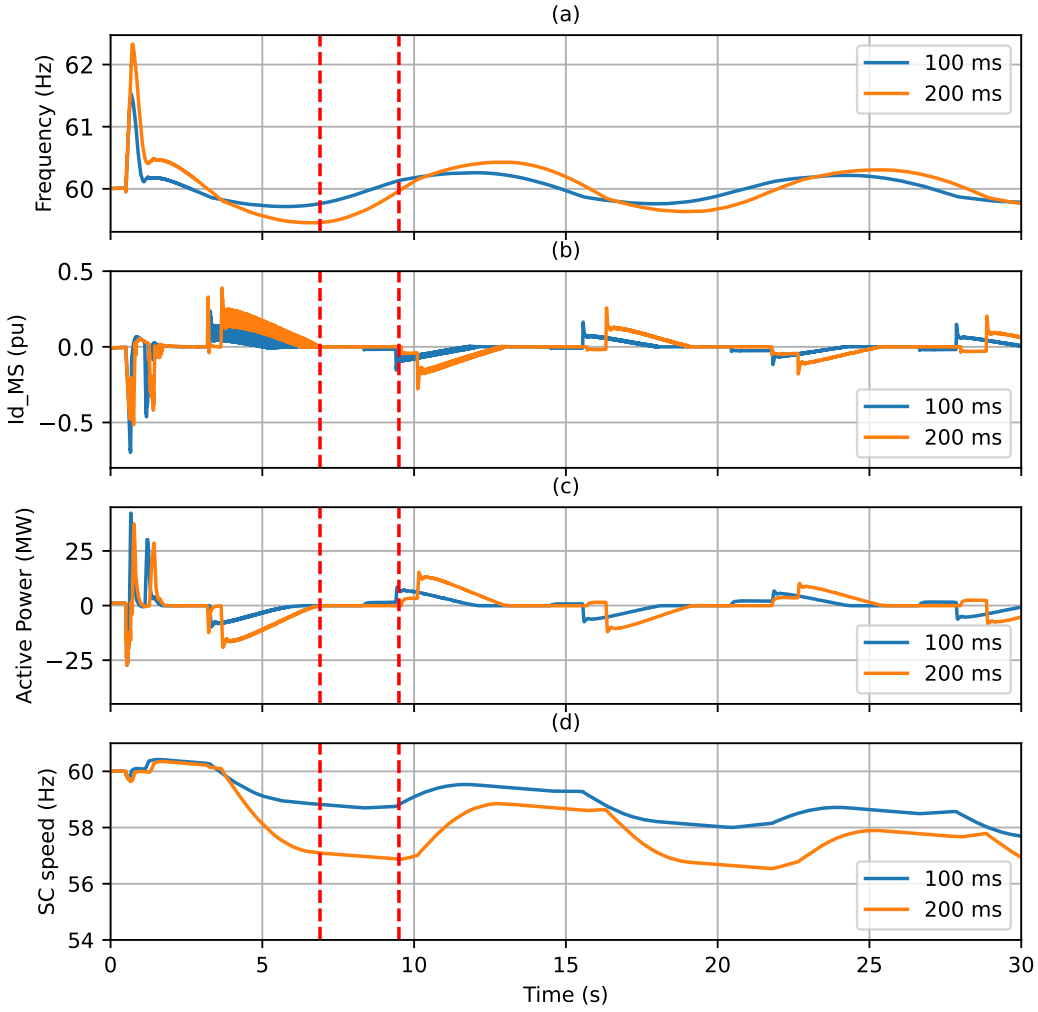

Figure 3.16: System Frequency (a) Direct-axis current of Machine-side (MS) converter (b) SC active power (c) and SC speed (d) under dynamic selection mode with $K_2 = 70$, during 100 ms & 200 ms faults

As expected and shown in Fig. 3.17, the recovery with dynamic K_2 is significantly faster, i.e., recovery to 59.9 Hz (0.998 pu) takes 8.3 s with dynamic K_2, as opposed to 12.1 s with constant K_2.

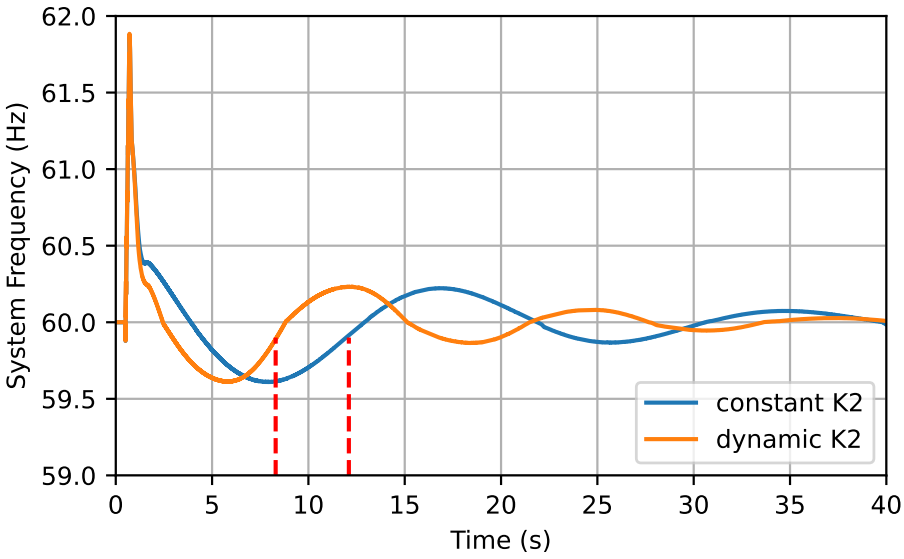

Figure 3.17: Comparison of BtB-SC with dynamic and constant K_2 control for fault duration of 200 ms

In addition to providing inertia support, the controller parameter K_1 enables the BtB-SC to enhance damping of electromechanical modes, as indicated in equation 3.8. In this case, K_1 is set to 20 pu/pu, allowing the hybrid system to inject 1 pu of active power in response to a frequency deviation of 0.05 pu.

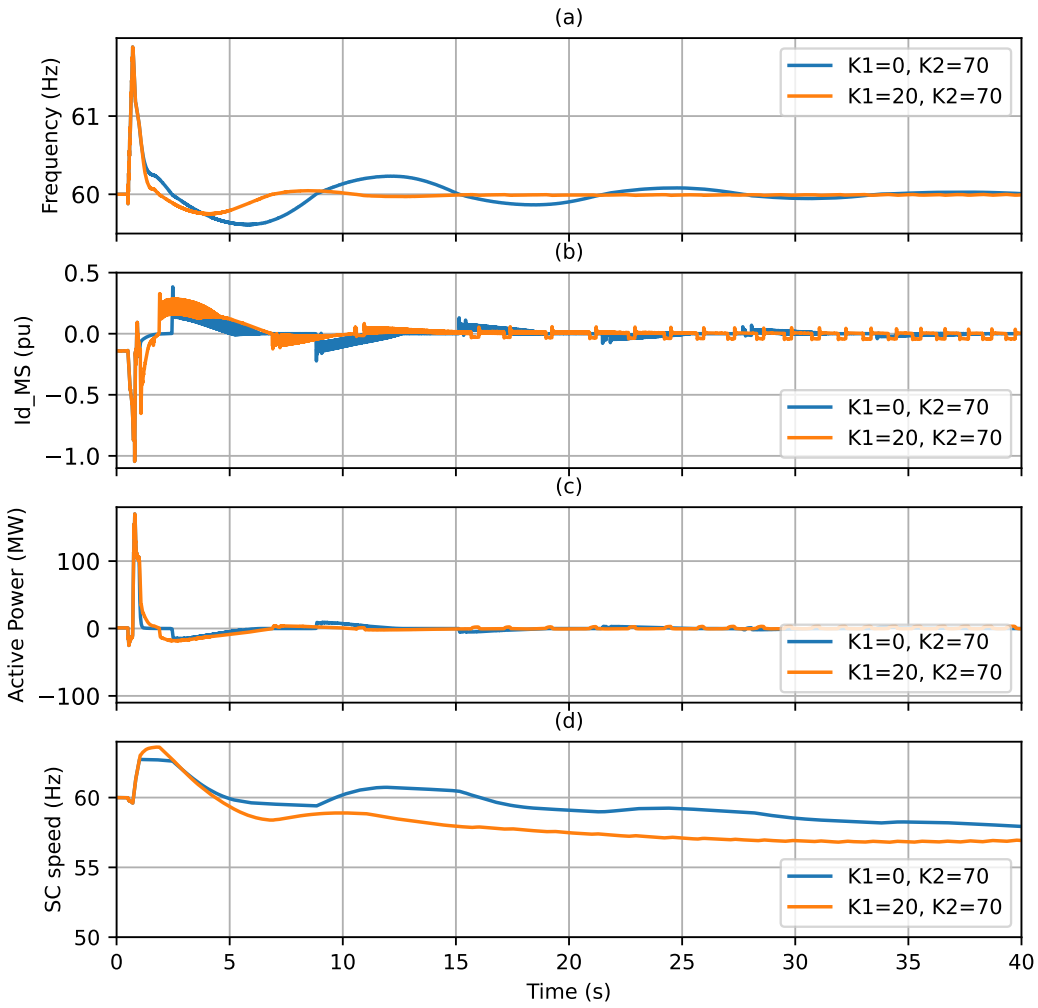

Figure 3.18: Comparison of BtB-SC with $K_1 = 0$ & $K_1 = 20$ in dynamic control mode for fault duration of 200 ms

Fig. 3.18 presents the corresponding system frequency, machine-side converter I_d, provided active power, and SC speed for $K_1 = 20$ and $K_2 = 70$. As shown in Fig. 3.18(a), the presence of the BtB-SC leads to a significantly more damped frequency response.

3.6 A Comment on Economic Considerations of the Proposed Scheme

As previously discussed, the BtB-SC offers significantly enhanced frequency support to the ac grid compared to a conventionally connected synchronous condenser. By utilizing a lower-rated SC in conjunction with two STATCOMs, the BtB-SC can provide a level of emulated inertia equivalent to that of a much larger standalone unit. Furthermore, this hybrid configuration facilitates much faster reactive power injection for voltage regulation than a traditional high-rating SC. From an economic perspective, the comparison reveals a distinct trade-off: while the initial Capital Expenditure (CAPEX) for a STATCOM is higher due to the advanced power electronics (IGBTs) required, the Operating Expenditure (OPEX) is notably lower. Specifically, traditional SCs incur higher maintenance costs due to mechanical rotating parts, lubrication requirements, and cooling systems. Moreover, the static operation of a STATCOM results in lower energy losses compared to the friction and windage losses inherent in a standalone SC. While a comprehensive economic analysis from a commercial standpoint would be highly valuable, such an evaluation is beyond the scope of this thesis, which focuses strictly on the technical performance and stability impacts of the system.

3.7 Summary

This chapter addresses the stability challenges of LCC-HVDC systems connected to weak ac grids. It explains the role of reactive compensators, such as synchronous condensers and STATCOM, in mitigating these issues. It then presents a novel topology where a synchronous

condenser connects to the ac bus of a weak LCC-HVDC system through a back-to-back voltage source converter link. It also designs the control system for the BtB-SC that gives superior performance during frequency events.

Results demonstrate that this configuration substantially improves the system's transient stability margin and rotor angle stability during severe disturbances, including long-duration three-phase-to-ground faults. Post-disturbance, the synchronous link between the SC and grid is deliberately disconnected, enabling asynchronous SC operation. This decoupling permits greater speed deviations and larger energy exchanges between the SC and ac network, yielding higher apparent inertia, reduced frequency deviations, and enhanced resistance to rotor angle instability.

Chapter 4

Enhancing Inertia and Voltage Regulation Using the BtB-SC at LCC-HVDC Terminals

This chapter evaluates the application of BtB-SC topology in addressing stability challenges in LCC-HVDC systems connected to weak ac networks, with a specific focus on N-1 contingencies that simultaneously stress both grid frequency and voltage. The previous chapter examined the advantages of the BtB-SC in recovering from disturbances such as ac faults, compared with scenarios where the BtB-SC is absent. In this chapter, I investigate how recovery from events such as generator trips is influenced by the BtB-SC topology. It compares the performance of this configuration against a traditional synchronous condenser of equivalent rating. System performance is validated through detailed electromagnetic transient (EMT) simulations performed in PSCAD/EMTDC.

4.1 Performance Comparison of BtB-SC and Standalone SC

To evaluate the performance of various reactive power compensators, the baseline weak LCC-HVDC system shown in Fig. 3.8 serves as the study case. The LCC system operates at its rated capacity with an active power of 1000 MW. Consequently, the ac filter banks are dispatched at full capacity, supplying 625 MVAr of reactive power. G_1 is a 1000 MVA generator with an inertia constant of 5 s in this study, whereas all other system parameters remain identical to those in Table 3.3 and Table 3.4.

4.1.1 Voltage Regulation Due to an ac Fault

As mentioned in section 1.1, a "frequency event" is defined as a contingency, such as a load rejection or generator trip, that induces a change in system frequency. Similarly, a "voltage event" refers to a disturbance, like an ac fault, that results in a significant voltage deviation.

The normal operation configuration of the BtB-SC device is shown in Fig. 3.5. To compare the performance of the BtB-SC system with that of a standalone SC during a voltage disturbance, a remote three-phase to ground fault lasting 200 ms is applied at the inverter ac bus at $t = 1$ s. Two scenarios are investigated. In the first, the VSC converters are blocked, allowing only a standalone SC to operate. In the second, the BtB converters are configured as two STATCOMs in parallel with the SC and regulate the ac voltage.

Fig. 4.1 presents a comparison of the voltage regulation responses for two scenarios under the same event. It clearly shows that with the BtB-SC system, the ac voltage recovers to within 10% of its rated value within 130 ms. However, with the standalone SC, the same recovery is much slower, taking 300 ms. Fig. 4.2 demonstrates that the reactive power

injected by the BtB-SC configuration (Fig 4.2 (b)) is nearly three times greater than that of the standalone SC (Fig 4.2 (a)).

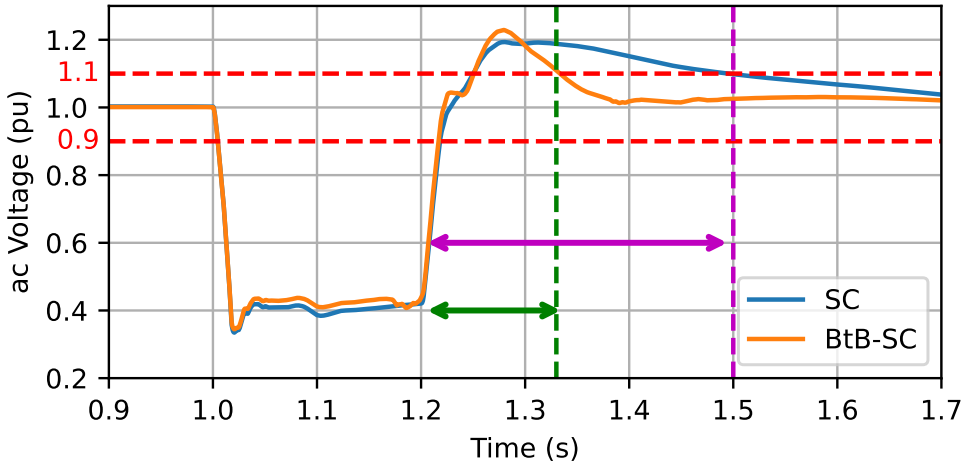

Figure 4.1: Comparison of voltage dynamic response between the standalone SC and the BtB-SC

Due to the rapid response of the back-to-back VSCs and the additional reactive power (MVAr) support they offer relative to a standalone SC, the BtB-SC configuration significantly facilitates post-fault voltage recovery.

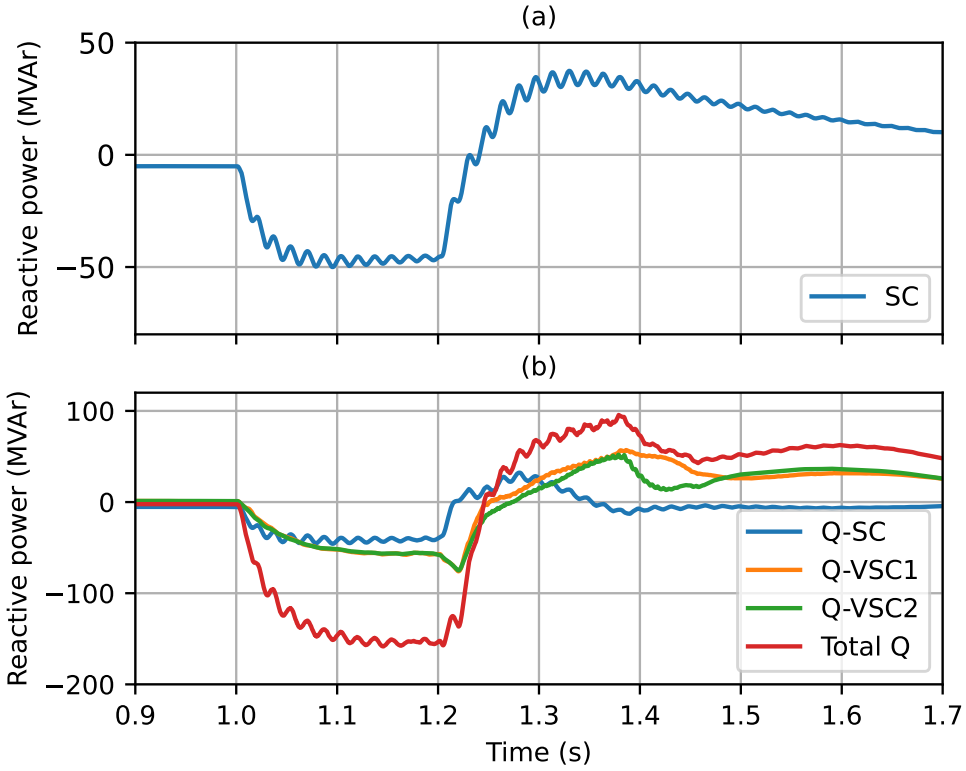

Figure 4.2: Comparison of reactive power contribution between the standalone SC and the BtB-SC

4.1.2 Comparison of a Stand-alone SC and BtB-SC due to a Frequency Event

The relative inertia contributions of a standalone SC and the proposed BtB-SC system are now compared. In this scenario, generator G_1 (1000 MVA) with an inertia constant $H = 5$ s is tripped at $t = 1$ s.

To ensure a realistic assessment of the BtB-SC, operational latencies were incorporated based on the input step change test requirements defined in IEEE Std C37.118.1a-2014

(Table 10) [76]. The maximum allowable response time for $RoCoF$ is specified as $\frac{6}{f_0}$ seconds, where f_0 denotes the nominal frequency. For the 60 Hz system under study, this yields a measurement latency of 100 ms. By accounting for an additional 20 ms for the mechanical action time of circuit breaker S_1, the total latency for the BtB-SC to initiate active power exchange is established at 120 ms.

The controller (the leftmost diamond block in Fig. 3.6 (a)) identifies a frequency event and opens S_1 if the system frequency deviation exceeds 0.5 Hz (0.008 pu) or the rate of change of frequency surpasses 1 Hz/s. Depending on the applicable grid codes, these thresholds can be modified based on the requirements of the specific system. By opening the switch S_1, the BtB-SC can provide a significant short-term increase in effective inertia, as the stored kinetic energy in the rotor can be tapped for short-time intervals. This is possible only because the SC connects asynchronously to the ac grid, as shown in Fig. 3.4, and does not need to be synchronized with the grid's frequency. In this case, the SC delivers (or absorbs) active power to (or from) the ac grid based on the active power reference P_{ref} determined in Block II of Fig. 3.6 (b), as given in (3.8). The factor K_2 in (3.8), which controls the apparent inertia is selected according to Table 3.2. Power transfer continues until the system frequency begins to recover or the SC's rotational speed reaches its permissible minimum or maximum limit, enabling the BtB-SC to manifest a considerably higher apparent inertia constant H compared to a conventional SC, significantly enhancing its role in promoting frequency stability within the ac grid [70].

Inertia Contribution of Proposed BtB-SC Arrangement

To study the inertia contribution of the proposed BtB-SC scheme, it is also compared with the standalone SC. Here, the power order of the BtB-SC is calculated based on (3.8) with a

nonzero value for K_2 and K_1 (which controls damping) set to zero. Hence, the hybrid system operates solely as a pure inertia source, supplying power only during frequency transients. The value of K_2 is calibrated to 60 pu/pu, ensuring the system delivers 1 pu (65 MW) of active power for a $\frac{d\Delta\omega}{dt} = 1$ Hz/s (0.016 pu/s).

According to (3.14), the BtB-SC provides an apparent inertia of 30 s, which is six times larger than that of the standalone SC. The equivalent inertia of the ac system, following the tripping of G_1, considering the contribution of the remaining generator G_2 with a standalone SC, can be derived as was done in (3.15) for the two-generator case.

$$H = \frac{H_2\text{MVA}_2 + H_{\text{SC}}\text{MVA}_{\text{SC}}}{\text{MVA}_2 + \text{MVA}_{\text{SC}}} = 2.79 \text{ s} \tag{4.1}$$

As indicated by (4.1), adding a stand-alone SC increases the system's equivalent inertia to 2.79 s—representing a 12% uplift relative to the system without a compensator.

Incorporating the BtB-SC, the power setpoint is determined according to (3.8), with K_1 set to zero and K_2 adjusted to 60 pu/pu. As a result, the hybrid system delivers active power only during frequency disturbance, resulting in an equivalent inertia for the system given by:

$$H_{eq-BtB-SC} = \frac{H_2\text{MVA}_2 + H_{\text{BtB-SC}}\text{MVA}_{\text{BtB-SC}}}{\text{MVA}_2 + \text{MVA}_{\text{BtB-SC}}} = 5.66 \text{ s} \tag{4.2}$$

Note that integrating the BtB-SC temporarily boosts the equivalent inertia to 5.66 s, which is over double the inertia achieved with the stand-alone SC. This higher apparent inertia reduces the $RoCoF$, allowing more time for primary control to adjust the power output. The $RoCoF$, which depends on the size of the power imbalance and the system inertia, is

given by:

$$RoCoF = \frac{f_0}{2H_{sys}} \frac{\Delta P}{S_{sys}} \tag{4.3}$$

where ΔP represents the disturbance magnitude and f_0 denotes the nominal system frequency. Note that the $RoCoF$ is inversely proportional to the inertia constant H. Let H_1 and $RoCoF_1$ be the inertia constant and rate of change of frequency of System 1, and H_2 and $RoCoF_2$ correspond to those of System 2, respectively. Consequently, the ratio of $RoCoF$ values of these two systems for a given disturbance can be expressed based on 4.3 as follows:

$$\left.\begin{aligned} RoCoF_1 &= \tfrac{f_0}{2H_1} \tfrac{\Delta P}{S_{sys}} \\ RoCoF_2 &= \tfrac{f_0}{2H_2} \tfrac{\Delta P}{S_{sys}} \end{aligned}\right\} \implies RoCoF_2 = RoCoF_1 \frac{H_1}{H_2} \tag{4.4}$$

Fig. 4.3 (a) illustrates that, due to the larger apparent inertia of the BtB-SC, the system achieves a substantially lower $RoCoF$ of 0.8 Hz/s, compared to 1.62 Hz/s for the system with a stand-alone synchronous condenser. The apparent inertia values are 5.66 s for the system with the BtB-SC and 2.79 s with a conventional SC, hence the $RoCoF$ changes in the ratio of $2.79/5.66 = 0.49$. As a result of the BtB-SC's lower $RoCoF$, the frequency nadir improves to 58.1 Hz, higher than the 57.25 Hz observed for the SC.

As mentioned before, the BtB-SC's ability to operate asynchronously with the ac grid allows energy to be transferred to or from the ac network by tapping the stored energy in the SC's rotor. Figs. 4.3 (b) and (c) illustrate that in the BtB-SC configuration, the synchronous condenser delivers substantially higher active power to the system than the stand-alone SC, which must operate with the constraint of maintaining synchronism with the grid.

As mentioned in section 3.4, the BtB-SC has the opportunity to dynamically change the

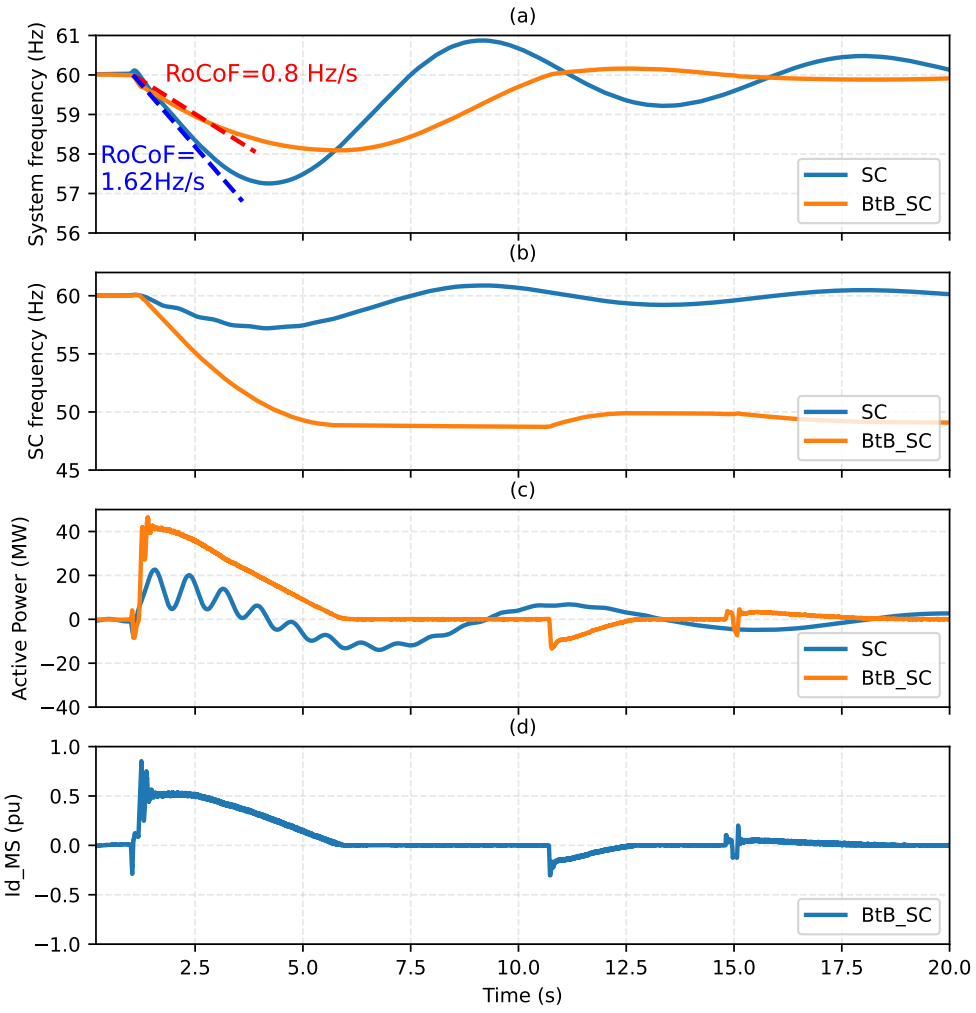

Figure 4.3: Frequency regulation for LCC-HVDC system using stand-alone SC and BtB-SC with $K_1 = 0$ during a frequency event

apparent inertia even during a power swing. Thus, as the system frequency gradually converges towards its steady-state value, the BtB-SC controller reduces K_2 to zero, as specified in 3.2. This action effectively ceases active power injection, as evident in Fig. 4.3 (c) during the interval from 5.7 to 10.6 seconds. This transition allows the BtB-SC to provide robust frequency support during transients while smoothly returning to a minimal power mode

once system stability is re-established, demonstrating its dynamic adaptability in maintaining grid stability. Fig. 4.3 (d) shows the direct-axis current commanded by the machine-side converter controller to supply the system with the reference active power determined by the BtB-SC controller.

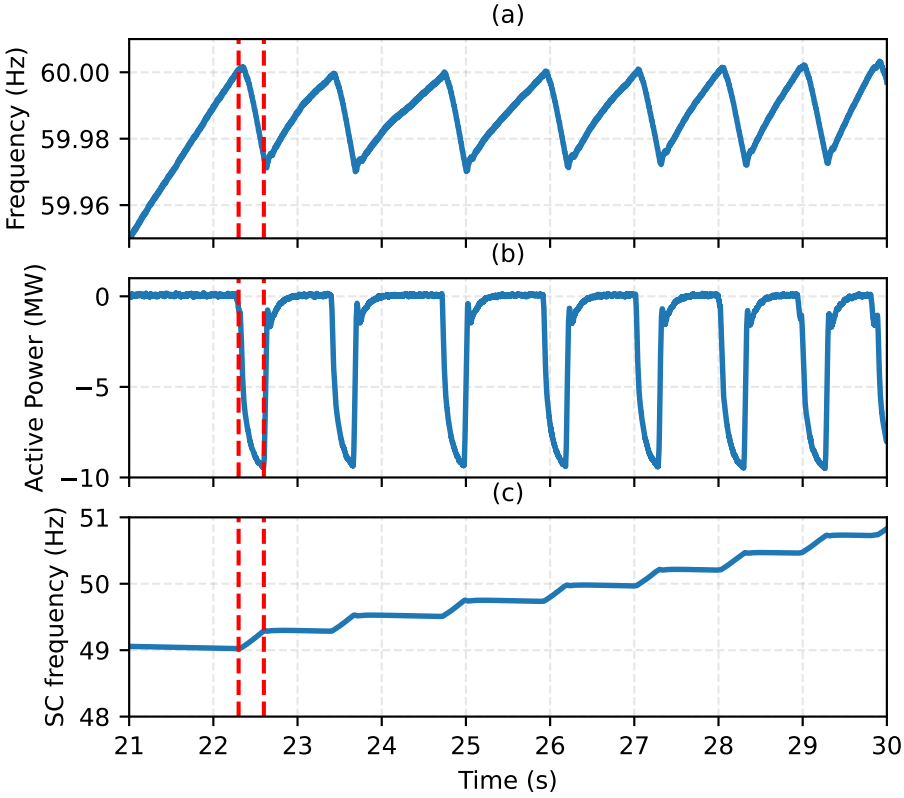

Figure 4.4: Synchronous Condenser speed recovery

As shown in the BtB-SC block diagram (Fig. 3.6), when the system frequency approaches 60 Hz (error less than 0.02 Hz), the BtB-SC absorbs a modicum of power from the ac system to bring the SC speed back to rated (shown in block I, Fig. 3.6). Fig. 4.4 shows a portion of the system frequency indicating that active power exchange starts approximately at 22.1 s when the frequency error $\Delta\omega$ drops below 0.02 Hz and triggers the active power injection

(see Fig. 3.6 (a) rightmost diamond block) to restore the SC speed as shown in Fig. 4.4 (b). The SC speed shown in Fig. 4.4 (c) is seen to move toward its rated value and is attained outside of the shown graph area. When the rated SC speed is achieved, the switch S_1 is closed using a standard synchronization relay.

Benchmarking BtB-SC Against High-Rating, High-Inertia Synchronous Condensers

As noted earlier, the proposed BtB-SC device provides superior inertia and voltage support performance. An interested engineer may ask the question, "What if I had used a conventional SC of much larger rating or inertia, rather than introduce the additional BtB-VSC Converters and the added complexity of additional control?" Accordingly, this section evaluates the frequency and voltage performance of the ac system when supported by the proposed BtB-SC against a conventional SC with: i) four times the power rating (260 MVA, H = 5 s) and ii) one with four times the inertia constant (65 MVA, H = 20 s) under a remote three-phase fault applied at $t = 0.5$ s. As shown in Fig. 4.5, the 65 MVA BtB-SC ($H = 5$ s) achieves significantly faster and better-damped frequency recovery, settling in 9.6 s compared to 12.6 s for both the four-times-rated conventional SC (260 MVA, $H = 5$ s) and the four-times-inertia unit (65 MVA, $H = 20$ s). Furthermore, Fig. 4.6 illustrates the corresponding post-fault voltage profiles. The proposed BtB-SC restores terminal voltage to the nominal value more rapidly (recovering 50 ms faster than the 260 MVA SC and 90 ms faster than the high-inertia unit ($H = 20$ s)) while substantially mitigating temporary overvoltage excursions, reducing peak overvoltage by 5% and 8% relative to the two conventional benchmarks, respectively.

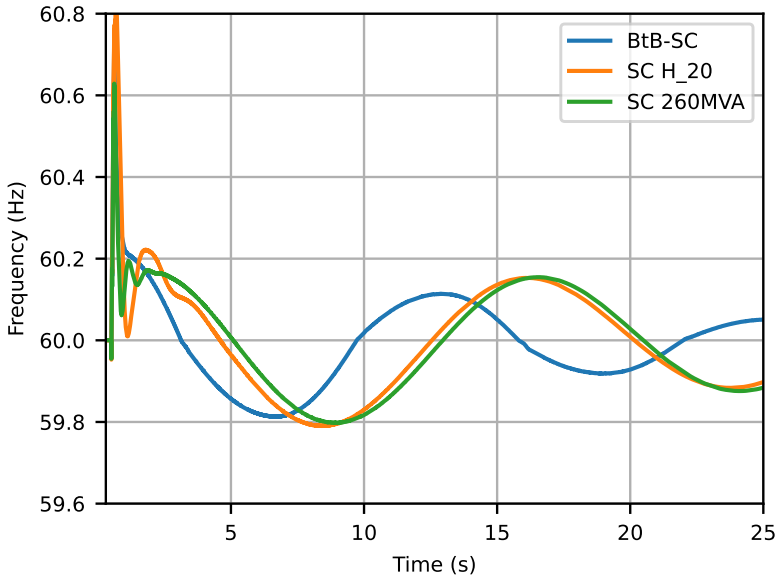

Figure 4.5: Frequency regulation comparison for LCC-HVDC system using high-rating and high-inertia stand-alone SC and BtB-SC

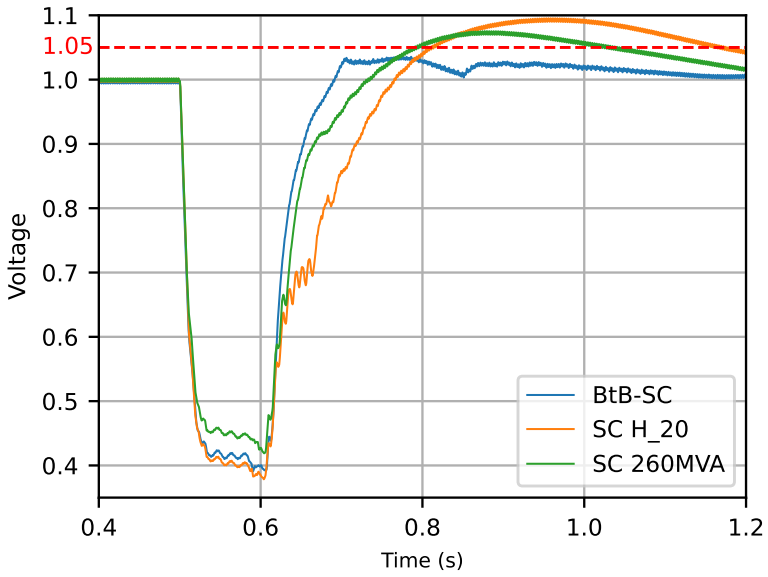

Figure 4.6: Voltage regulation comparison for LCC-HVDC system using high-rating and high-inertia stand-alone SC and BtB-SC

Impact of VSC Rating on *RoCoF*

In some systems, it is critical to limit the *RoCoF* below a specified value in order to ensure a stable recovery after a major fault. Immediately following a disturbance, frequency can change rapidly, resulting in a high *RoCoF*. Controlling *RoCoF* at this stage requires that converters exchange significant active power with the ac grid. However, the maximum current that voltage source converters can supply is limited by the ratings of their IGBTs, so the amount of power exchange—and therefore the extent to which *RoCoF* can be reduced—is inherently constrained. Even if the system parameter K_2 is set very high, a VSC cannot transfer unlimited amounts of power, and as a result, there is an effective lower bound for *RoCoF* determined by the converter's rating. To achieve a further reduction in *RoCoF*, the only option is to increase the VSC rating, which comes with higher costs and maintenance. Fig. 4.7(b), which further reduces the *RoCoF* immediately after the disturbance.

Assume that parameter K_2 is set to 170 pu/pu with the intention of further decreasing the *RoCoF*. Then the converter rated at 70 MVA would reach its maximum current limit of 1.15 pu (5.98 kA), restricting further power exchange, as shown in Fig. 4.7 (a). By increasing the converter rating by 20% to 85 MVA, additional active power, as illustrated in Fig. 4.7(c), can be supplied to the ac network without exceeding the VSC current limit of 1.15 pu (7.26 kA), according to Fig. 4.7(b).

As illustrated in Fig. 4.8, the *RoCoF* achieved with the higher-rated converter is 0.4 Hz/s, while the smaller converter exhibits a *RoCoF* of 0.44 Hz/s. These results demonstrate that a 20% increase in the VSC rating yields a 10% reduction in *RoCoF*, thereby validating how upsizing the converter improves system dynamic performance by enhancing frequency stability following a disturbance.

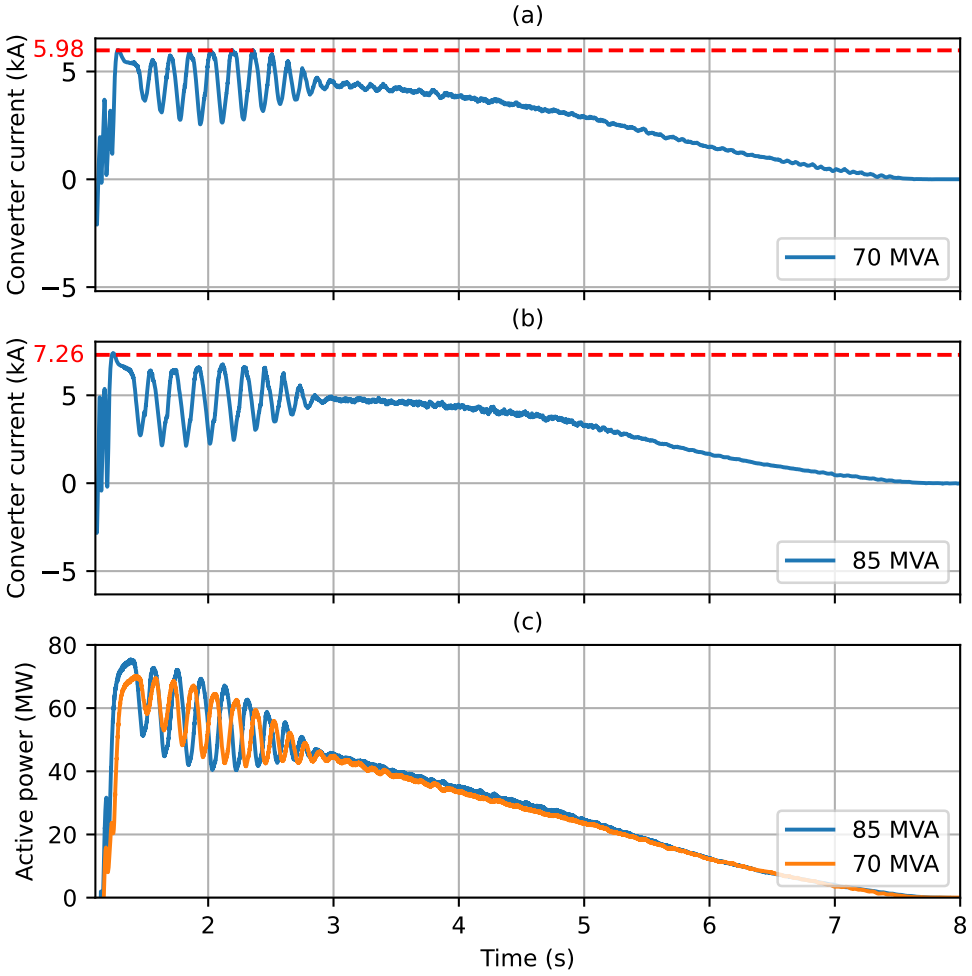

Figure 4.7: Direct-axis current profile for 70 MVA (a) and 85 MVA (b) converter ratings, active power (c)

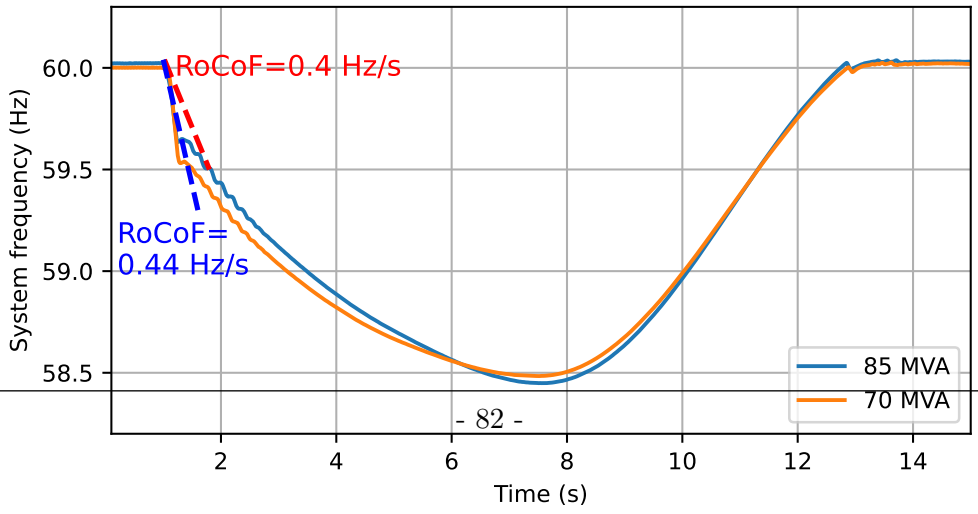

Figure 4.8: Post-contingency frequency recovery profiles for 70 MVA and 85 MVA converter ratings

Damping Contribution of Proposed BtB-SC Arrangement

In addition to inertia support, the controller parameter K_1 allows the BtB-SC to also improve damping of electromechanical modes (see (3.8)). In this case, K_1 is chosen as 20 pu/pu, ensuring that the hybrid system delivers 1 pu of power for a frequency deviation of 0.05 pu [77]. In this example, K_2 was set to zero as the aim was to demonstrate only the damping effect. In an actual application, both K_1 and K_2 would likely be non-zero.

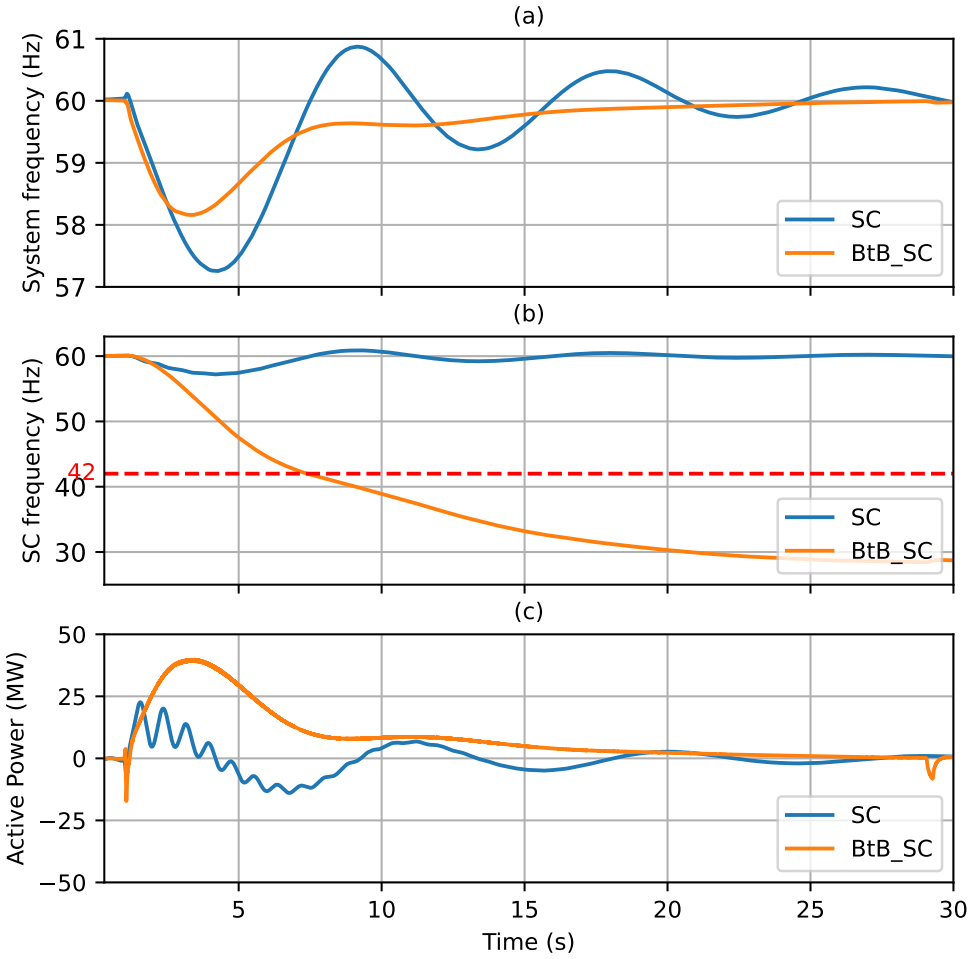

Figure 4.9: System performance comparison: standalone SC vs. BtB-SC with $K_2 = 0$ during a frequency event

As shown in Fig. 4.9 (a), with the SC directly connected to the ac grid (i.e., the standalone SC case), the frequency nadir is 57.25 Hz. However, when the BtB-SC is connected, the frequency response is significantly more damped, with a nadir of only 58.15 Hz. Since the SC is no longer synchronously connected, its speed drops to 28.5 Hz. The controller has been designed to reduce the deceleration (i.e., rate of change) of SC speed when its speed falls below 0.7 pu or 42 Hz. This ensures that the machine speed does not deviate too far, making resynchronization more challenging. Due to this, in Fig 4.9 (b), it can be seen that the rate of change of SC speed changes at $t = 7.5$ s when the SC speed reaches its lower limit threshold of 42 Hz. Fig 4.9 (c) shows that the BtB-SC provides significantly greater active power contribution than a standalone SC.

Impact of Combined Inertia and Fast Frequency Support of BtB-SC

For enhanced damping of electromechanical oscillations in the case study with BtB inertia of 30 s ($K_2 = 60$ pu/pu), the controller parameter K_1, which is responsible for the damping is set to a value of 4 pu/pu. As a result, the frequency response shows a higher frequency nadir, reduced oscillatory behavior, faster decay of oscillation, and a faster return to steady state, while the initial rate of change of frequency remains unchanged, as illustrated in Fig. 4.10.

Increasing K_2 enhances frequency regulation by progressively reducing the $RoCoF$; however, this improvement continues only until the machine-side VSC's active power controller reaches its maximum current limit, beyond which the $RoCoF$ plateaus. Similarly, increasing K_1 enhances the damping of the frequency response; however, this increased damping is accompanied by a slower system response. Consequently, if K_1 is set excessively high, the frequency recovery time becomes prolonged, potentially compromising system's timely response.

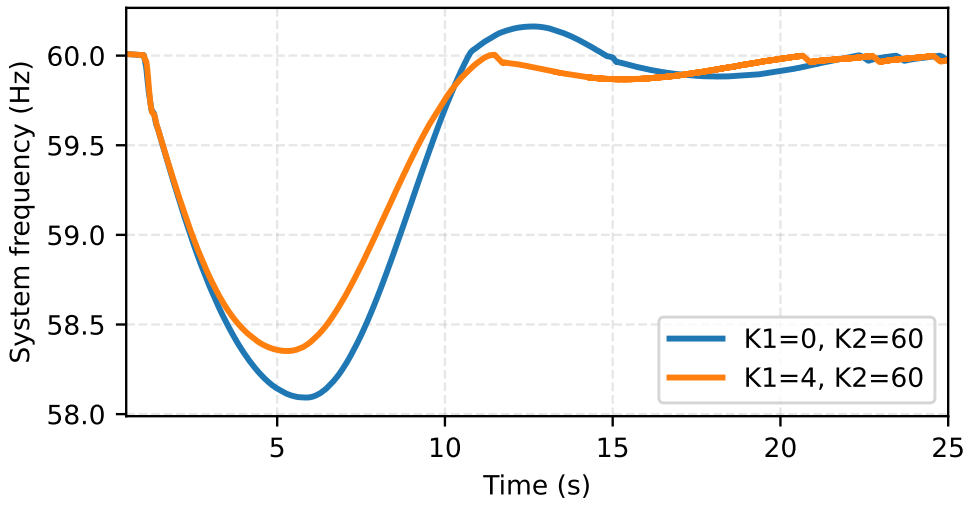

Figure 4.10: Frequency regulation for LCC-HVDC system using BtB-SC with $K_1 = 4$ and $K_2 = 60$ during a frequency event

4.2 Optimizing BtB-SC Virtual Inertia for Frequency Regulation

To achieve optimal frequency regulation, it is essential to select both K_1 and K_2 parameters appropriately, balancing their complementary effects on damping and rate of change of frequency. These parameters can be tuned using optimization algorithms, such as particle swarm optimization (PSO) [78] or genetic algorithms (GA) [79], among others. This chapter demonstrates how frequency regulation can be substantially enhanced using such optimized parameters. The genetic algorithm is selected in this thesis due to its robust global search capability and high customization, enabling the integration of diverse constraints and objectives [80]. Unlike certain optimization methods prone to converging at local optima, GA works well with non-linear multi-modal functions and reliably identifies the global optimum [81].

Although this thesis does not aim to explore different optimization methods, but rather to leverage optimization toward a specific objective, the nonlinear Simplex method of Nelder and Mead [82], integrated within PSCAD, was initially employed due to its perceived simplicity and speed relative to GA. However, its results proved highly sensitive to user-specified initial conditions; even after 2000 iterations, the parameters oscillated around these initial values without approaching the true optima when starting far from the optimal solution. On the other hand, GA was easy to implement and provided good performance and converged without oscillation. However, any other optimization algorithm capable of solving these functions could be selected.

4.2.1 Background of Genetic Algorithm

This section focuses on the selection of the active power order controller parameters, K_1 and K_2, for the BtB-SC system equipped with a VSC rated at 70 MVA. The primary objective is to optimize these parameters to achieve the fastest possible post-contingency frequency recovery, specifically by minimizing the area denoted as cross section A in Fig. 4.11, which quantifies the frequency deviation over time. As shown in the figure, A is the time integral of the absolute frequency over the recovery interval $[t_0,t_f]$. Here, t_0 is the point at which the disturbance is applied, and t_f is the time when the frequency first reaches its rated value. Of course, t_f will be different for each set of trial parameters.

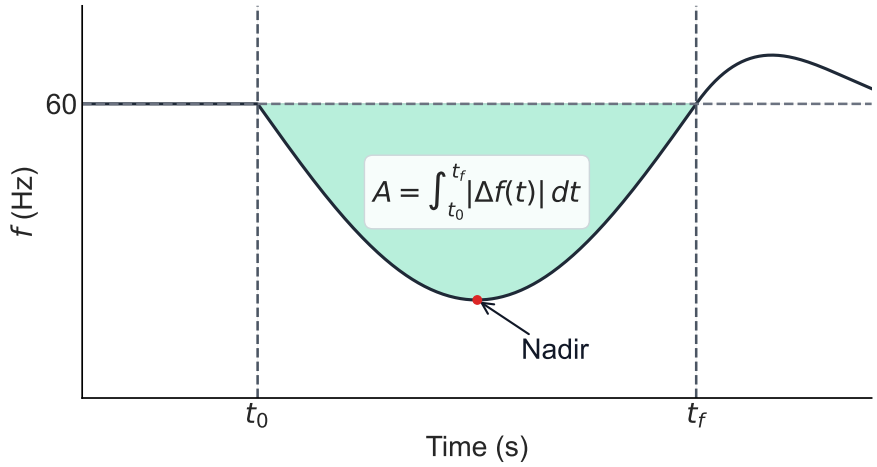

Figure 4.11: Post-contingency crossrecovery profiles for different K_1 and K_2 settings; area A denotes recovery speed

A genetic algorithm, as illustrated in Fig. 4.12, is employed in this thesis to optimize the K_1 and K_2 parameters of the BtB-SC.

GA is a meta-heuristic optimization method inspired by the natural evolutionary process, whereby a population of candidate solutions evolves over successive generations. Through mechanisms such as selection, crossover, and mutation, the algorithm iteratively improves the parameter sets, progressively steering the system toward enhanced performance in terms of frequency recovery.

$$f_1 = \min_{K_1, K_2} \; A(K_1, K_2) + P(K_1, K_2) \tag{4.5}$$

The GA operates on a population $\mathbf{P}_o = \{\vec{S}_1, \vec{S}_2, \ldots, \vec{S}_N\}$, where each individual solution n is $\vec{S}_n = [K_{1_n}, K_{2_n}]$. Starting from an initial population $\mathbf{P}_{o_1}$, the GA evolves over G generations. At each generation g, offspring $\mathbf{Q}_{o_g}$ are created using **arithmetic crossover** (Algorithm 1), followed by **random mutation** (Algorithm 2).

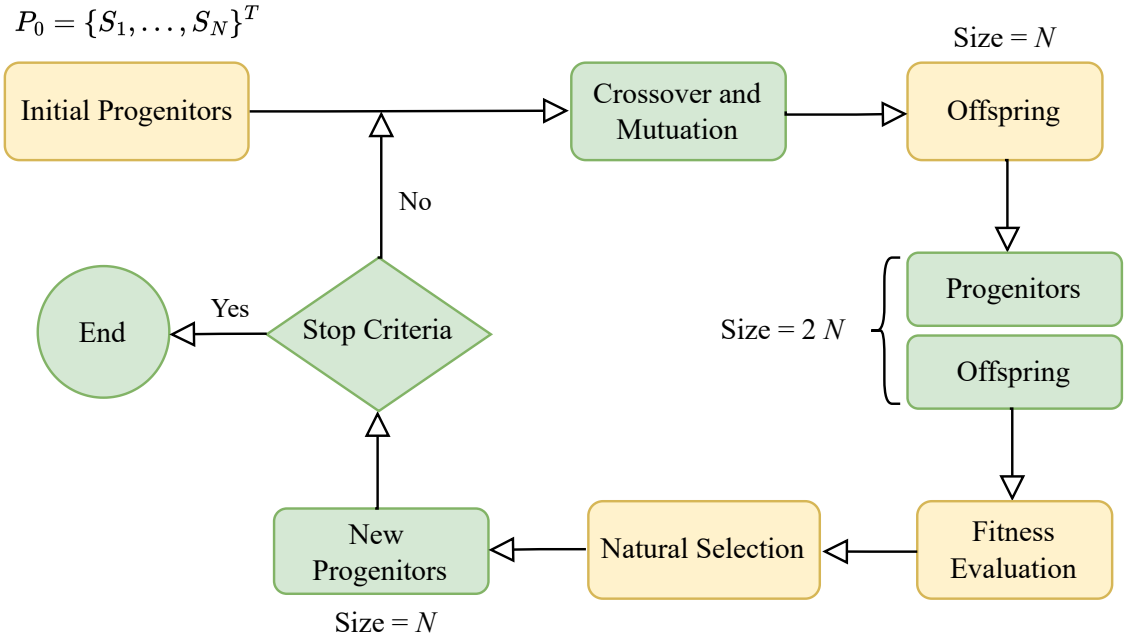

Figure 4.12: Flowchart of the Genetic Algorithm

After mutation, parents and offspring are merged: $\mathbf{P}_{o_g} \leftarrow \mathbf{P}_{o_g} \cup \mathbf{Q}_{o_g}$. If a solution falls outside the limits, constraint handling is applied to put it back in the feasible solution space. Then, a **modified tournament selection** (Algorithm 2) reduces the population to N individuals for the next generation $\mathbf{P}_{o_{g+1}}$. The modified tournament balances exploitation and diversity, helping avoid premature convergence. The operational parameters adopted for the Genetic Algorithm are detailed in Table 4.1.

By employing this bio-inspired optimization strategy, the study systematically explores the solution space for K_1 and K_2, ultimately identifying parameter combinations that yield the best frequency response recovery for the given scenario. A constraint is included in the optimization where any candidate parameters resulting in a nadir frequency below 58.5 Hz are penalized. Another constraint is that the magnitudes of the VSC's currents must

Algorithm 1 Arithmetic Crossover

while $|\mathbf{Q}_{o_g}| < N$ **do**
  Select two parents $\vec{p1}_d$, $\vec{p2}_d$ from $\mathbf{P}_{o_g}$
  if random $\alpha_0 \leq$ crossover probability **then**
    for $d = 1$ to size($\vec{p1}_d$) **do**
      $\alpha \leftarrow$ random $\in [0, 1]$
      $q1_d \leftarrow \alpha p1_d + (1 - \alpha)p2_d$
      $q2_d \leftarrow \alpha p2_d + (1 - \alpha)p1_d$
    Add $q1$, and if needed $q2$, to $\mathbf{Q}_{o_g}$

Algorithm 2 Modified Tournament

for each $\vec{S}_n \in \mathbf{P}_{o_g}$ **do**
  $\vec{S}_{n_{score}} = 0$
  Randomly select $0.2N$ competitors $\mathbf{P}_t$ from $\mathbf{P}_{o_g}$
  for each $\vec{S}_{n_2} \in \mathbf{P}_t$ **do**
    if $f_1(\vec{S}_n)$ ¡ $f_1(\vec{S}_{n_2})$ **then**
      $\vec{S}_{n_{score}} += 1$
Select top N individuals with highest scores for $\mathbf{P}_{o_{g+1}}$

be below the converter's maximum current limit of 1.15 pu. This approach ensures that only feasible solutions meeting these critical system constraints are considered as potential candidates. The case described in Section 4.1.2 was optimized. This case considers the tripping of the largest generator (1000 MW), which also has the biggest inertia constant (5 s), making it the worst case as for the largest $RoCoF$ and lowest frequency nadir. The GA was performed considering a population of 20 individuals, evolving during 100 generations, with a mutation probability of 5%, and a modified tournament comprised of groups of 40% of the population size. The resulting frequency recovery and converter current plots after optimization are shown in Figs. 4.13 (a) and (b), respectively. The optimized gains are $K_1 = 9.107$ and $K_2 = 102.336$. For comparison, the plot also shows the original responses when K_1 and K_2 were selected by human judgment without much trial and error. After

Table 4.1: Genetic Algorithm Configuration Parameters

Parameter	**Value**	**Parameter**	**Value**
Initial Population Size	20	Automatic Standard Deviation (Real Mutation)	Enabled
Maximum Number of Generations	100	Standard Deviation for Mutation of Real Variables	0.01
Mutation Prob. (Binary & Integer)	5%	Population Sorting Method	Elitist
Mutation Prob. (Real Variables)	5%	Percentage of Competitors (Tournament)	40%
Lower Limit (Variable 1)	-110.0	Upper Limit (Variable 1)	-10.0
Lower Limit (Variable 2)	-20.0	Upper Limit (Variable 2)	0.0

optimization, the frequency nadir is improved to 58.8 Hz from the original value of 58.1 Hz, and the optimized $RoCoF$ is 0.56 Hz/s instead of the original 0.8 Hz/s. This corresponds to a virtual inertia of 8.1 s as opposed to the 5.66 s without optimization and 2.79 s with the stand-alone SC. Also, as seen from Fig. 4.13 (b), the optimized current remains within the converter limit of 1.15 pu, although it is larger than that of the unoptimized case. Note that the larger current is the reason why the higher virtual inertia is achieved.

As mentioned, the optimized parameters, $K_1 = 9.107$ and $K_2 = 102.336$, were derived based on the worst-case disturbance scenario to maximize frequency support. To evaluate robustness, this optimized parameter set was also applied at other operating conditions and showed good results. For example, consider the case previously discussed in Section 3.5, involving a 200 ms three-phase bolted fault at the inverter ac busbar.

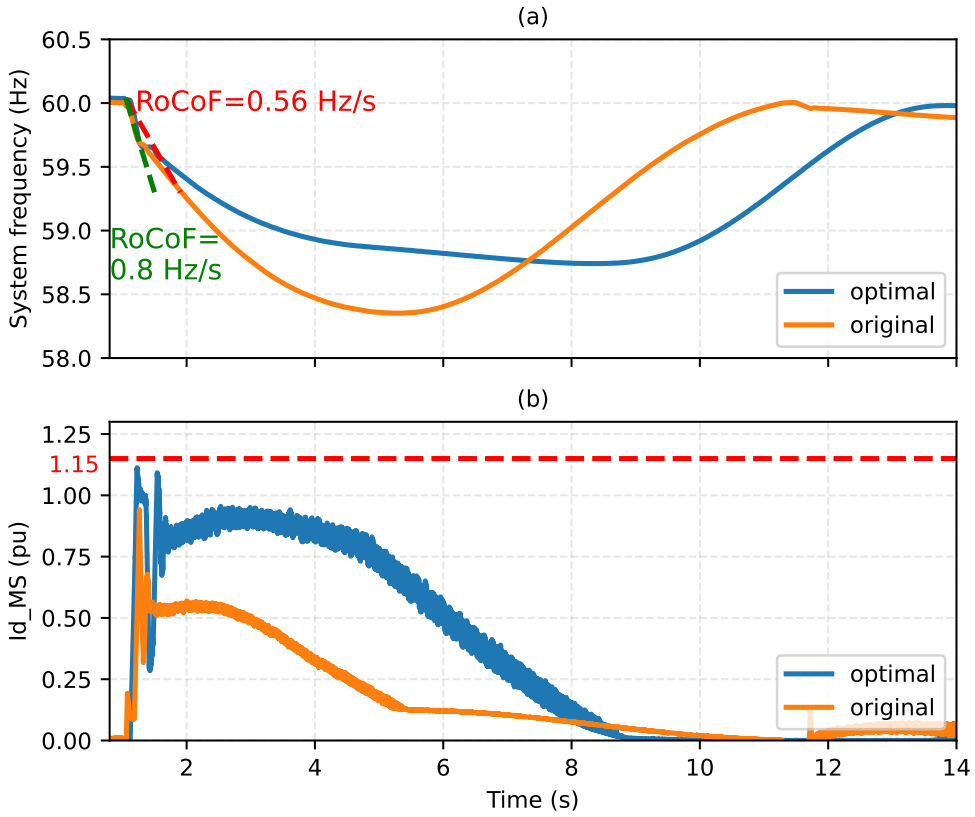

Figure 4.13: Comparison of post-contingency frequency recovery for K_1=4, K_2=60, and the optimal results achieved by the genetic algorithm at K_1=10.6008, K_2=102.062

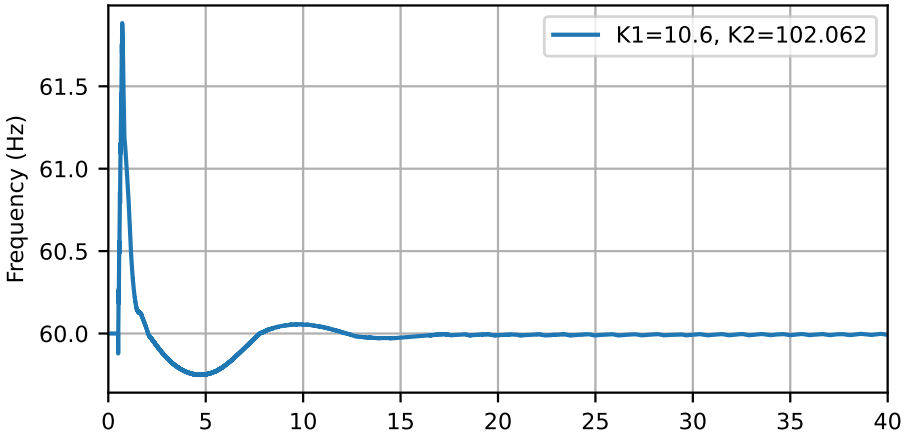

Figure 4.14: Post-contingency frequency recovery performance, achieved using the control parameters optimized via a Genetic Algorithm ($K_1 = 10.6008$, $K_2 = 102.062$)

The performance of the BtB-SC with optimized parameters, as illustrated in Fig. 4.14, is very similar to the performance in the case presented in Fig. 3.18, which was tuned by trial and error. These results demonstrate the robustness of the proposed settings, provided the system load remains constant, and the LCC-HVDC operates at its nominal rated active power. However, under extreme operating conditions involving severe power imbalances, a more aggressive inertial response may be necessary to maintain the optimized frequency profile.

4.3 Summary

Using electromagnetic transient (EMT) simulations, this chapter evaluates the performance of the proposed BtB-SC topology and demonstrates its substantial advantages over a standalone synchronous condenser.

During voltage disturbances, the BtB-SC delivers significantly higher reactive power than a standalone SC, enabling faster voltage recovery. For frequency transients, the asynchronous connection between the SC and grid facilitates large energy exchanges with the ac network, yielding higher apparent inertia, smaller frequency deviations, and reduced RoCoF compared to the standalone SC.

Increasing the VSC rating further mitigates $RoCoF$ by allowing greater power exchange without exceeding IGBT current limits. Using Genetic Algorithm, the active power controller parameters were further successfully optimized to give lowest $RoCoF$ and highest nadir for the worst case disturbance of the tripping of the largest generator.

Chapter 5

Online Inertia Estimation of Inverter-Based Resources

This chapter proposes a new method to quantify the inertia contributed by the BtB-SC and other inverter-based resources (IBRs), and examines the frequency support provided to a low-inertia ac system by BtB-SC and VSG-based HVDC converters. The method extends a recently introduced probing-based approach presented in [29], in which inertia is estimated from the steady-state active power and virtual speed deviations resulting from a sinusoidal voltage or current injection at a specified frequency. The concept is first demonstrated using a synchronous generator (SG), as well as a grid-forming virtual synchronous generator implemented through the control of a voltage source converter. Subsequently, it is applied to investigate inertia measurement in the proposed BtB-SC device, using the system configuration shown in 3.4.

The approach proposed in [29] has been tested for the classical model of generators and IBRs emulating classical generator models. To estimate the inertia contribution of

grid-forming IBRs, the electrical frequency in the converter controller is used in [29]. A limitation of this approach is its inherent dependence on the converter internal speed signal, which may not be available if the controller has been provided by the manufacturer in a "black-boxed" form, i.e., the internal structure and parameters are not accessible. Although the use of *nearby* synchronously connected generators has been proposed to estimate the virtual speed deviation for grid-following converters, this is particularly challenging when the inertia capability of asynchronously connected converters needs to be estimated. Regarding the BtB-SC as a grid-following IBR connected to the ac network, access to the speed of a close synchronous generator is required to isolate the BtB-SC contribution. Thus, if the controller of the active power order is black-boxed, precluding use of Eq. (3.14), an alternative method independent of the surrounding network is essential.

Motivated by these concerns, this chapter investigates the applicability of the bus voltage frequency signal as a suitable replacement for the virtual speed signal, which is externally accessible and eliminates the need for proprietary internal signals for calculating the inertial characteristics of converter-based systems. This distinction makes the method particularly valuable for black-boxed commercial controllers and asynchronously connected converters. The probing signal injection can be used as an excitation to the system. The inertia of the IBR/synchronous generator under test is then estimated using the measured active power and the bus frequency at its terminals. The bus frequency can be measured using a Phase-Locked Loop (PLL), whose bandwidth must be sufficiently high to capture the steady-state deviations accurately in the frequency range of interest. Using the well-known classical model of synchronous generators, the chapter first derives the analytical relationship to understand whether the bus frequency deviations can replicate the behavior of the rotor speed signal accurately.

5.1 Probing Signal Based Inertia Measurement [29]

The electro-mechanical dynamics of a synchronous generator are characterized by its inertia constant H, which is a measure of the stored kinetic energy in its rotating mass. This stored energy helps to impede frequency changes during disturbances such as sudden changes in power generation or consumption. The electro-mechanical dynamics of the classical model of a synchronous generator can be represented using the well-known "swing" equation, as given in (5.1).

$$\begin{aligned} \frac{d\delta}{dt} &= (\omega_r - \omega_o) \\ \frac{2H}{\omega_B}\frac{d\omega_r}{dt} + D\,(\omega_r - \omega_o) &= T_m - T_e \end{aligned} \tag{5.1}$$

where δ and ω_r denote the electrical angle (with respect to a reference axis) and the electrical speed of the rotor, respectively. The variables ω_o and ω_B denote the steady-state electrical frequency of the system (in rad/s) and the base frequency (in rad/s), respectively. T_m and T_e represent the mechanical torque and electrical torque (in per unit), respectively, and D denotes the damping of the machine. Since the synchronous generator frequency is usually very close to the steady-state frequency (i.e., $\omega_r \approx \omega_o$), then T_m and T_e can be substituted by the mechanical power P_m and electrical power P_e of the machine, respectively, in per unit.

For small-signal analysis, the system can be linearized about the quiescent operating point. The mechanical power can be assumed to be constant since the associated turbine is much slower compared to the electrical power variations. Therefore, the transfer function between the electrical power deviation $\Delta P_e(s)$ and the speed variation $\Delta\omega_r(s)$ of a synchronous

machine is as follows:

$$\frac{\Delta\omega_r(s)}{\Delta P_e(s)} = \frac{-1}{\frac{2H}{\omega_B}s + D} \tag{5.2}$$

At a certain frequency $s = j\Omega$, the frequency response satisfies the following relationship.

$$\frac{\omega_B \left|\Delta P_e(j\Omega)\right|}{2\Omega \left|\Delta\omega_r(j\Omega)\right|} = \left|H + \frac{D\omega_B}{2j\Omega}\right| = H_m \tag{5.3}$$

Note that (5.3) refers to the frequency response of the synchronous machine when excited by a modulating signal of frequency Ω. This can be achieved either by injecting a small-amplitude modulating voltage V_h or a current signal I_h of frequency $\Omega_h = (\omega_o - \Omega)$, as shown in Fig. 5.1. The injected voltage and/or current signals are posed on top of the quiescent voltage and/or current sources in the circuit (usually 50/60 Hz). Their magnitude should be minimized to avoid disturbing circuit operation, but not so small that noise effects become significant.

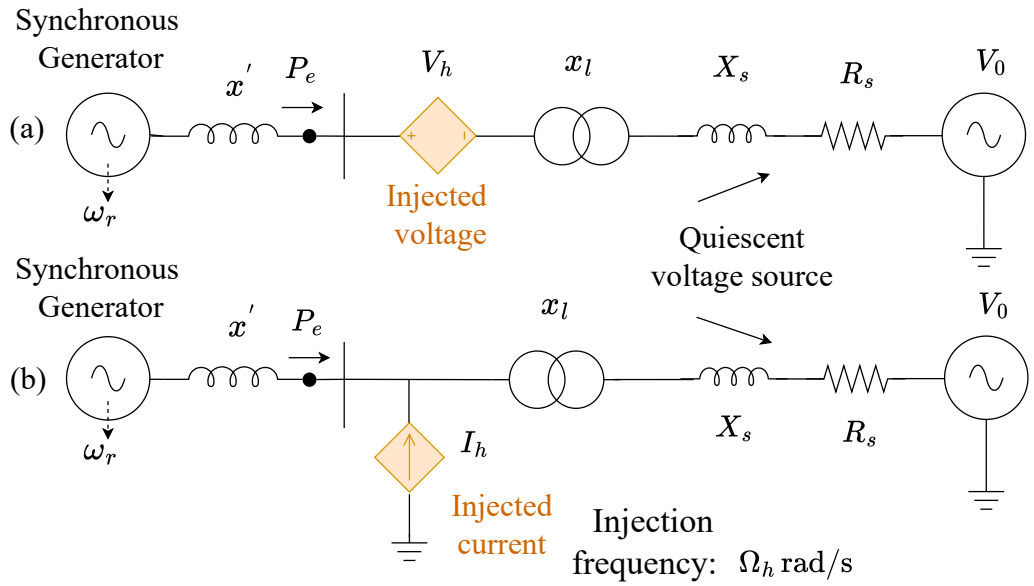

Figure 5.1: Probing frequency injection (a) Voltage injection (b) Current injection

For synchronous machines, D is usually very small and therefore, the inertia estimate H_m calculated using (5.3) gives the inertia constant with reasonable accuracy i.e. $H_m \approx H$. If the damping term D is large, the inertia constant H can be calculated accurately by doing two independent measurements at two different injection frequencies [29]. If the measured inertia is H_{m1} at an injection frequency of f_1 Hz, and the inertia measurement is H_{m2} at injection frequency f_2 Hz, then the inertia H can be calculated as follows [29]:

$$\begin{cases} H_{m1}^2 = H^2 + \dfrac{D^2\omega_B^2}{4(2\pi\Delta f_1)^2} \\ H_{m2}^2 = H^2 + \dfrac{D^2\omega_B^2}{4(2\pi\Delta f_2)^2} \end{cases} \implies H = \sqrt{\frac{H_{m1}^2\Delta f_1^2 - H_{m2}^2\Delta f_2^2}{\Delta f_1^2 - \Delta f_2^2}} \tag{5.4}$$

where $\Delta f_1 = (f_o - f_1)$ Hz, $\Delta f_2 = (f_o - f_2)$ Hz and $f_o = \dfrac{\omega_o}{2\pi}$ Hz. In practice, the terminal voltage of the machine is regulated using an automatic voltage regulator [83]. The injection

of a probing "voltage" signal at the terminals (point of voltage regulation) of the machine creates an inconsistency, resulting in an erroneous inertia measurement.

Illustrative Example: A 100 MVA, 15 kV synchronous generator is connected to a 132 kV three-phase ac source through a 15/132 kV transformer, whose parameters and the quiescent operating condition are shown in Fig. 5.2. To test this probing frequency injection method, the system is simulated at this operating point in the PSCAD/EMTDC program.

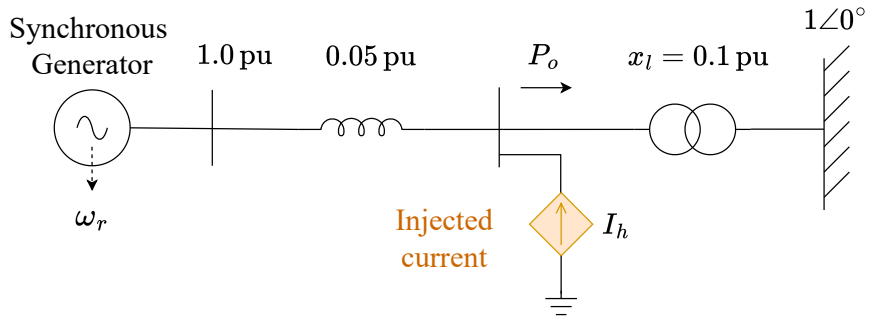

Figure 5.2: Schematic for inertia measurement of synchronous generator

The inertia measurement is performed using the current injection method, with a current source of magnitude $I_h = 0.05$ kA for a range of mechanical damping values and quiescent operating conditions. To account for the effect of the damping, the inertia is calculated using two different frequencies, as given in (5.4). These results are reported in Table 5.1 along with the combination of injection frequencies.

As an illustrative example consider the case with damping $D = 0.026$ pu/rad/s and active power $P_o = 0.9$ pu. The injected frequency components are $f_{h1} = 59.5$ Hz and $f_{h2} = 59$ Hz i.e. $\Delta f_1 = 0.5$ Hz and $\Delta f_2 = 1$ Hz. In steady-state, for Δf_1, the amplitudes of the active power deviation is $|\Delta P_{e1}(j\Omega)| = 0.00008$ pu and the rotor speed deviation is $|\Delta\omega_{r1}(j\Omega)| = 0.00141$ rad/s. Similarly, with injection frequency Δf_2 we obtain $|\Delta P_{e2}(j\Omega)| = 0.00041$ pu

Table 5.1: Inertia measurement for classical generator model

		Second injection frequency (Δf_2 in Hz)				
Damping (in pu/rad/s)	Quiescent power (P_o)	0.2 Hz	1	5	10	20
$D = 0.026$	0.1 pu	2.99	2.99	2.99	2.99	3.00
	0.5 pu	2.99	2.99	2.99	2.99	3.00
	0.9 pu	2.99	2.99	2.99	2.99	3.00
$D = 0.053$	0.1 pu	3.00	2.99	2.99	2.99	3.00
	0.5 pu	3.00	2.99	2.99	2.99	3.00
	0.9 pu	3.00	2.99	2.99	2.99	2.99
For all cases, the first injection frequency was $\Delta f_1 = 0.5$ Hz.						

and $|\Delta\omega_{r2}(j\Omega)| = 0.00395$ rad/s. The inertia values are calculated using (5.3) as follows.

$$H_{m1} = \frac{\omega_B \times |\Delta P_{e1}(j\Omega)|}{2 \times (2\pi \times \Delta f_1)\,|\Delta\omega_{r1}(j\Omega)|} = 3.39 \text{ s}$$
$$H_{m2} = \frac{\omega_B \times |\Delta P_{e2}(j\Omega)|}{2 \times (2\pi \times \Delta f_2)\,|\Delta\omega_{r2}(j\Omega)|} = 3.10 \text{ s}$$

The correct inertia constant H can be evaluated from these measurements using (5.4) and is given as follows.

$$H = \sqrt{\frac{H_{m1}^2 \Delta f_1^2 - H_{m2}^2 \Delta f_2^2}{\Delta f_1^2 - \Delta f_2^2}} = 2.99 \text{ s}$$

The inertia measurement approach uses the steady-state variations in the generator rotor speed due to the external injections. However, this necessitates that the inertia of every generator needs to be evaluated separately, and the generator rotor speed measurements be available. For a BtB-SC operating as a grid-following converter connected asynchronously to the grid, measuring its individual inertia support requires access to the converter's internal frequency signal or controller parameters. Otherwise, knowledge of the host network's total

inertia is necessary to isolate the BtB-SC contribution. For grid-forming IBRs emulating classical model characteristics, this approach will require access to the emulated virtual speed. This is particularly challenging since real-life IBR controllers are usually black-boxed by the manufacturers. An alternative signal to the converter's frequency can be the bus voltage frequency, which can be directly obtained from the network measurements. The following section investigates the applicability of the bus frequency measurement instead of the virtual speed for inertia estimation.

5.2 Inertia Estimation directly from Bus Frequency Measurements

The earlier approach used an available rotor speed (or emulated rotor speed in case of a virtual SG) for inertia estimation. This signal may not be available in a simulation as the controllers may be "black-boxed" by the manufacturer, not permitting access to internal variables in the model. So, in this section, I investigate how inertia can be estimated purely from the measurement of bus voltage and frequency.

An important aspect that needs to be analyzed is how to measure the bus frequency. One of the ways to measure the frequency of the measured voltage signal is to use a Phase-Locked Loop (PLL). The parameters of the PLL can affect the accuracy of the bus frequency measurement, which in turn could affect the inertia measurement. Using the D-Q based PLL [84], this phenomenon is analyzed below.

The block diagram of a three-phase D-Q based PLL is shown in Fig. 5.3. The D-Q transformation in (5.5) transforms the a-b-c variables to the D-Q-0 variables, and $\gamma = \omega_o t + \xi$,

ξ being an arbitrary constant.

$$\begin{bmatrix} v_D \\ v_Q \\ v_o \end{bmatrix} = \sqrt{\frac{2}{3}} \begin{bmatrix} \cos(\gamma) & \cos(\gamma - \frac{2\pi}{3}) & \cos(\gamma + \frac{2\pi}{3}) \\ \sin(\gamma) & \sin(\gamma - \frac{2\pi}{3}) & \sin(\gamma + \frac{2\pi}{3}) \\ \frac{1}{\sqrt{2}} & \frac{1}{\sqrt{2}} & \frac{1}{\sqrt{2}} \end{bmatrix} \begin{bmatrix} v_a \\ v_b \\ v_c \end{bmatrix} \tag{5.5}$$

The frequency used in the D-Q transformation ω_o is taken to be the steady-state frequency so that the D-Q variables are constants in the steady state.

The PLL consists of a low-pass de-noising filter to mitigate noise and other high-frequency components in the voltage measurements and provide a clean reference for the PLL [85]. The filtered D-component is then regulated using a P-I controller, whose output determines the measured frequency ω_m. The following analysis derives the small-signal model of the PLL shown in Fig. 5.3 to understand the dynamic behavior of the PLL.

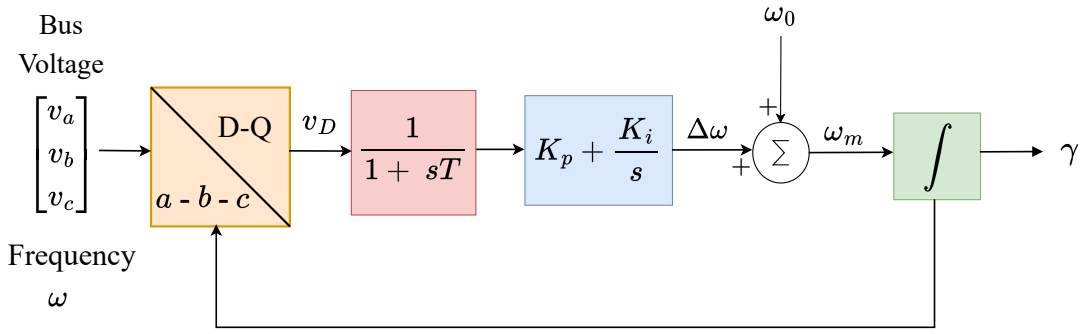

Figure 5.3: Schematic diagram of three-phase PLL

Consider the balanced sinusoidal line-neutral voltages of magnitude V and phase ϕ at the

PLL input, given as follows.

$$\begin{bmatrix} v_a(t) \\ v_b(t) \\ v_c(t) \end{bmatrix} = \sqrt{\frac{2}{3}} \times V \times \begin{bmatrix} \sin(\omega_o t + \phi) \\ \sin\left(\omega_o t + \phi - \frac{2\pi}{3}\right) \\ \sin\left(\omega_o t + \phi + \frac{2\pi}{3}\right) \end{bmatrix} \tag{5.6}$$

The D-Q components are generated using the PLL angle γ. At steady-state, the PLL will lock onto the input voltage waveforms, and therefore the equilibrium value of ω_m will be ω_o. The D-Q voltages can then be written by combining (5.5) and (5.6) as follows.

$$v_D = V\sin(\phi - \xi),\ v_Q = V\cos(\phi - \xi),\ \gamma = \omega_o t + \xi \tag{5.7}$$

It is easy to verify that at the equilibrium point, $\xi_o = \phi_o$, where ϕ_o is the equilibrium value of the voltage phase angle. The small-signal model of the PLL at this operating point can then be represented as follows.

$$\frac{d}{dt}\begin{bmatrix} \Delta x_d \\ \Delta x_i \\ \Delta\xi \end{bmatrix} = \begin{bmatrix} -\frac{1}{T} & 0 & -\frac{V_o}{T} \\ 1 & 0 & 0 \\ K_p & K_i & 0 \end{bmatrix}\begin{bmatrix} \Delta x_d \\ \Delta x_i \\ \Delta\xi \end{bmatrix} + \begin{bmatrix} \frac{V_o}{T} & 0 \\ 0 & 0 \\ 0 & 0 \end{bmatrix}\begin{bmatrix} \Delta\phi \\ \frac{\Delta V}{V_o} \end{bmatrix}$$

The frequency response of the system between the input $\Delta\phi$ and the output $\Delta\xi$ can then be written as follows.

$$\Delta\xi(s) = \frac{(sK_p + K_i)}{s^2(1 + sT) + sK_p + K_i}\Delta\phi(s) \tag{5.8}$$

The frequency $\Delta\omega_m$ and the bus frequency $\Delta\omega$ are related to the PLL output angle ξ and

the bus voltage angle ϕ as follows.

$$\Delta\omega_m = \frac{d\Delta\xi}{dt},\ \Delta\omega = \frac{d\Delta\phi}{dt} \tag{5.9}$$

The overall PLL model between the measured frequency ω_m and the input signal frequency ω can then be obtained by substituting (5.9) in (5.8) and can be written as follows.

$$\begin{aligned} \Delta\omega_m(s) &= \frac{(sK_p + K_i)}{s^2(1+sT) + sK_p + K_i}\Delta\omega(s) \\ \implies G_{pll}(s) &= \frac{\Delta\omega_m(s)}{\Delta\omega(s)} = \frac{(sK_p + K_i)}{s^2(1+sT) + sK_p + K_i} \end{aligned} \tag{5.10}$$

For accurate inertia estimation, the PLL parameters must be carefully chosen so that the frequency response of the PLL is close to $1\angle 0°$ in the injection frequency range.

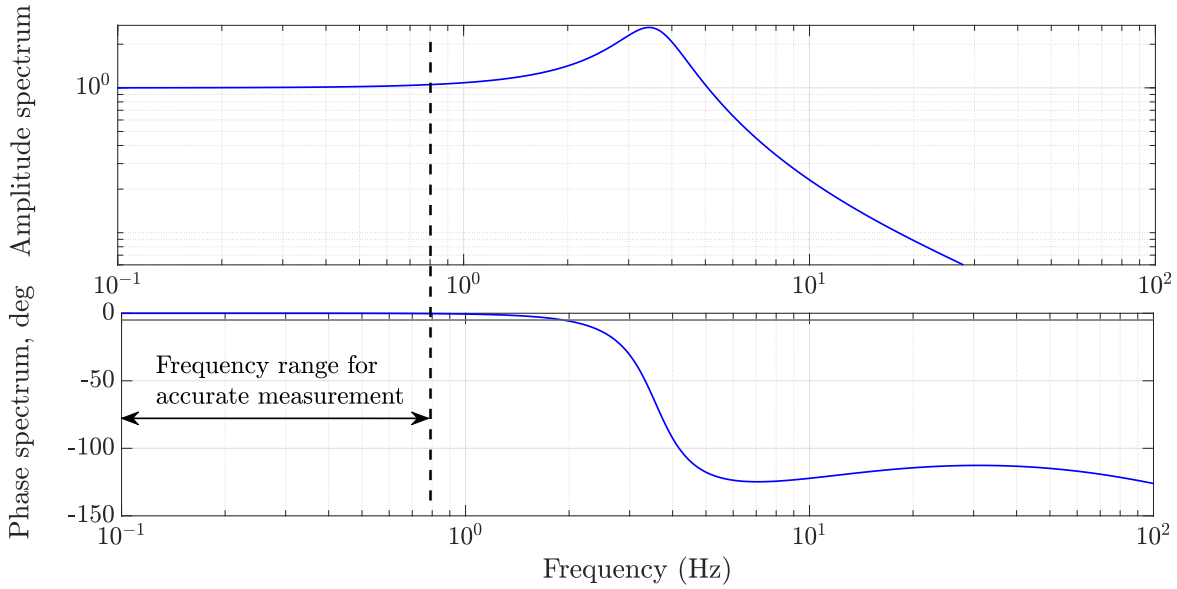

Figure 5.4: Frequency response of three-phase PLL parameters

To demonstrate the accuracy of the estimation, consider a PLL with parameters: $K_p =$

$20, K_i = 500$, and $T = 0.001$ s. The frequency response of the PLL, denoted by $G_{pll}(s)$ in (5.10), is shown in Fig. 5.4 to determine whether the PLL has sufficient bandwidth to accurately measure the steady-state frequency deviations. Note that the selected PLL parameters are appropriate for the measurement of frequency variations (Δf) of 1 Hz around the fundamental frequency, which is sufficient for the proposed scheme.

To verify this, the PLL is connected to a balanced three-phase voltage source of nominal frequency 60 Hz. The source frequency is modulated by a small-amplitude signal, which is given as: $f(t) = 60 + 0.05 \times \sin(2\pi \times \Delta f \times t)$ Hz.

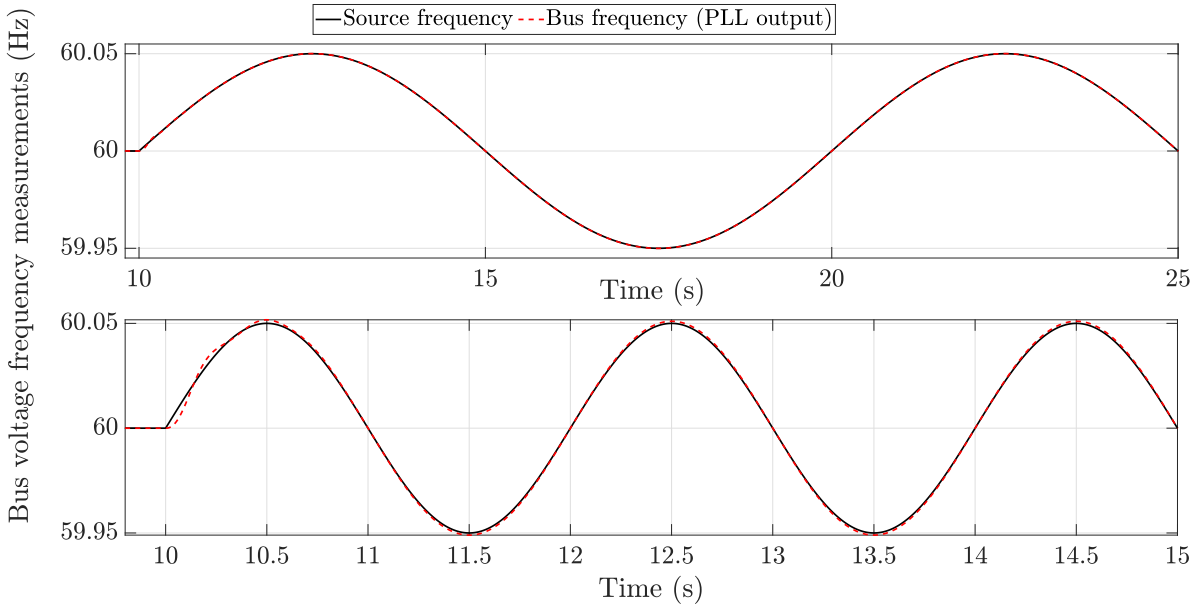

Figure 5.5: Steady-state behaviour of PLL frequency measurement

The PLL output along with the source frequency is shown in Fig. 5.5 for two different modulating frequencies of 0.1 Hz and 0.5 Hz. As expected from the frequency response, these PLL parameters can accurately capture the steady-state perturbations in the input voltage frequency signal. Using this approach, the following section presents the relationship between

the bus frequency and the rotor speed of the classical model of a synchronous generator.

5.2.1 Bus Frequency-based Inertia Measurement of Classical Generator Model

In many studies, it is essential to calculate the apparent inertia as seen from a bus. In that case, the generator is usually available as a software model from which signals like speed are directly available. This section shows how the inertia measurement can be applied to measure the inertia of a software model of a generator. Later, I will show how it can be adapted to estimate the apparent inertia of other configurations, such as grid-forming and grid-following converters, using direct measurements of bus voltage.

The electro-mechanical dynamics of the classical model of a synchronous generator is illustrated in Fig. 5.6. This figure depicts a classical equivalent circuit of a machine as a voltage source of $E_g\angle\delta$ behind impedance x'_d. Let x_g represent the equivalent impedance of the system, which is the sum of the generator internal impedance x'_d and the external network impedance x_l. The generator internal voltage E_g is constant for the classical model. The electro-mechanical dynamics of the classical generator model are defined as follows.

$$\begin{aligned} \frac{d\delta}{dt} &= (\omega_r - \omega_o) \\ \frac{2H}{\omega_B}\frac{d\omega_r}{dt} + D\,(\omega_r - \omega_o) &= T_m - (v_D i_D + v_Q i_Q) \\ E_g\angle\delta - jx_g(i_Q + ji_D) &= v_Q + jv_D \end{aligned} \tag{5.11}$$

Note that H and D denote the inertia constant and the equivalent damping of the generator. The equilibrium values are denoted by the subscript o, e.g., ζ_o is the equilibrium value of the variable ζ. Without loss of generality, it is assumed that the equilibrium values of the

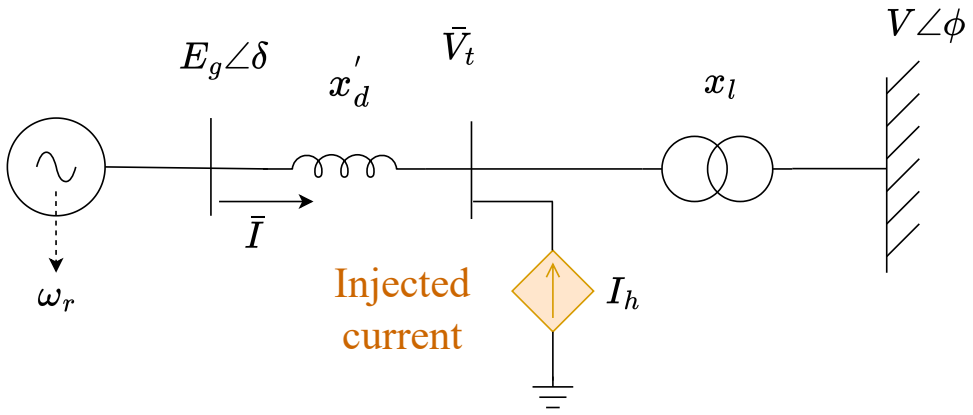

Figure 5.6: Schematic of classical generator connected to infinite bus

terminal voltages are $v_{Qo} = V_o$ and $v_{Do} = 0$. This can be arranged by aligning the D-Q transformation angle with the quiescent terminal voltage phase angle. The dynamical model given in (5.11) is linearized around the equilibrium point and can be written as follows.

$$\frac{d}{dt}\begin{bmatrix}\Delta\delta\\ \Delta\omega_r\end{bmatrix} = \begin{bmatrix}0 & 1\\ -\frac{V_o E_g\cos(\delta_o)}{M x_g} & -\frac{D}{M}\end{bmatrix}\begin{bmatrix}\Delta\delta\\ \Delta\omega_r\end{bmatrix} + \frac{V_o E_g}{M x_g}\begin{bmatrix}0 & 0\\ \cos(\delta_o) & -\sin(\delta_o)\end{bmatrix}\begin{bmatrix}\Delta v_D\\ \Delta v_Q\end{bmatrix} \tag{5.12}$$

where $M = \frac{2H}{\omega_B}$. The probing signal I_h will cause steady-state perturbations of the injection frequency in the input signals Δv_D and Δv_Q. The D-Q components of the voltage are related to their respective polar components as follows.

$$v_D = V\sin(\phi),\ \ v_Q = V\cos(\phi) \tag{5.13}$$

Linearizing, I get

$$\begin{bmatrix} \Delta v_D \\ \Delta v_Q \end{bmatrix} = V_o \begin{bmatrix} \Delta \phi \\ \Delta V_n \end{bmatrix}, \ \Delta V_n = \frac{\Delta V}{V_o}, \Delta\theta = \int \Delta\omega \, dt \tag{5.14}$$

where $\Delta\omega$ denotes the bus frequency deviation. Applying Laplace transform in (5.12) and substituting (5.14), we get

$$\Delta\omega_r(s) = \underbrace{\frac{V_o E_g \cos(\delta_o)}{M x_g s^2 + D x_g s + V_o E_g \cos(\delta_o)}}_{A(s)} \Delta\omega(s) \quad - \frac{V_o E_g \sin(\delta_o)}{M x_g s^2 + D x_g s + V_o E_g \cos(\delta_o)} \Delta V_n(s) \tag{5.15}$$

The deviation in bus frequency $\Delta\omega$ is related to the rotor speed deviation $\Delta\omega_r$ through the transfer function $A(s)$. Note that if the internal reactance of the model were small, i.e., $x_g \approx 0$, then $A(s) = 1$, indicating that the terminal voltage frequency deviation would be a good approximation of the rotor speed deviation. This substitution ensures that our proposed method remains robust even when direct rotor speed measurements are unavailable. This is illustrated with the following numerical case study.

Numerical Case Study

Consider a synchronous generator connected to an infinite bus through an external impedance, as given in (5.11). The equilibrium values of the terminal voltage V_o and the internal voltage E_g are both 1 pu. The steady-state frequency f_o is 60 Hz and the classical model parameters are $H = 3$ s and $D = 0.5$ pu/rad/s. The transformer leakage reactance is $x_l = 0.1$ pu, and the generator is injecting 0.8 pu active power into the network. The frequency response of $A(s)$ is plotted in Fig. 5.7 for different values of x'_d. Note that the frequency response of

the transfer function $A(s)$ is approximately $1\angle 0°$ for frequencies less than 0.4 Hz for both values of x'_d. However, at higher frequencies, the deviation is much larger for higher x'_d, indicating that the rotor speed deviations may not be accurately captured in the bus frequency measurements. The bandwidth of the PLL and the frequency range of the injected signal should therefore cover the frequencies over which $A(s) \approx 1$.

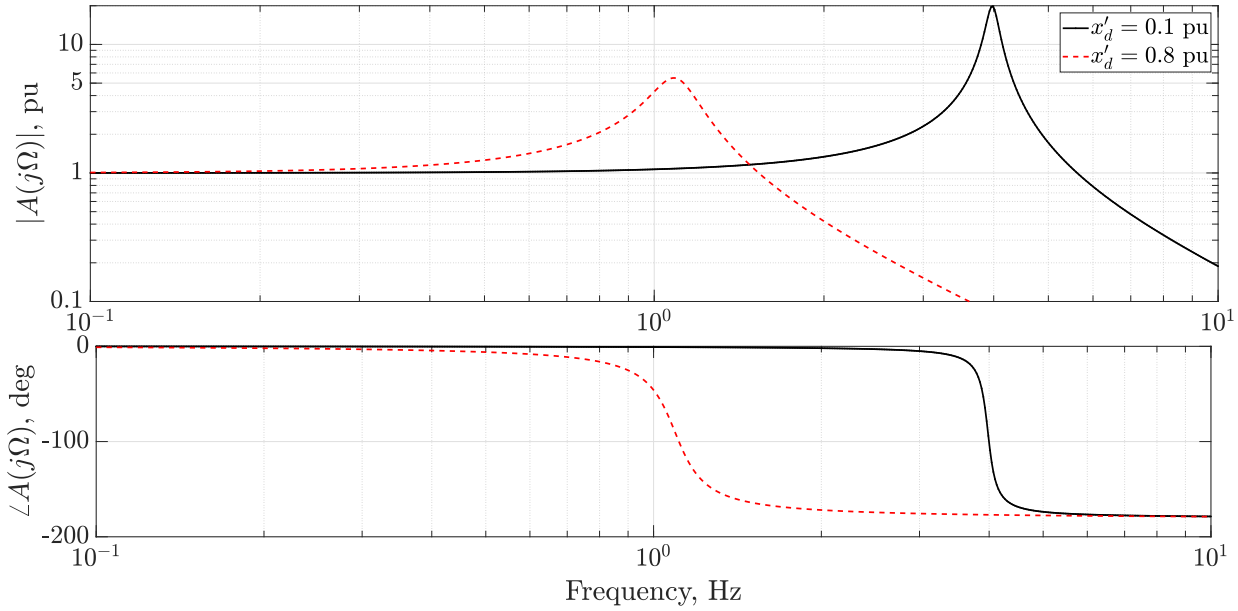

Figure 5.7: Frequency response of $A(s)$ for different values of x'_d

To validate the above, the classical model-based system is simulated in an EMT platform, and the system is probed with a current injection as shown in Fig. 5.1 using the approach described in Section 5.1. The PLL parameters selected here are as follows: $K_p = 20, K_i = 500, T = 0.001$ s. The injection frequency is $\Delta f = 0.3$ Hz, and the steady-state waveforms of the generator terminal voltage frequency *omega* and the rotor speed ω_r are shown in Fig. 5.8 for different values of x'_d. As expected, the mismatch is quite significant when x'_d is higher, which will cause the inertia estimation to be inaccurate. To overcome this limitation,

a compensation strategy for the internal impedance is proposed, which is now explained.

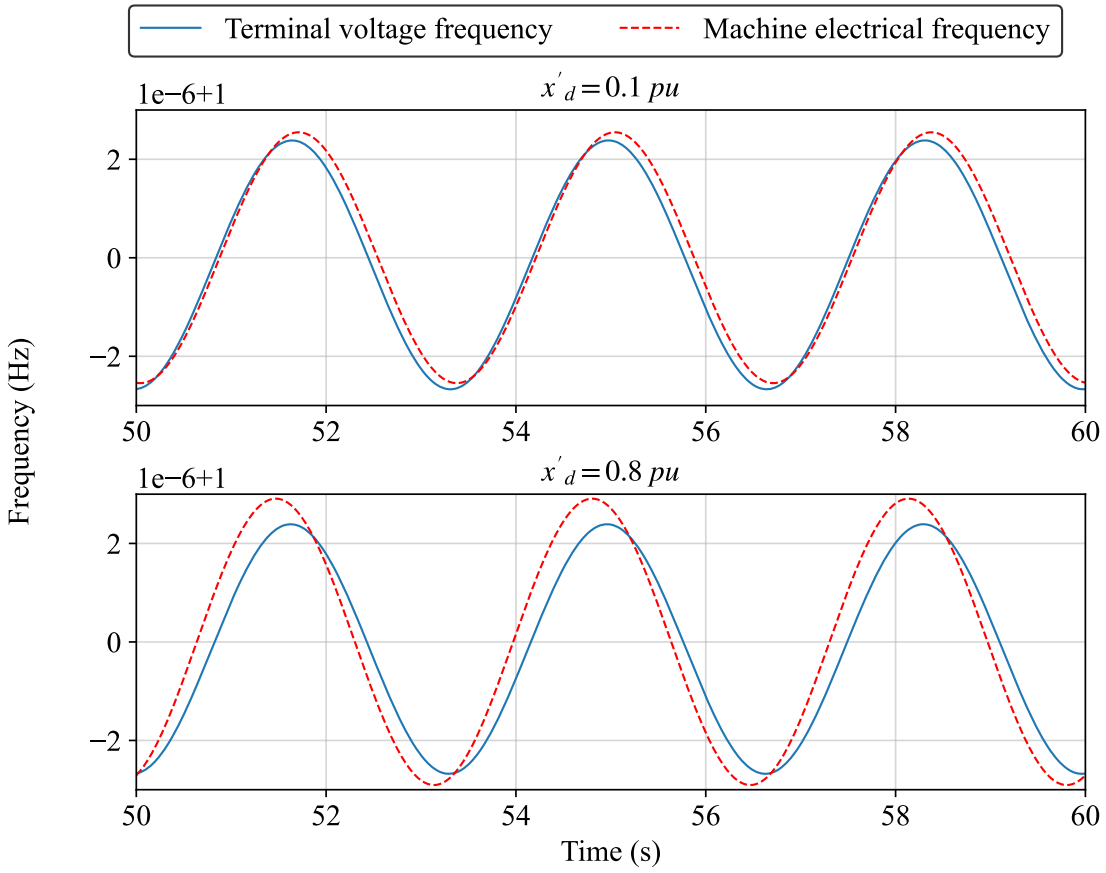

Figure 5.8: Comparison of terminal voltage frequency and rotor speed waveforms for classical synchronous machine model with injected probing frequency $\Delta f = 0.3$ Hz for $x'_d = 0.1$ pu, $x'_d = 0.8$ pu

Internal Impedance Compensation

Since the phase angle of the internal voltage δ of the classical model relates to the rotor angle, it is expected that the electrical frequency of the internal voltage E_g can accurately capture the behavior of the rotor speed signal ω_r. Although the internal voltage is not measurable, the internal voltage can be calculated using the terminal voltage and current measurements,

as given in (5.16).

$$E_{gQ} + jE_{gD} = v_{tQ} + jv_{tD} + jx'_d(i_Q + ji_D) \tag{5.16}$$

The D-Q components of the voltages and currents are calculated using the D-Q-0 transformation given in (5.5). The D-Q components of the internal voltage are then converted back to the phase variables and are given as inputs to the PLL, as illustrated in Fig. 5.9. The frequency of this signal (measured using a PLL) is then used for inertia measurement, as described in Section 5.1. To ensure that the internal voltage E_g is obtained appropriately w.r.t. the terminal voltage, the D-Q transformations are done with the same transformation angle γ as shown in Fig. 5.9. The frequency of the transformation is taken to be the steady-state frequency, i.e., 60 Hz. The accuracy of this approach is verified with the following case study.

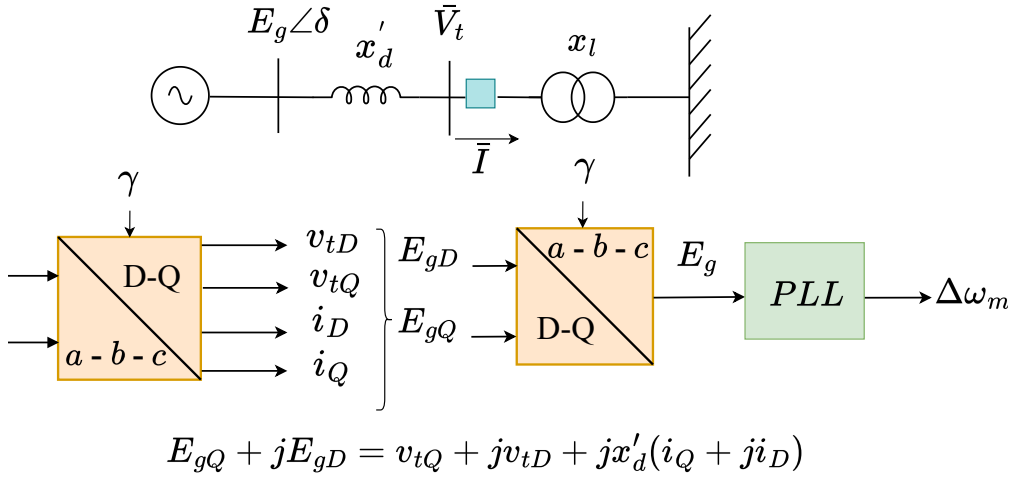

Figure 5.9: Schematic of internal voltage measurement approach

Fig. 5.10 illustrates the steady-state waveforms of the generator terminal frequency and

rotor speed for $x'_d = 0.8$ pu, without and with the proposed compensation. As anticipated, performing the compensation enables the terminal frequency to closely track the rotor frequency. This alignment ensures accurate inertia estimation.

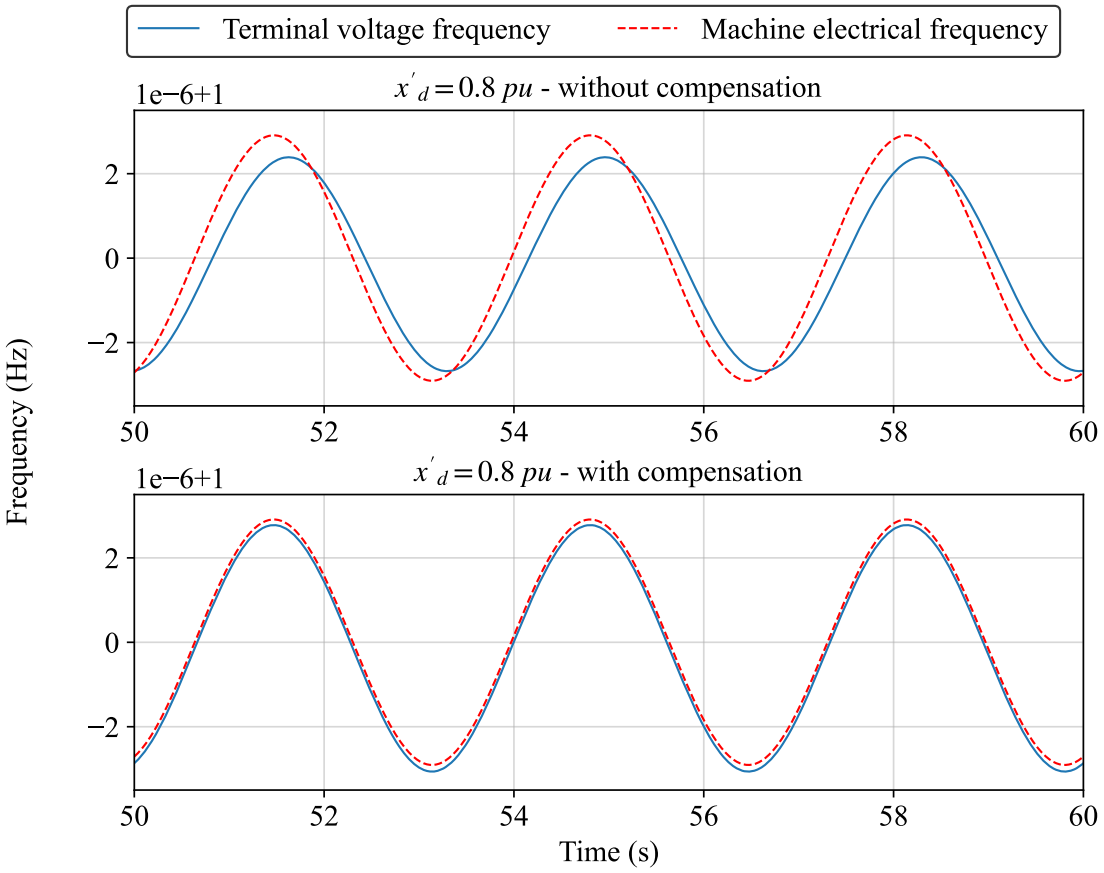

Figure 5.10: Comparison of terminal voltage frequency and rotor speed waveforms for classical synchronous machine model with injected probing frequency $\Delta f = 0.3$ Hz for $x'_d = 0.8$ pu without and with the compensation

The inertia estimation is done with and without compensating for the internal impedance of the generator with $x'_d = 0.8$ pu. As described earlier, the inertia is measured using two different injection frequencies. The measured inertia values for different injection frequencies are reported in Table 5.2. As expected, there is a significant error in the inertia measurement

at higher loading levels when the internal impedance compensation is not done. However, with the compensation, the inertia estimation is quite accurate.

Table 5.2: Measured Inertia values for classical generator model for different power loadings (P_o) and injected probing signal frequencies

		Injection frequency (Δf_2 in Hz)				
Compensation included?	Quiescent power (P_o)	0.1	0.25	0.3	0.4	0.5
Yes	0.1 pu	2.99	2.96	2.96	2.94	2.92
	0.5 pu	2.99	2.96	2.96	2.94	2.92
	0.9 pu	2.98	2.96	2.96	2.94	2.92
No	0.1 pu	3.1	3.14	3.16	3.22	3.29
	0.5 pu	3.14	3.17	3.21	3.27	3.35
	0.9 pu	3.32	3.39	3.41	3.47	3.56
For all cases, the first injection frequency was $\Delta f_1 = 0.2$ Hz						

The results presented in this section are useful to understand the behaviour of the classical model of synchronous generators and, therefore, also for inverters emulating such characteristics. The following section presents the inertia estimation of grid-forming inverters emulating classical synchronous generator models, commonly referred to as "Virtual Synchronous Generators" (VSG).

5.3 Inertia Measurement of Grid-Forming Inverters with VSG Control

The higher bandwidth of power-electronic converters allows one to emulate the dynamics of conventional synchronous machines. This is referred to as the "Virtual Synchronous Generator" or VSG control strategy [54]. The control structure of a VSG is illustrated in Fig. 2.13. The swing equation in (5.1) is implemented in the power synchronization loop.

The emulated angle θ is used as the reference angle for the voltage and current control loops of the VSC inverter. In addition to these components, the controller also includes over-current limiters to prevent excessive fault currents.

The schematic of the power circuit of a two-level VSC with VSG-based control is shown in Fig. 5.11. The inverter is connected to an LCL filter to filter out the switching frequency components. The converter is interfaced to the external ac system through a step-up transformer at the Point Of Interconnection (POI), as shown in the figure. The voltage and current measurements V_t and I_t, respectively, are used by the controller to generate the switching pulses.

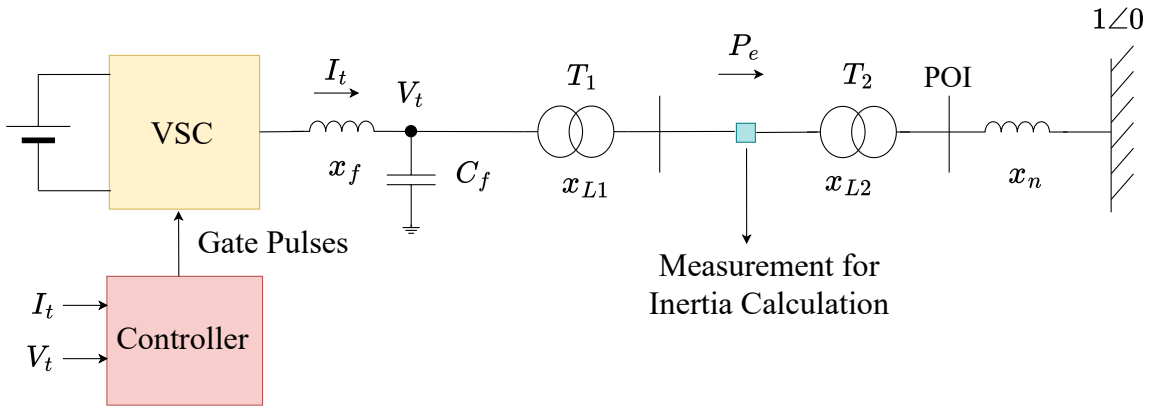

Figure 5.11: Power circuit schematic of VSC-based inverter

The steady-state deviations in the measured active power P_o and the frequency of the internal voltage is used instead of the converter speed signal ω_{vsg} to estimate the emulated inertia H. Although the VSG model has the advantage that markedly different parameters could be used in comparison to the actual generator, which is constrained only to realistic values, their structures and transfer functions are the same. Therefore, the treatment used for the classical generator models in the previous section can directly be extended to the

VSG case.

The proposed approach uses the fundamental relationship between power and frequency to estimate inertia and applies to any control mode or type of converter e.g., GFM, Grid Following (GFL), etc. Any control method that changes the power order as a function of frequency affects the virtual inertia and can be detected by this method. Since the approach is based on steady-state measurements, the inertia estimation is not expected to be influenced by over-current limiting strategies such as virtual impedance compensation [86, 87], which is active only during short-circuit faults and overload conditions. Although experimental results are presented here for specific control modes, the proposed method is versatile and can be applied to other control modes as well.

Since the converter control regulates the low voltage side of the transformer V_t, this voltage is analogous to that of the internal voltage E_g of a classical synchronous machine. Therefore, the frequency of this "internal" voltage can serve as a better representative of the converter speed signal ω_{vsg}. As a straightforward extension of the approach presented in Section 5.2.1, this internal voltage can either be directly measured or can be obtained using the compensation approach presented earlier. The frequency of this internal voltage can be measured using the PLL, which is used for the inertia measurement. The accuracy of this approach is presented using a numerical case study.

5.3.1 Inertia measurement using ω_{vsg} signal

Consider a two-level 200 MVA, 230 kV VSG connected as s shown in Fig. 5.11. The circuit parameters of the VSG, along with the controller parameters, are given in Table 5.3. The VSC converter is connected to a 230 kV ac system. The emulated inertia constant and damping are $H = 3$ s and $D = 0.05$ pu/(rad/s), respectively.

Table 5.3: VSG converter system parameters

Converter reactance (x_f)	0.335 mH
Filter capacitance (C_f)	700 μF
Converter transformer T_1 winding voltage	0.69/13.8 kV
Converter transformer T_1 leakage reactance (x_{L1})	0.0375 pu
Converter transformer T_1 rating	200 MVA
POI transformer winding voltage	13.8/230 kV
POI transformer T_2 rating	200 MVA
POI transformer T_2 leakage reactance (x_{L2})	0.125 pu
Network reactance (x_n)	0.014 pu
DC link voltage	1.45 kV
Voltage loop controller gains (K_{vp}, K_{vi})	(10,10)
Current loop controller gains (K_{ip}, K_{ii})	(0.5,100)

Table 5.4: Inertia measurement of VSG converter with ω_{vsg} signal

		Second injection frequency (Δf_2 Hz)				
Damping (in pu/rad/s)	Quiescent apparent power ($P_o + jQ_o$)	0.3	0.4	0.6	0.7	0.8
$D = 0.05$	0.1 pu	3.03	3.02	3.01	3.00	3.00
	0.5 pu	3.02	2.99	2.96	2.96	2.95
	0.9 pu	2.88	2.88	2.87	2.88	2.88
	$(0.25 + j0.5)$ pu	3.04	3.02	3.00	2.99	2.98
	$(0.7 + j0.25)$ pu	2.97	2.95	2.93	2.93	2.92
For all cases, the first injection frequency was $\Delta f_1 = 0.5$ Hz.						

The inertia measurement approach described in Section 5.1 is used here to measure the inertia capability of VSG-based converters. For the inertia estimation, a probing current

signal of magnitude 0.02 kA is applied at the POI. The inertia is first calculated for different quiescent operating conditions using the virtual speed signal ω_{vsg} and is given in Table 5.4. Since $D \neq 0$, the inertia is calculated using two injection frequencies as explained in Section 5.1. As expected, the converter virtual speed signal provides a very accurate estimate of the emulated inertia constant.

5.3.2 Bus Frequency-based Inertia Measurement

To evaluate the accuracy of the bus frequency-based approach, the bus voltage and current are measured, as shown in Fig. 5.11. The frequency of the terminal voltage is measured by the PLL and is used for inertia measurement (without internal impedance compensation). The PLL parameters are: $K_p = 10, K_i = 500, T_f = 0.001$ s. The calculated inertia values for different operating scenarios are shown in Table 5.5. The steady-state deviations in the

Table 5.5: Inertia measurement of VSG converter with bus frequency (without internal impedance compensation)

		Quiescent power output from VSC ($P_o + jQ_o$) pu				
Injection (Δf_2 Hz)		(0.1+8j0)	(0.5+8j0)	(0.9+8j0)	(0.25+j0.5)	(0.7+j0.25)
0.3	Inertia (s)	3.49	3.3	2.82	3.42	3.14
	Error (%)	16.3	10	6	14	4.66
0.4	Inertia (s)	3.47	3.27	3.0	3.4	3.14
	Error (%)	15.7	9	0	13.3	5
0.6	Inertia (s)	3.48	3.27	3.04	3.4	3.15
	Error (%)	16	9	1.33	13.3	5
0.7	Inertia (s)	3.48	3.28	3.05	3.41	3.19
	Error (%)	16	9.33	1.66	13.6	6.33
0.8	Inertia (s)	3.29	3.29	3.07	3.42	3.2
	Error (%)	9.66	9.66	2.33	14	6.66
For all cases, the first injection frequency was $\Delta f_1 = 0.5$ Hz						

internal voltage are then calculated by compensating for the impedance x_{L1}. The frequency of this signal is then measured using the same PLL. The estimated inertia (for the same D and H values) with the PLL-based frequency measurements (along with the relative errors) are presented in Table 5.6 for the same operating conditions.

Comparing the results of Tables 5.5 and 5.6, the internal impedance compensation improves the inertia estimate, as was indicated in Section 5.2.1. An interesting observation is that the inertia estimate is more accurate when the VSC operates at a higher power injection level. The accuracy of the measured inertia is acceptable when the injection frequency is up to about 1 Hz, which is within the bandwidth of the PLL.

Table 5.6: Inertia measurement of VSG converter with bus frequency (with internal impedance compensation)

		Quiescent power output from VSC ($P_o + jQ_o$) pu				
Injection (Δf_2 Hz)		(0.1+j0)	(0.5+j0)	(0.9+j0)	(0.25+j0.5)	(0.7+j0.25)
0.3	Inertia (s)	3.33	3.15	2.84	3.27	3.02
	Error (%)	11	5	5.33	9	0.66
0.4	Inertia (s)	3.29	3.12	2.86	3.23	3.00
	Error (%)	9.66	4	4.66	7.66	0
0.6	Inertia (s)	3.24	3.07	2.85	3.18	2.97
	Error (%)	8	2.33	5	6	1
0.7	Inertia (s)	3.21	3.04	2.85	3.15	2.94
	Error (%)	7	1.33	5	5	2
0.8	Inertia (s)	3.18	3.01	2.81	3.12	2.92
	Error (%)	6	0.33	6.33	4	2.66
For all cases, the first injection frequency was $\Delta f_1 = 0.5$ Hz						

5.3.3 Effect of Variation in Operating Conditions on Inertia Measurement

Our proposed method also works if the apparent inertia suddenly changes due to a change of operating point or controller setting. To verify the accuracy of the inertia estimation during change in operating condition, the active power reference of the GFM converter of the test system is increased. Fig. 5.12 illustrates this point by considering the case where a power order change from 0.1 to 0.2 pu is applied at $t = 7.1$ s as shown by Fig. 5.12 (a). The injected power follows the reference input and the steady-state power waveform has an oscillatory component, whose frequency is same as that of the injection frequency for inertia measurement. As shown in Fig. 5.12 (b), after a short period (approximately 4 s), the estimated inertia value stabilizes and converges to its pre-disturbance value, as it should because we have not ordered a change in inertia in the controller.

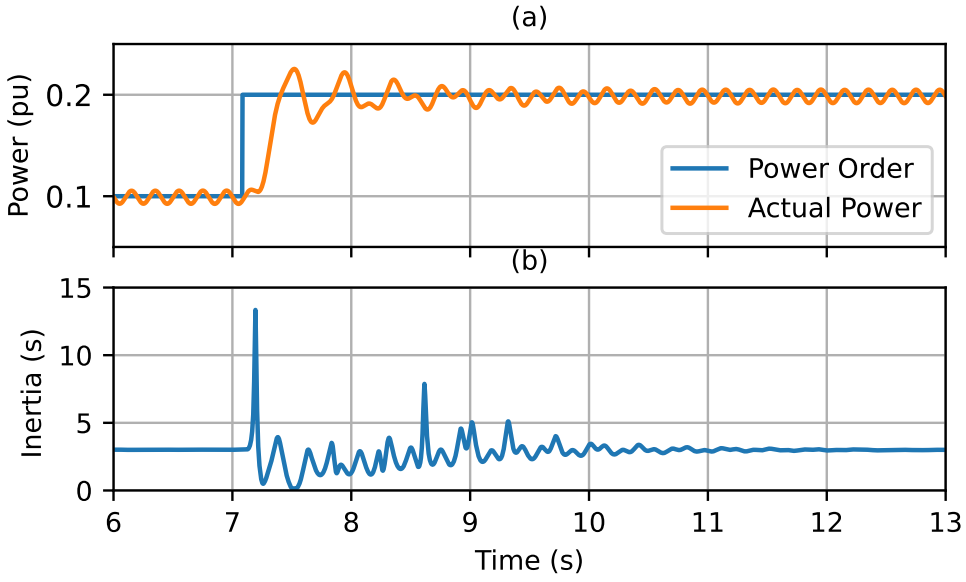

Figure 5.12: Observation that inertia estimation is not affected by active power change

5.4 Inertia Measurement of a Grid-Following BtB-SC

To further investigate the frequency support provided by the BtB-SC, a test system comprising a BtB-SC and a synchronous generator was developed; the layout of this configuration is illustrated in Fig. 5.13. The synchronous machine is rated at 100 MVA with inertia constant $H = 3$ s and a sub-transient reactance of 0.18 pu. The BtB-SC configuration and parameters are identical to those specified in Section 3.5.

The machine-side controller regulates the active and reactive power (P and Q), while the grid-side converter maintains the ac and dc bus voltages (V_{ac} and V_{dc}) in accordance with the control architecture illustrated in Fig. 2.11. The grid-side VSC converter is connected to a 230 kV ac system. The active power controller parameters are $K_1 = 0$ pu/pu and $K_2 = 20$ pu/pu, respectively. Therefore, the BtB-SC provides an apparent inertia of 10 s according to (3.14).

5.4.1 Measurement of BtB-SC Apparent Inertia Using Internal Speed Signal

To measure the BtB-SC apparent inertia using approach mentioned in Section 5.1, a probing current signal of magnitude 0.02 kA is applied at the Point of Interconnection (POI).

In this system, the inertial contribution of BtB-SC can be quantified using two distinct approaches. The first method involves calculating the aggregated inertia of the entire system (synchronous machine plus BtB-SC) and subsequently isolating the BtB-SC component by subtracting the known inertia constant of the synchronous machine. Alternatively, the BtB-SC inertia can be calculated individually by utilizing the synchronous machine speed deviation. In the latter approach, since the machine's speed deviation is equivalent to the

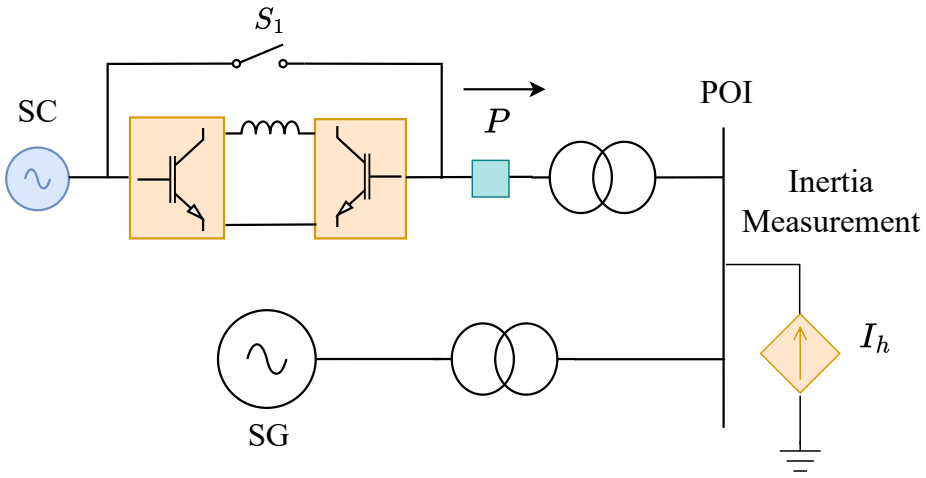

Figure 5.13: Schematic for apparent inertia measurement of BtB-SC using internal speed signal

frequency deviation at the grid-side converter terminal, the BtB-SC inertia can be derived directly from the frequency deviation and active power deviation measured at that terminal. Here, the second approach is used.

As indicated by the results presented in Table 5.7, the synchronous machine speed signal provides a highly accurate estimation within a maximum error of 5% from the actual apparent inertia value of 10 s.

Table 5.7: Inertia measurement of BtB-SC compensator using synchronous generator speed

	Second Injection Frequency (Δf_2 Hz)			
	0.1	0.2	0.4	0.5
Inertia (s)	9.98	9.92	9.68	9.51
Error (%)	0.2	0.8	3.4	4.9
For all cases, the first injection frequency was $\Delta f_1 = 0.3$ Hz				

5.4.2 Measurement of BtB-SC Apparent Inertia Using Bus Frequency Signal

To evaluate the accuracy of the bus frequency-based approach, the bus voltage and current are measured at the ac terminal of the grid-side converter, as illustrated in the schematic of the BtB-SC power circuit in Fig. 5.14. As shown, the grid-side converter is interfaced with the external ac system via a step-up transformer at the POI. The terminal voltage measurement, V_t, is utilized by the Phase-Locked Loop to measure the system frequency f; this frequency measurement serves as a primary input for the machine-side controller to determine the active power reference. Subsequently, the machine-side converter adjusts its active power to the reference value, utilizing the power provided by the SC. This power is then exchanged with the grid through the grid-side converter. Consequently, by analyzing the voltage frequency and active power deviations at the BtB-SC terminals, the proposed approach quantifies the inertia provided solely by the BtB-SC device.

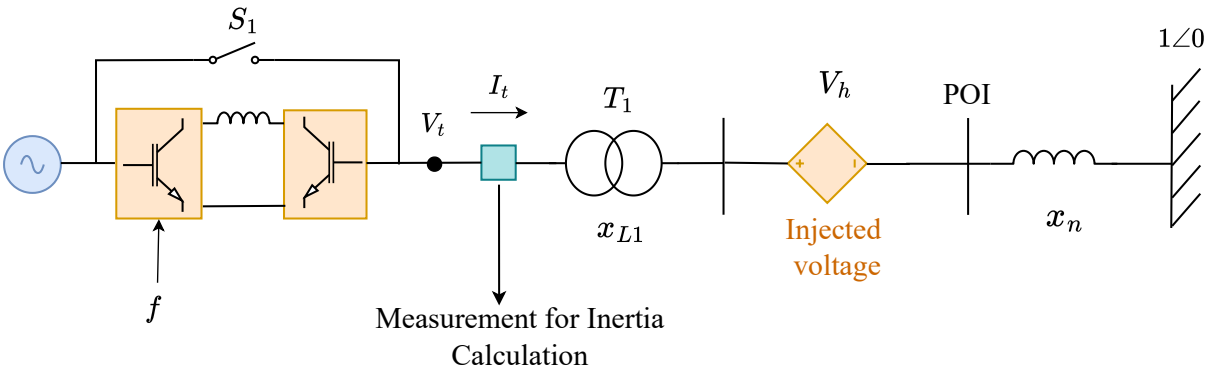

Figure 5.14: Power circuit schematic of BtB-SC for apparent inertia measurement of BtB-SC using bus frequency signal

The PLL parameters are: $K_p = 10, K_i = 500, T_f = 0.001$ s. The calculated inertia values using two different injection frequencies are shown in Table 5.8.

Table 5.8: Inertia measurement of BtB-SC compensator using bus frequency

	Second Injection Frequency (Δf_2 Hz)			
	0.1	0.2	0.4	0.5
Inertia (s)	10.29	10.58	10.43	9.46
Error (%)	2.9	5.8	4.3	5.4
For all cases, the first injection frequency was $\Delta f_1 = 0.3$ Hz				

As indicated in Table 5.8, the measured inertia is highly accurate when the injection frequency is within approximately 0.5 Hz. Since this range falls within the PLL bandwidth, the estimation maintains a low relative error of less than 6% compared to the actual inertia value of 10 s of the BtB-SC compensator. This is only marginally higher than when using the internal speed signal, which gave a maximum error of 5% as mentioned in Table 5.7.

5.5 Summary

This chapter introduced a novel inertia measurement method for Inverter-Based Resources utilizing the bus frequency signal. The proposed approach was first validated using a classic synchronous machine model to establish a baseline. Subsequently, the methodology was applied to both Grid-Forming system, which is controlled as a Virtual Synchronous Generator, and a Grid-Following system, exemplified by a Back-to-Back BtB-SC configuration. The approach was also compared and contrasted with the earlier approach proposed in [29], where the internal speed signal from the VSG controller is available, and was seen to give comparable accuracy.

A major advantage of the proposed approach is that it can be effectively applied even when only black-box models of the IBR are available, as it does not require knowledge of internal controller parameters. Furthermore, the proposed method provided a reasonably accurate estimation of the inertia constant. To demonstrate this, EMT-based numerical case studies were presented to validate the accuracy of this approach.

Chapter 6

Contributions, Conclusion, and Recommendations for Future Work

This final chapter summarizes the primary contributions of this research and discusses prospective directions for future work.

6.1 Contributions and Conclusions

The main contributions and conclusions of this research are summarized as follows:

- Using numerical electromagnetic transient (EMT) simulations, this thesis investigated the performance of a novel topology in which a synchronous condenser was connected to the ac bus of a weak LCC-HVDC system via a back-to-back voltage source converter link (BtB-SC). The results demonstrated that this configuration significantly enhanced the system's transient stability margin and rotor angle stability under severe disturbances, such as a long-duration three-phase solid fault. Following the disturbance, the

synchronous link between the SC and the grid was intentionally disconnected, allowing the SC to operate asynchronously. This decoupling enabled greater speed deviation, facilitating large energy exchanges between the SC and the ac network. Consequently, the BtB-SC arrangement provided higher apparent inertia, much smaller frequency deviations, and better immunity to rotor angle instability.

- The significant benefits of this topology as compared with a standalone synchronous condenser were demonstrated. During normal operation, the SC was synchronously connected to the grid, with the VSC converters operating as STATCOMs. This allowed the proposed BtB-SC configuration to deliver much higher reactive power following ac faults in comparison to a stand-alone SC, which helped in faster voltage recovery. During a frequency transient, an asynchronous connection between the SC and the grid allowed the ac network to exchange large amounts of energy with the SC, resulting in higher virtual inertia and a notably reduced $RoCoF$ compared to the standalone SC. In the specific case where $K_2 = 60$, the virtual inertia is effectively doubled; consequently, the magnitude of the $RoCoF$ was reduced by half, as illustrated in Fig. 4.3. The result was that the BtB-SC provided an inertia comparable to that of a much larger standalone SC.

- The approach also permitted dynamic adjustment of inertia by only exchanging active power when the frequency is moving away from 1.0 pu and by having zero exchange when it is naturally moving towards 1.0 pu. This approach prevented the BtB-SC from impeding frequency restoration, unlike a standalone synchronous condenser, by setting the BtB active power order to zero during recovery intervals. This control functionality further enhanced the system's frequency regulation performance.

- It was also demonstrated that increasing the VSC rating further reduced the $RoCoF$ by enabling the converter to exchange more power with the network without exceeding IGBT current limits. Additionally, the BtB-SC can modulate active power proportionally to frequency deviation, enhancing damping, improving frequency nadir, and reducing oscillations.

- To achieve the fastest possible frequency response, the active power controller parameters of the BtB-SC were optimized using a genetic algorithm, providing a significant enhancement in dynamic performance by effectively combining the benefits of increased inertia and improved damping, thereby ensuring a more stable and rapid frequency recovery following disturbances.

- A probing-based inertia measurement approach utilizing the bus frequency signal was proposed to quantify the inertia provided by grid-forming inverters emulating Virtual Synchronous Generator characteristics, as well as the BtB-SC grid-following system. The steady-state deviations in the bus frequency signal were utilized to calculate the emulated inertia of these inverters. A major advantage of the proposed approach is that it can be applied even when only black-boxed models of the IBR are available, as it does not rely on access to internal controller signals. Furthermore, the methodology provided highly accurate inertia estimation, maintaining a relative error of less than 5% for VSG, except under very low loading conditions, and less than 6% for the BtB-SC system.

6.2 Future Work

Further investigations are summarized as follows.

- Future research could involve a comparative performance analysis between the BtB-SC configuration, utilizing the static exciter modeled in this thesis, and alternative excitation strategies to evaluate their relative impact on rotor angle stability. Specifically, comparing this setup against a synchronous condenser equipped with brushless excitation systems would highlight the differences in their transient response times. Furthermore, investigating the coordination and performance of multiple synchronous condensers would provide deeper insights into the scalability and effectiveness of the proposed BtB-SC topology for complex grids characterized by a high penetration of low-inertia IBRs.

- Another promising investigation would be the development of a modified equal area criterion (EAC) to serve as an alternate analytical method for validating the improvements in critical clearing time (CCT) offered by the BtB-SC topology. While this thesis relies on numerical electromagnetic transient simulations to demonstrate stability enhancements, an analytical framework based on a mathematical model would allow for a more generalized assessment of the transient stability margin.

References

[1] J. Arrillaga, *High Voltage Direct Current Transmission*. London: Institution of Electrical Engineers, 1998.

[2] CIGRE working group B4.37, "Vsc transmission," 2005.

[3] M. P. Bahrman, "Hvdc transmission overview," in *2008 IEEE/PES Transmission and Distribution Conference and Exposition*, 2008, pp. 1–7.

[4] A. HALLEY (A.U.), N. MARTINS (B.R.), et al., "Effects of increasing power electronics-based technology on power system stability: Performance and operations," in *Cigre Science and Engineering, Volume N11*, June 2018.

[5] CIGRE working group 14.05, "Commutation failures. causes and consequences," 1996. [Online]. Available: https://e-cigre.org/publication/103-commutation-failures-causes-and-consequences

[6] CIGRE working group B4.41, "Systems with multiple dc infeed," 2008. [Online]. Available: https://ecigre.org/publication/364-systems-with-multiple-dc-infeed

[7] N. Hatziargyriou, J. Milanovic, C. Rahmann, V. Ajjarapu, C. Canizares, I. Erlich, D. Hill, I. Hiskens, I. Kamwa, B. Pal, P. Pourbeik, J. Sanchez-Gasca, A. Stankovic, T. Van Cutsem, V. Vittal, and C. Vournas, "Definition and classification of power system stability – revisited extended," *IEEE Transactions on Power Systems*, vol. 36, no. 4, pp. 3271–3281, July 2021.

[8] H. T. Nguyen, G. Yang, A. H. Nielsen, and P. H. Jensen, "Combination of synchronous condenser and synthetic inertia for frequency stability enhancement in low-inertia systems," *IEEE Transactions on Sustainable Energy*, vol. 10, no. 3, pp. 997–1005, July 2019.

[9] A. Moeini and I. Kamwa, "Analytical concepts for reactive power based primary frequency control in power systems," *IEEE Transactions on Power Systems*, vol. 31, no. 6, pp. 4217–4230, November 2016.

[10] O. B. Nayak, A. M. Gole, D. G. Chapman, and J. B. Davies, "Dynamic performance of static and synchronous compensators at an hvdc inverter bus in a very weak ac system," *IEEE Transactions on Power Systems (Institute of Electrical and Electronics Engineers); (United States)*, vol. 9:3, August 1994. [Online]. Available: https://www-osti-gov.uml.idm.oclc.org/biblio/6843829

[11] Y. Zhuang, R. Menzies, O. Nayak, and H. Turanli, "Dynamic performance of a statcon at an hvdc inverter feeding a very weak ac system," *IEEE Transactions on Power Delivery*, vol. 11, no. 2, pp. 958–964, 1996.

[12] D. Jovcic, N. Pahalawaththa, and M. Zavahir, "Investigation of the use of inverter control strategy instead of synchronous condensers at inverter terminal of an hvdc system," *IEEE Transactions on Power Delivery*, vol. 15, no. 2, pp. 704–709, Apr 2000.

[13] S. Bozhko, R. Li, R. Blasco-Gimenez, G. M. Asher, J. C. Clare, L. Yao, and C. Sasse, "Statcom-controlled hvdc power transmission for large offshore wind farms: Engineering issues," in *IECON 2006 - 32nd Annual Conference on IEEE Industrial Electronics*, April 2006, pp. 4219–4224.

[14] C.-K. Kim, "Dynamic coordination strategies between hvdc and statcom," in *2009 Transmission Distribution Conference Exposition: Asia and Pacific*, October 2009, pp. 1–9.

[15] Y. Zhang and A. M. Gole, "Quantifying the contribution of dynamic reactive power compensators on system strength at lcc-hvdc converter terminals," *IEEE Transactions on Power Delivery*, vol. 37, no. 1, pp. 449–457, February 2022.

[16] CIGRE working group B14.05, "Interaction between hvdc converters and nearby synchronous machines," 1997.

[17] N. Mendis, K. M. Muttaqi, and S. Perera, "Management of battery-supercapacitor hybrid energy storage and synchronous condenser for isolated operation of pmsg-based variable-speed wind turbine generating systems," *IEEE Transactions on Smart Grid*, vol. 5, no. 2, pp. 944–953, March 2014.

[18] Siemens, "The stable way synchronous condenser solutions," 2014. [Online]. Available: http://www.energy.siemens.com/ru/pool/hq/power-transmission/FACTS/Synchronous-Condenser/Synchronous-Condenser.pdf

[19] Y. H. Song, Y.-H. Song, and A. Johns, *Flexible AC transmission systems (FACTS)*, ser. IEE power and energy series ; 30. London: Institution of Electrical Engineers, 1999.

[20] D. Langner, G. Pilz, and M. Gurbiel, "Application benefits of line- or self-commutated static var compensator," *2014 IEEE PES General Meeting — Conference & Exposition*, pp. 1–5, July 2014.

[21] A. L. Rainer Marquardt, "New concept for high voltage-modular multilevel converter," *IEEE PESC*, June 2004.

[22] M. Claus, D. Retzmann, K. Uecker, A. Zenkner, "Improvement in voltage quality for power systems: Innovative reactive power compensation with modular multilevel voltage-sourced converter technology for grid access of wind farms," *International ETG - Congress, Düsseldorf*, October 2009.

[23] NESO, "Hybrid statcoms gcrp update." [Online]. Available: https://www.neso.energy/document/26001/download

[24] A. Ulbig, T. S. Borsche, and G. Andersson, "Impact of low rotational inertia on power system stability and operation," *IFAC Proceedings Volumes*, vol. 47, no. 3, pp. 7290–7297, August 2014.

[25] A. Stiger, R. Rivas, and M. Halonen, "Synchronous condensers contribution to inertia and short circuit current in cooperation with statcom," in *2019 IEEE PES GTD Grand International Conference and Exposition Asia (GTD Asia)*. IEEE, May 2019, pp. 955–959.

[26] Y. Zhang and A. Gole, "Consideration of inertia for design of reactive power compensation devices for hvdc transmission systems," in *10th IET International Conference on AC and DC Power Transmission (ACDC 2012)*. Stevenage, UK: IET, December 2012, pp. A42–.

[27] R. A. RIVAS, A. OWENS, F. WANG, E. ARNSTEN, R. RUI, C. FOOTE, "Phoenix: The world's first hybrid synchronous condenser system." CIGRE Session 48, December 2020.

[28] M. Mohaddes, M. Rashwan, C. Karawita, and H. Suriyaarachchi, "Application of Power Electronics to Enhance Synchronous Condenser Performance," in *Cigre B4 – DC Systems and Power Electronics*, 2022.

[29] T. Lin, A. M. Gole, M. K. Das, G. D. Irwin, A. L. Issacs, and D. A. Woodford, "An online probing frequency injection method for Grid-Forming IBRs inertia measurement," *Cigre Science and Engineering*, vol. CSE N32, February 2024.

[30] D. Woodford, "Hvdc transmission," 1998.

[31] *IEEE Std 1204-1997: IEEE Guide for Planning DC Links Terminating at AC Locations Having Low Short-Circuit Capacities.* IEEE, January 1997.

[32] O. Anaya-Lara, D. Campos-Gaona, E. Moreno-Goytia, and G. Adam, *Offshore Wind Energy Generation: Control, Protection, and Integration to Electrical Systems*, 1st ed. Newark: Wiley, April 2014.

[33] W. Long and S. Nilsson, "Hvdc transmission: yesterday and today," New York, pp. 22–31, April 2007.

[34] M. Bahrman, "Hvdc transmission overview," in *2008 IEEE/PES Transmission and Distribution Conference and Exposition.* IEEE, May 2008, pp. 1–7.

[35] L. Carlsson, G. Flisberg, and L. Weimers, "Recent evolution in classic hvdc," in *4th International Conference of Power Transmission Distribution Technology 2003, Chang. P.R. China*, 2003.

[36] C. Davidson, R. Preedy, J. Cao, C. Zhou, and J. Fu, "Ultra-high power thyristor valves for hvdc in developing countries," in *9th IET International Conference on AC and DC Power Transmission (ACDC 2010).* Stevenage: IET, October 2010, pp. O35–.

[37] M. Bahrman, J. Johansson, and B. Nilsson, "Voltage source converter transmission technologies: the right fit for the application," in *2003 IEEE Power Engineering Society General Meeting (IEEE Cat. No.03CH37491)*, vol. 3. IEEE, July 2003, pp. 1840–1847 Vol. 3.

[38] N. Flourentzou, V. Agelidis, and G. Demetriades, "Vsc-based hvdc power transmission systems: An overview," *IEEE Transactions on Power Electronics*, vol. 24, no. 3, pp. 592–602, February 2009.

[39] C. Guo, Y. Liu, C. Zhao, X. Wei, and W. Xu, "Power component fault detection method and improved current order limiter control for commutation failure mitigation in hvdc," *IEEE transactions on power delivery*, vol. 30, no. 3, pp. 1585–1593, March 2015.

[40] H.-J. Kim, D.-H. Kim, B.-M. Han, J.-H. Jung, and E.-C. Nho, "New synthetic test circuit for testing thyristor valve in hvdc converter," in *2012 IEEE Energy Conversion Congress and Exposition (ECCE).* IEEE, 2012, pp. 2053–2058.

[41] N. R. Chaudhuri, *Integrating Wind Energy to Weak Power Grids using High Voltage Direct Current Technology*, 1st ed. Cham: Springer International Publishing, 2019.

[42] K. Linden, "(12) Patent Application Publication (10) Pub. No.: U.S. 2013/0127426A1," vol. 1, no. 19, 2013.

[43] Y. Leng, "Comparison of synchronization techniques for generation of firing pulses for a hvdc converter," Master's thesis, Concordia University, 2006.

[44] A. Gole, "Validation and analysis of a grid control system using d-q-z transformation for static compensator systems," *Proc. Can. Conf. Elect. Comput. Eng., Montreal, QC, Canada, 1989-9*, pp. 745–748, 1989. [Online]. Available: https://cir.nii.ac.jp/crid/1570572700789772288

[45] A. Yazdani and R. Iravani, *Voltage-sourced converters in power systems: modeling, control, and applications*, 1st ed. Hoboken, N.J: Wiley, January 2010.

[46] B. Andersen, L. Xu, and K. Wong, "Topologies for vsc transmission," in *IEE conference publication*. London: IEE, December 2001, pp. 298–304.

[47] A. Abbas and P. Lehn, "Pwm-based vsc-hvdc systems - a review," in *2009 IEEE Power Energy Society General Meeting*. IEEE, July 2009, pp. 1–9.

[48] S. Debnath, J. Qin, B. Bahrani, M. Saeedifard, and P. Barbosa, "Operation, control, and applications of the modular multilevel converter: A review," *IEEE transactions on power electronics*, vol. 30, no. 1, pp. 37–53, January 2015.

[49] S. Debnath and M. Saeedifard, "A new hybrid modular multilevel converter for grid connection of large wind turbines," *IEEE Transactions on Sustainable Energy*, vol. 4, no. 4, pp. 1051–1064, September 2013.

[50] R. Rosso, X. Wang, M. Liserre, X. Lu, and S. Engelken, "Grid-forming converters: Control approaches, grid-synchronization, and future trends-a review," *IEEE Open Journal of Industry Applications*, vol. 2, pp. 93–109, April 2021.

[51] M. Chandorkar, D. Divan, and R. Adapa, "Control of parallel connected inverters in standalone ac supply systems," *IEEE Transactions on Industry Applications*, vol. 29, no. 1, pp. 136–143, February 1993.

[52] N. Soni, S. Doolla, and M. C. Chandorkar, "Improvement of transient response in microgrids using virtual inertia," *IEEE transactions on power delivery*, vol. 28, no. 3, pp. 1830–1838, June 2013.

[53] P. Kundur, *Power System Stability and Control*. New York: McGraw-Hill, 1994.

[54] Q.-C. Zhong and G. Weiss, "Synchronverters: Inverters that mimic synchronous generators," *IEEE Transactions on Industrial Electronics (1982)*, vol. 58, no. 4, pp. 1259–1267, April 2011.

[55] J. Alipoor, Y. Miura, and T. Ise, "Power system stabilization using virtual synchronous generator with alternating moment of inertia," *IEEE Journal of Emerging and Selected Topics in Power Electronics*, vol. 3, no. 2, pp. 451–458, June 2015.

[56] M. Chen, D. Zhou, and F. Blaabjerg, "Modelling, implementation, and assessment of virtual synchronous generator in power systems," *Journal of Modern Power Systems and Clean Energy*, vol. 8, no. 3, pp. 399–411, May 2020.

[57] K.-I. Sakimoto, K. Sugimoto, and Y. Shindo, "Low voltage ride through capability of a grid-connected inverter based on the virtual synchronous generator," in *2013 IEEE 10th International Conference on Power Electronics and Drive Systems (PEDS)*. IEEE, June 2013, pp. 1066–1071.

[58] Z. K. Shuai, Y. Y. Sun, Z. J. Shen, W. Tian, et al, "Microgrid stability: Classification and a review," *Renewable Sustainable Energy Reviews*, vol. 58, pp. 167–179, May 2016.

[59] M. Salmani, N. Rahbari-Asr, C. S. Edrington, and M.-Y. Chow, "Online and offline stability analysis methods for the power electronic-based components in design and operational stages," *IEEE Transactions on Power Electronics*, vol. 31, pp. 3151–3164, April 2016.

[60] P. M. Anderson, A. A. Fouad, *Power system control and stability*. Piscataway, N.J.: IEEE Press : Wiley-Interscience, 2003.

[61] K. R. Padiyar and M. K. Anil, "Analysis and control of loss of synchronism," *Dynamics and Control of Electric Transmission and Microgrids, IEEE*, pp. 247–282, December 2018.

[62] X. Zhao, Y. Xue, and X.-P. Zhang, "Fast frequency support from wind turbine systems by arresting frequency nadir close to settling frequency," *IEEE Open Access Journal of Power and Energy*, vol. 7, pp. 191–202, May 2020.

[63] IEEE Committee Report, "Dynamic performance characteristics of north american hvdc systems for transient and dynamic stability evaluations," vol. PAS-100, pp. 3356–3364, July 1981.

[64] T. Smed and G. Andersson, "Utilizing hvdc to damp power oscillations," *IEEE Transactions on Power Delivery*, vol. 8, pp. 620–627, 1993.

[65] Mao Xiao-ming, et al, "Coordinated control of interarea oscillation in the china southern power grid," *IEEE Transactions on Power Systems*, vol. 21, pp. 845–852, May 2006.

[66] W. Juanjuan, F. Chuang and Z. Yao, "Design of wams-based multiple hvdc damping control system," *IEEE Transactions on Smart Grid*, vol. 2, pp. 363–374, June 2011.

[67] J. Hazra, Y. Phulpin and D. Ernst, "Hvdc control strategies to improve transient stability in interconnected power systems," *PowerTech 2009 IEEE Bucharest*, pp. 1–6, June 2009.

[68] R. Eriksson, "Coordinated control of multiterminal dc grid power injections for improved rotor-angle stability based on lyapunov theory," *IEEE Transactions on Power Delivery*, vol. 9, pp. 1789–1797, August 2014.

[69] P. E. Marken, M. Henderson, D. LaForest, J. Skliutas, J. Roedel, and T. Campbell, "Selection of synchronous condenser technology for the granite substation," in *IEEE PES TD 2010*. IEEE, April 2010, pp. 1–6.

[70] NZ Shahraki, M Mohaddes, K Dey, AM Gole, "Enhancing inertia and voltage regulation using converter-interfaced synchronous condensers at LCC-HVDC terminals," in *IET Conference Proceedings CP918*. IET, April 2025, pp. 357–362.

[71] S. Kynev, G. Pilz, and H. Schmitt, "Comparison of modern statcom and synchronous condenser for power transmission systems," in *2016 IEEE Electrical Power and Energy Conference (EPEC)*. IEEE, October 2016, pp. 1–6.

[72] E. Rahimi, A. Gole, J. Davies, I. Fernando, and K. Kent, "Commutation failure in single- and multi-infeed hvdc systems," in *8th IEE International Conference on AC and DC Power Transmission (ACDC 2006)*. London: IEE, March 2006, pp. 182–186.

[73] "IEEE Guide for Specification of Transmission Static Synchronous Compensator (STATCOM) Systems," pp. 1–115, April 2019.

[74] T. J. E. Miller, *Reactive Power Control in Electric Power Systems*. John Wiley Sons, 1982.

[75] International Renewable Energy Agency (IRENA), "Grid Codes for Renewable Powered Systems," 2022.

[76] *IEEE Std C37.118.1a-2014 (Amendment to IEEE Std C37.118.1-2011): IEEE standard for synchrophasor measurements for power systems. amendment 1, modification of selected performance requirements*. Place of publication not identified: IEEE, April 2014.

[77] Manitoba Hydro, "Transmission System Interconnection Requirements," 2016,www.oasis.oati.com.

[78] M. R. Bonyadi and Z. Michalewicz, "Particle swarm optimization for single objective continuous space problems: A review," *Evolutionary computation*, vol. 25, no. 1, pp. 1–54, March 2017.

[79] J. S. Acosta Sarmiento, "Optimization of overhead transmission lines with multiple circuits at different voltage levels on the same tower," Ph.D. dissertation, University of Campinas, Brazil, 2021.

[80] Germain and D. Azar, "Genetic algorithms with local optima handling to solve sudoku puzzles," in *Proceedings of the 2018 International Conference on Computing and Artificial Intelligence*. New York, NY, USA: ACM, March 2018, pp. 19–22.

[81] L. M. Schmitt, "Theory of genetic algorithms ii: models for genetic operators over the string-tensor representation of populations and convergence to global optima for arbitrary fitness function under scaling," *Theoretical Computer Science*, vol. 310, no. 1, pp. 181–231, January 2004.

[82] J. A. Nelder and R. Mead, "A simplex method for function minimization," *Computer journal*, vol. 7, no. 4, pp. 308–313, January 1965.

[83] J. Alipoor, Y. Miura, and T. Ise, "Power system stabilization using virtual synchronous generator with alternating moment of inertia," *IEEE journal of Emerging and Selected Topics in power electronics*, vol. 3, no. 2, pp. 451–458, 2014.

[84] M. Han, R. Ma, and M. Zhan, "Transient synchronous stability analysis and assessment of pll-based vsc systems by bifurcation theory," *IEEE Transactions on Energy Conversion*, vol. 40, no. 2, pp. 1312–1324, June 2025.

[85] A. Gole and V. Sood, "A static compensator model for use with electromagnetic transients simulation programs," *IEEE Transactions on Power Delivery*, vol. 5, no. 3, pp. 1398–1407, July 1990.

[86] A. D. Paquette and D. M. Divan, "Virtual Impedance Current Limiting for Inverters in Microgrids With Synchronous Generators," in *IEEE Transactions on Industry Applications*, August 2015, pp. 1630–1638.

[87] S. P. Me, S. Zabihi, F. Blaabjerg, and B. Bahrani, "Adaptive virtual resistance for postfault oscillation damping in grid-forming inverters," *IEEE Transactions on Power Electronics*, vol. 37, no. 4, pp. 3813–3824, October 2021.

Appendix A

PLL small signal modeling

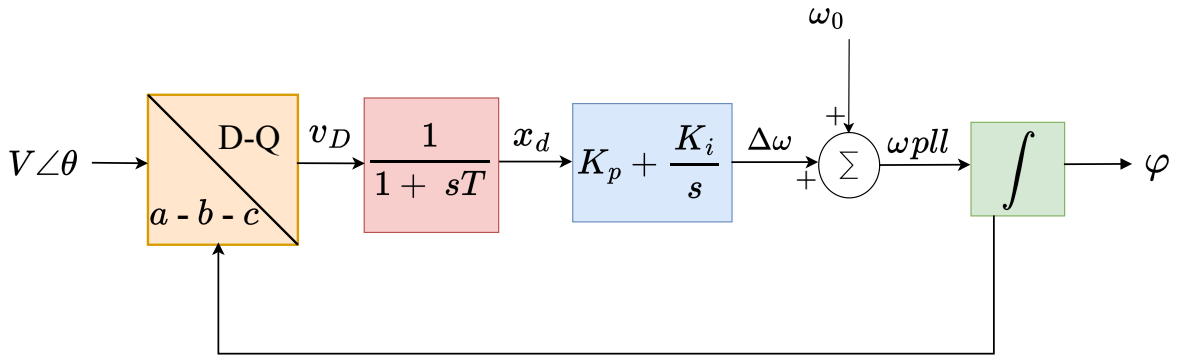

Figure A.1: PLL block diagram

$$v_D(t) = Vsin(\theta(t) - \varphi(t)) \tag{A.1}$$

According to fig.:

$$\frac{dx_d(t)}{dt} = \frac{-1}{T}x_d(t) + \frac{1}{T}v_D(t) \tag{A.2}$$

$$\frac{dx_i(t)}{dt} = x_d(t) \implies \frac{d\Delta x_i(t)}{dt} = \Delta x_d(t) \implies s\Delta x_i(s) = \Delta x_d(s) \tag{A.3}$$

$$\Delta\omega = k_i x_i + k_p x_d \tag{A.4}$$

$$\omega_{pll}(t) = \Delta\omega(t) + \omega_0 \xrightarrow{substituting\ (A.4)} \omega_{pll}(t) = k_i x_i(t) + k_p x_d(t) + \omega_0 \tag{A.5}$$

$$\begin{aligned} &\frac{d\varphi(t)}{dt} = \omega_{pll}(t) \xrightarrow{substituting\ (A.5)} \frac{d\Delta\varphi(t)}{dt} = k_i \Delta x_i(t) + k_p \Delta x_d(t) \implies \\ &s\Delta\varphi(s) = k_i \Delta x_i(s) + k_p \Delta x_d(s) = \frac{k_i}{s}\Delta x_d(s) + k_p \Delta x_d(s) = (\frac{k_i}{s} + k_p)\Delta x_d(s) \end{aligned} \tag{A.6}$$

$$\begin{aligned} \frac{d\Delta x_d(t)}{dt} &= \frac{-1}{T}\Delta x_d(t) + \frac{1}{T}V cos(\theta_0 - \varphi_0)\Delta\theta(t) - \frac{1}{T}V cos(\theta_0 - \varphi_0)\Delta\varphi(t) + cos(\theta(t) - \varphi(t))\Delta V \\ &\implies s\Delta x_d(s) = \frac{-1}{T}\Delta x_d(s) + \frac{1}{T}V\Delta\theta(s) - \frac{1}{T}V\Delta\varphi(s) + cos(\theta(s) - \varphi(s))\Delta V \end{aligned} \tag{A.7}$$

Under the assumption of constant voltage magnitude $V = 1pu$, (A.7) is reformulated as:

$$(s + \frac{1}{T})\Delta x_d(s) = \frac{1}{T}(\Delta\theta(s) - \Delta\varphi(s)) \implies \Delta x_d(s) = \frac{\frac{1}{T}(\Delta\theta(s) - \Delta\varphi(s))}{(s + \frac{1}{T})} \tag{A.8}$$

Substituting (A.8) into (A.6) yields:

$$\begin{aligned} s\Delta\varphi(s) = \frac{\frac{1}{T}(\Delta\theta(s) - \Delta\varphi(s))(\frac{k_i}{s} + k_p)}{(s + \frac{1}{T})} &= \frac{(\Delta\theta(s) - \Delta\varphi(s))(\frac{k_i}{s} + k_p)}{(1 + sT)} \\ \implies \Delta\varphi(s) &= \underbrace{\frac{(\frac{k_i}{s} + k_p)}{s(1 + sT)(\frac{k_i}{s} + k_p)}}_{G(s)}\Delta\theta(s) \end{aligned} \tag{A.9}$$

(A.9) demonstrates that the PLL angle (or frequency) tracks the measured voltage angle θ (or frequency) exactly when the transfer function $G(s) = 1\angle 0$. This condition is satisfied where the complex frequency s is very small. Consequently, the PLL provides an accurate measurement of the bus frequency only when the injection frequency is near the fundamental frequency. Under these conditions, the frequency deviation—represented by $\Delta\omega$—remains sufficiently small, ensuring the transfer function maintains near-unity gain.